Multiscale Modeling of Multicompartment Micelles: Influence of Triblock and Tetrablock Polymer Architecture on Morphological Variation

A Doctoral Dissertation
Presented to
The Academic Faculty

by

Connor P. Callaway

In Partial Fulfillment
Of the Requirements for the Degree
Doctor of Philosophy in the
School of Materials Science and Engineering
College of Engineering

Georgia Institute of Technology
May 2020

Multiscale Modeling of Multicompartment Micelles:
Influence of Triblock and Tetrablock Polymer Architecture on Morphological Variation

Approved by:

Dr. Seung Soon Jang, Advisor
School of Materials Science and Engineering
Georgia Institute of Technology

Dr. Donggang Yao
School of Materials Science and Engineering
Georgia Institute of Technology

Dr. Zhiqun Lin
School of Materials Science and Engineering
Georgia Institute of Technology

Dr. Christopher Jones
School of Chemical and Biomolecular Engineering
Georgia Institute of Technology

Dr. Paul Russo
School of Materials Science and Engineering
Georgia Institute of Technology

Date approved: December 5, 2019

ACKNOWLEDGEMENTS

This thesis was funded by the U.S. Department of Energy, Office of Science, Office of Basic Energy Sciences, under Award DE-FG02-03ER15459.

To Prof. Christopher Jones, Prof. Zhiqun Lin, Prof. Paul Russo, and Prof. Donggang Yao, I am deeply grateful for your support as part of my doctoral committee. To the countless other professors whose mentorship and guidance helped me innumerable times through my educational career, I thank you as well – all of you have shaped me into the teacher and researcher I am today.

To the wonderful friends and colleagues I have been fortunate enough to work with – Kayla Hendrickson, Vivian Bond, Dr. Jiil Choi, Mackenzie Mallard, Robin Lawler, and many more, I thank you all for your collaboration, for your wonderful work, and, of course, for your friendship. Each and every one of you has made the journey more fun.

And now, specific thanks to those who have been invaluable to my graduate student career:

Prof. Seung Soon Jang: I want to express my sincerest gratitude and appreciation. I give you my thanks for the kindness you have shown me as my doctoral advisor, for the myriad lessons you have provided, for the chance to shape a research lab that I love profoundly, and – above all – for encouraging me to become all that I never dared to believe I could be.

Allie Burch: If I had told you seven years ago that you would be mentioned here, I'm not sure you would have believed me. I'm not sure I would've, either. Thanks for the support, the banter, and the steadfast friendship.

Steven Walker: Our conversations have varied everywhere from the Chicago rap scene to pun chains that last for days. Thanks for giving me a friendship that defies explanation.

Shruti Venkatram: You were the first friend I made when I got to Georgia Tech. Now, as I look over the horizon, all I can say is that I am endlessly glad you're still there.

Jas Vahidsafa: Looks like we both survived grad school in the end, eh? I'm glad we met – I'm so fortunate to count you among my best friends. Here's to the years yet to come.

CJ Caliendo: I'd say I owe you a meal next time I see you, but I'm no fool – I wouldn't be able to afford it…even on a postdoc salary.

Omar Allam: It's not often I laugh so hard I cry, but you always seem to find a way to make that happen, in new and unexpected ways.

SeungMin Lee: I'm not sure how I'll manage without your incomprehensible metaphors, so please do text me one every now and then.

To the three knuckleheads above: SeungMin, Omar, and CJ, you are some of the best friends I could ask for. I'm proud of everything you've all accomplished and everything you've all become – and incredibly fortunate to have found the fellowship that we did.

Kevin Xiong: Brother, it has been a long time coming, but I finally made it. Thanks for the endless hours of conversation, the support at the worst of times, and the laughter at the best. Over a decade and counting – know always that I have your back.

Aunt Carolynne and Uncle Bill: It hasn't always been easy to believe I'd make it to the end of this educational journey, but the two of you have always shown how much you believe in me. Your love and support through the years has spoken volumes – thank you for everything.

Maggie and Maya: It's been an honor watching you both come into your own. I'm so lucky to have you as my sisters. Thanks for the memes, the jokes, and the unspoken companionship that one can find only with siblings. Never stop believing in yourselves and what you can accomplish. Never forget that I am proud of you both for the strength and dedication you have demonstrated many times over. And never forget that I love you both, always.

And, above all, Mom and Dad: Not one step of this journey could have happened without both of you. I will never be able to articulate the gratitude I have for the boundless love and tireless support you have provided me, nor will I ever stop trying to do so. You have both been everything a person could hope for from their parents, and I could not ask for better. I have learned so much from you, and everything I have accomplished is a testament to your parenthood, to your unwavering belief in me, and to who you are. I love you both more than I can describe. Thank you, now and forever.

TABLE OF CONTENTS

LIST OF TABLES

LIST OF FIGURES

LIST OF ABBREVIATIONS

CVN – Connolly volume normalization

DFT – density functional theory

DPD – dissipative particle dynamics

ESP – electrostatic potential

EST – electronic structure theory

GGA – generalized gradient approximation

HF – Hartree-Fock

HLF – hydrophilic, lipophilic, and fluorophilic

IGC – inverse gas chromatography

KS-DFT – Kohn-Sham density functional theory

LDA – local density approximation

MCM – multicompartment micelle

MCMNR – multicompartment micelle nanoreactor

MNR – micelle nanoreactor

PECH – poly(epichlorohydrin)

PEF – potential energy function(s)

PEG – polyethylene glycol

PES – potential energy surface

PMA – poly(methyl acrylate)

PMMA – poly(methyl methacrylate)

QEq – charge-equilibration

SANS – small-angle neutron scattering

SCF – self-consistent field

SUMMARY

Multicompartment micelles offer great potential for catalytic science, owing to their ability to sequester immobilized catalytic species into distinct chambers within the micelle. In multi-step reaction sequences that feature non-orthogonal reaction steps, multicompartment micelles help to maintain overall reaction efficiency or catalyst efficacy by confining reaction steps to distinct catalytic compartments and by guiding reactants and products through thermodynamic species flow throughout the micelle. The morphology of a multicompartment micelle thus directly influences its performance for catalytic applications. This work explores the relationships between block copolymer architecture and micelle morphology in order to allow the synthetic chemist greater control over morphology when synthesizing micelle systems. The chief results of this work include the development of a computational methodology for estimating the Flory-Huggins χ-parameter and the formulation of a structural parameter $\mathcal{R}$ which allows for the morphologies of multicompartment micelles to be predicted on the basis of the block copolymer architecture.

1. INTRODUCTION

Efficient reaction design forms an important foundation of many processes in modern chemistry. Reaction optimization has far-reaching effects that greatly improve many other facets of polymer manufacturing, pharmaceutical production, and related industries[1-8]. In particular, a field of growing interest during the past century is that of immobilized molecular catalysis[9-19]. This topic holds great potential due to its combination of the best strengths of both homogeneous and heterogeneous catalysis. By allowing for high selectivity and reaction rates traditionally achieved by homogeneous catalysis while still yielding the excellent separability offered by heterogeneous catalysis, this field presents an opportunity to leverage the advantages of both techniques[19-24].

Despite the strengths of immobilized molecular catalysis, however, systems containing multiple *tandem* non-orthogonal reactions (i.e., reactions which have the potential for mutual interference) still encounter difficulties[25-28]. In extreme cases, a particular step of the multistep reaction may even be incompatible with another species present in the system; in such a case, the catalyzing agent could suffer drastically reduced efficacy or cease to function altogether[29].

For example, as studied previously by Lu et al.[30], the hydration reaction of terminal alkynes into methyl ketones may be catalyzed by cobalt porphyrin (Co-Por) complexes. In the presence of sodium formate (HCOONa), however, this hydration reaction is prevented. Similarly, the methyl ketones may be transformed into chiral secondary alcohols of great utility in pharmaceutical applications. The corresponding asymmetric transfer hydrogenation (ATH) reaction, catalyzed by an N-tosylated derivative of 1,2-diphenyl-1,2-ethylenediamine containing rhodium (Rh-TsDPEN), is prevented by the presence of triflimide (HNTf2). These incompatibilities present obstacles that traditional implementations of immobilized molecular catalysis alone cannot surmount.

A potential solution to these obstacles arises in a field of study which has been the subject of growing academic interest in recent years – namely, that of multicompartment micelles. These systems offer separate molecular "chambers" in which each of the non-orthogonal reactions can take place, allowing for one-pot synthesis and tandem catalysis[30-35]. Micelles are, of course, well studied in chemistry; indeed, the multicompartment micelle (MCM) is simply an extension of the traditional idea. It is well known that a typical micelle is generally composed of polymers which have hydrophilic and hydrophobic portions[36-37]. MCMs, then, are composed of polymers of three or more distinct portions; a common example results from triblock copolymers containing hydrophilic, lipophilic, and fluorophilic (HLF) blocks[38-44]. For a proper choice of solvent, solutions of these polymers thus self-assemble into micellar structures containing three or more regions of microphase separation.

By introducing immobilized catalysts into MCM-containing systems, it is possible to create a micelle nanoreactor[45-57]. Because of the multicompartmental nature of the micelles in the system, it is possible to introduce different immobilized catalysts within each region of the MCM, thereby creating distinct catalytic regions within the structure that support simultaneous non-orthogonal reactions without the need for successive reaction chambers while still achieving high reaction rates and easy separability[30, 34, 52-54, 57-59]. The micelle nanoreactor (MNR) thus presents an elegant solution to many of the challenges facing immobilized molecular catalysis science.

It is natural to expect that the particular structural morphology of the micelles formed by a given polymer will in turn affect their utility in MNR applications. By extension, the particular architecture of the polymers selected for the formation of MCMs will have a marked effect on the performance of the resultant MNR system. For example, even if the species which define the different regions of solvophilicity of the polymer are held constant, variations in the sequence,

lengths, and length ratios of the respective blocks can lead to significant morphological changes in the resultant MCMs[42-44, 60]. Such changes can then lead to diminished catalyst effectiveness (e.g., due to decreased extent of compartmentalization) or less desirable reactant and product transport (leading to reduced reaction rates).

Therefore, proper design of MCM systems for use in MNR applications requires complete understanding of how to control the polymer architecture and, consequently, the micelle structure. A systematic study of the effects of the relevant variables is, however, made difficult in experiment due to the time-consuming preparation and reactions involved. Computational techniques offer a more economical avenue for the study of large systems such as these, as they allow for direct analysis of the MCM structure without the need for structural synthesis.

Of course, computational methods are not without their own set of challenges. Whereas chemical systems in physical experiments follow nature's specifications, simulations must be carefully designed to recreate the real behavior of the given system[61-65]. Clearly, for instance, two different chemical species in nature need not be instructed as to their miscibility – free energy considerations dictate the preferred phase(s) of the system. Computational models of these molecules, however, do not have this natural intuition; explicit simulations must be performed to determine these properties before the true study of interest can begin in earnest[61].

Considering all of these factors, the present work aims to study the effects of polymer architecture and composition on the morphology of the resulting self-assembled multicompartment micelles. The foundation of this study lies in the development of a robust methodology for determining the miscibility of polymer species[61] and several studies of morphological tunability in triblock[66-67] and tetrablock copolymer micelles. Four major studies have already been accomplished toward this goal and comprise Chapters 3-6 of this dissertation. Future work on this

project, to be undertaken either by the author or by a future researcher, will focus on (1) additional refinement of χ-parameter simulation techniques, as introduced in Chapter 3; (2) the extension of the structural parameter $\mathcal{R}$, introduced in Chapters 3 and 4, to include thermodynamic information; (3) the study of additional tetrablock sequences to complement those studied in Chapter 6, and (4) the introduction of reactants, products, and potentially catalysts into the MCM systems in order to directly study the effectiveness of such a system for MNR purposes. These potential studies are discussed in greater detail in Chapter 8.

2. THEORETICAL AND COMPUTATIONAL BACKGROUND

2.1. Thermodynamics and Statistical Mechanics

A brief discussion of the key items in the theoretical background of this work is warranted. From a thermodynamic perspective, a detailed study of micelle self-assembly rests on the foundation of Flory-Huggins solution theory, which begins with the traditional definition of Gibbs free energy of mixing, given as

$$\Delta G_m = \Delta H_m - T\Delta S_m, \quad (1)$$

where T represents the absolute temperature[68-70]. Flory-Huggins theory reduces the solution to a lattice model[70-71]. Thus, the entropy of mixing ΔS_m can be determined through configurational statistics on the polymer chains as

$$\Delta S_m = -R(n_1 \ln \phi_1 + n_2 \ln \phi_2), \quad (2)$$

where R is the gas constant and n_i and ϕ_i represent the number of moles and the volume fraction of species i, respectively. Likewise, the enthalpy change upon mixing (ΔH_m) may be expressed through the change in interaction energies between the unmixed and mixed states:

$$\Delta H_m = (n_1 N_A)\phi_2 \Delta w_{12} \quad (3)$$

where the mixing energy Δw_{12} is given as

$$\Delta w_{12} = \frac{1}{2}[(Z_{12} + Z_{21})E_{12} - (Z_{11}E_{11} + Z_{22}E_{22})]. \quad (4)$$

Here Z_{ij} represents the coordination number of the species j around the species i, while E_{ij} represents the interaction energy between individual molecules of species i and j:

$$E_{ij} = \varepsilon_{ij} - (\varepsilon_i + \varepsilon_j), \quad (5)$$

that is, the difference between energy of the two molecules in a paired configuration and of the two separately. While the *mixing* energy may commonly be either positive or negative, depending

on the particular pairing of species, the *interaction* energy is nearly always negative between uncharged molecules, due to favorable intermolecular interactions[71]. Then χ_{12} is defined as

$$\chi_{12} = \Delta w_{12}/RT \tag{6}$$

and its relationship with the enthalpy of mixing is given as

$$\Delta H_m = n_1 \phi_2 \chi_{12} RT \tag{7}$$

Thus, the change in free energy upon mixing is expressed in terms of ϕ_1, ϕ_2, χ_{12}, and RT via the combination of equations (1), (2), and (7):

$$\Delta G_m = RT(n_1 \ln \phi_1 + n_2 \ln \phi_2 + n_1 \phi_2 \chi_{12}) \tag{8}$$

Micelles are defined by their microphase separation into distinct regions[36-37, 42-44]; the simplest case often contains just a solvophobic core with a solvophilic corona, governed by a *positive* free energy of mixing between the species of the two regions. For this reason, there exists a crucial dependence in a micelle solution upon the pairwise miscibility of each identifiable species with the others. In designing a computational model of a micelle solution, it is clearly essential to obtain accurate χ_{12} values for each pair of identifiable copolymer species (i.e., regarding the solvophobic and solvophilic portions of the fundamental copolymer as *distinct* species). A discussion of the availability and shortcomings of *experimental* techniques for doing this, as well as a newly developed *computational* methodology for estimating χ_{12}, is presented in Chapter 3.

Computational simulations, however, are performed on groups of molecules far too few in number for thermodynamics to apply[72]. Further analysis based on statistical mechanics then becomes necessary to extend the scope of the system to the thermodynamic level[73]. In particular, the partition function Q of the possible states offers a manner in which the thermodynamics of the system may be studied; generally speaking, the partition function is a summation over all possible available states of the system. In energy space, this would take the form

$$\sum_i \rho(\varepsilon_i), \tag{9}$$

where $\rho(\varepsilon_i)$ represents the unnormalized probability of energy state ε_i. The particular form of this probability can change depending on which system parameters are held constant; the groups of parameters held constant are the various statistical mechanical *ensembles*. A common choice of ensemble is the so-called NVT or *canonical* ensemble, in which the number of particles, system volume, and average system temperature are all held constant. In such an ensemble, $\rho(\varepsilon)$ becomes the familiar weight factor of the Boltzmann distribution and the partition function becomes

$$\mathrm{Q} = \sum_i \exp(-\beta\varepsilon_i) = \sum_i \exp(-\varepsilon_i/k_B T). \tag{10}$$

This quantity is particularly important since all thermodynamic properties of interest may be derived from it. In particular, the ensemble average energy (i.e., across all states) is given as

$$\langle E \rangle = -\left(\frac{\partial \ln Q}{\partial \beta}\right) = [\sum_i \varepsilon_i \exp(-\varepsilon_i/k_B T)]/[\sum_i \exp(-\varepsilon_i/k_B T)]. \tag{11}$$

Of course, computationally sampling *all* possible energy states for a molecule of any real complexity becomes an impossible task. Fortunately, the nature of the Boltzmann weight factor means that high-energy states are much less probable. They then contribute little to the partition function and to the average energy. Thus, for the scope of this work, an alternative "pseudo-partition function" Q^* will be defined as a sum over all the N_s lowest-energy samples from configurational space. These energy samples represent the most important contributions to the average energy; the states which are excluded from consideration will be fairly high in energy and therefore justifiably may be assumed to cause a sufficiently small error in the pseudo-ensemble average energy E^* across all sampled states.

2.2. Theory of Computational Methods

Through statistical mechanics, the pseudo-ensemble average can be determined for the interaction energies E_{11}, E_{12}, and E_{22}. These three values, as well as the four possible coordination

numbers Z_{11}, Z_{12}, Z_{21}, and Z_{22}, must be computed for each possible pairing of distinct species in the system. As an example, the seven values mentioned before would need to be computed for each of the three pairings possible in a simple AB copolymer micelle system – namely, the A-B interpolymer pairing and the solvent-A and solvent-B pairings.

In order to generate accurate values for these pairings, it becomes essential to consider factors at multiple length scales. Indeed, a word about the level of theory in computational studies is warranted. Computational techniques vary significantly depending on the length scale in question; at the level of a single atom or molecule, electronic structure theory (EST) should be used to determine the most favorable orbital occupation for a given geometry[72, 74-75]. At this scale, techniques such as density functional theory or post-Hartree-Fock methods are common.

When there are several atoms present, EST may still be used (with less rigorous settings, of course), but force field methods often become more economical for larger systems (~50 atoms or more), especially if only generally correct values of orbital occupation-based properties, like partial atomic charges, are needed. Force field methods certainly treat the electronic energy of a molecule more approximately but give an added advantage of being *significantly* cheaper while still delivering satisfactory accuracy. Even still, these methods are unsuitable for systems with hundreds or even thousands of atoms; at such large length scales, coarse-grained (or *mesoscale*) techniques are often used to reduce the level of detail represented in the system, allowing for the evolution of many atoms or molecules to be studied at the network scale.

2.2.1. Electronic Structure Theory

At the lowest length scale, EST methods are universally based upon approximate solution of the time-independent Schrödinger equation

$$\hat{H}(\boldsymbol{x})\psi(\boldsymbol{x}) = E\psi(\boldsymbol{x}), \tag{12}$$

where E is the total energy corresponding to wavefunction $\psi(\boldsymbol{x})$ and $\widehat{H}(\boldsymbol{x})$ is the Hamiltonian operator of the system given by

$$\widehat{H}(\boldsymbol{r}) = -\hbar\nabla^2/2m + V(\boldsymbol{x}). \tag{13}$$

The two terms in the Hamiltonian above represent kinetic and potential energy contributions. Lastly, the coordinate $\boldsymbol{x}$ contains both a spatial coordinate $\boldsymbol{r}$ and a spin coordinate σ.

EST methods may be classified either as wavefunction-based or electron density-based. The former includes Hartree-Fock theory[76-80] (procedures which do not rigorously consider electron correlation and London dispersion effects[81]) or post-Hartree-Fock methods[72, 82] (procedures which include increasingly rigorous treatment of electron correlation[83-87]). Despite these differences, a commonality to many wavefunction methods is their basis in the variational theorem and dependence on a self-consistent field (SCF) procedure[78]. It should be noted that EST methods based in perturbation theory do *not* make use of the variational theorem[88-89]; these methods are, however, beyond the scope of the current work.

The first step in this process is generally to transform the Schrödinger equation into a one-electron Schrödinger equation of the form

$$f(\boldsymbol{x}_k)\phi_i(\boldsymbol{x}_k) = \varepsilon_i\phi_i(\boldsymbol{x}_k), \tag{14}$$

where $f(\boldsymbol{x}_k)$ fills the role of a one-electron Hamiltonian operator that considers kinetic energy as well as Coulombic and exchange interactions. $\phi_i(\boldsymbol{x}_k)$ represents a one-electron wavefunction as opposed to the overall wavefunction $\psi(\boldsymbol{x})$, in much the same way that ε_i represents the energy of a single electron as opposed to the total energy E.

Next, basis functions are introduced as linear combinations of atomic orbitals, taking the form

$$\phi_i(\boldsymbol{x}_k) = \sum_\mu C_{\mu i}\tilde{\phi}_\mu \tag{15}$$

The basis functions $\tilde{\phi}_\mu$, weighted by coefficients $C_{\mu i}$, are generally exponential functions with radial dependence of either e^r or e^{r^2}. Although the former (referred to as Slater-type orbitals[90]) is more accurate, the latter (Gaussian-type orbitals[91-92]) is nonetheless generally favored for its higher computational efficiency[93]. The collection of all basis functions used in a particular calculation is referred to as a *basis set*. Upon the introduction of these terms, equation (14) may be rewritten in matrix form as the Roothaan equation

$$\mathbf{FC} = \mathbf{SC}\varepsilon, \tag{16}$$

where **F** and **S** are the Fock and overlap matrices, respectively[94-95]. The Fock matrix serves as the Hamiltonian operator, while the overlap matrix is in essence a normalizing matrix used in orthogonalization of the Fock matrix. These matrices are given by

$$\mathbf{F}_{\mu\nu} = \int \tilde{\phi}_\mu^*(\boldsymbol{x}_k) f(\boldsymbol{x}_k) \tilde{\phi}_\nu(\boldsymbol{x}_k) d\boldsymbol{x}_k \tag{17}$$

$$\mathbf{S}_{\mu\nu} = \int \tilde{\phi}_\mu^*(\boldsymbol{x}_k) \tilde{\phi}_\nu(\boldsymbol{x}_k) d\boldsymbol{x}_k \tag{18}$$

Because **F** and **C** are interdependent, at this point the SCF procedure begins: **F** and **C** are iteratively varied, with each updating the other upon each iteration, until they converge to a desired level of accuracy. This yields orbital occupation and orbital energies, typically for the ground-state configuration. The variational theorem guarantees that these methods cannot underestimate the true energy. It should be noted that base Hartree-Fock theory is deeply flawed in its failure to consider electron correlation; post-Hartree-Fock methods aim to correct this, but another quite popular approach exists.

All of the methods discussed thus far are iterative approaches to find the wavefunction $\psi(\boldsymbol{x})$ which minimizes the total energy E. Density functional theory (DFT), however, tackles the Schrödinger equation by seeking the electron density $\rho(\boldsymbol{r})$ which minimizes the total energy[96-98]. The Hohenberg-Kohn theorem demonstrates that the ground-state electronic properties of a system

depend only on the electron density, making this approach fully tractable[99-101]. Indeed, DFT can deliver far more accurate results than base Hartree-Fock theory with comparable computational cost[102]. Expressing the energy as a *functional* of electron cleverly reduces all energy terms for which an analytical expression is not known into a single parameter $E_{XC}[\rho(\boldsymbol{r})]$:

$$E[\rho(\boldsymbol{r})] = -\frac{1}{2}\sum_i \langle\phi_i|\nabla^2|\phi_i\rangle + \sum_A \int \frac{Z_A\rho(\boldsymbol{r})}{|\boldsymbol{R}_A-\boldsymbol{r}|}d\boldsymbol{r} + \frac{1}{2}\iint \frac{\rho(\boldsymbol{r})\rho(\boldsymbol{r}')}{|\boldsymbol{r}-\boldsymbol{r}'|}d\boldsymbol{r}d\boldsymbol{r}' + E_{XC}[\rho(\boldsymbol{r})] \qquad (19)$$

The first three terms in this equation represent the kinetic energy of an analogous system of *non-interacting* electrons and the Coulombic energies for the attractive nuclear-electronic interactions and the repulsive two-electron interactions[96]. The unknown parameter $E_{XC}[\rho(\boldsymbol{r})]$, termed the exchange-correlation functional, is the core hurdle in DFT. Thus, the choice of functional is a major determinant in the accuracy of the computation results.

Even though the explicit forms of exchange-correlation functionals can vary quite drastically, the most common functionals fall into one of several major categories. Local density approximation (LDA) functionals[96, 103] use only the local electron density $\rho(\boldsymbol{r})$ at each point $\boldsymbol{r}$. Generalized gradient approximation[104-107] (GGA) and meta-GGA[108-110] functionals additionally incorporate the gradient $\nabla\rho(\boldsymbol{r})$ and the Laplacian $\nabla^2\rho(\boldsymbol{r})$ for additional information. Hybrid functionals[111-117] make use of the Hartree-Fock exchange energy expression. Finally, hybrid meta-GGA functionals[118-120] utilize all of the terms discussed above and are extremely accurate, but greatly increase the computational cost of the DFT calculation. As a result, GGA (e.g., PBE[105]) or hybrid (e.g., B3LYP[113-117]) functionals are generally used unless extreme accuracy is desired.

It should be noted that while DFT deals with electron density rather than the wavefunction, it is still fundamentally a variational method! The most common implementation of DFT, often referred to as Kohn-Sham density functional theory[96, 102] (KS-DFT), expresses equation (14) as

$$\hat{h}_{KS}(\boldsymbol{r}_k)\phi_i(\boldsymbol{r}_k) = \varepsilon_i\phi_i(\boldsymbol{r}_k) \qquad (20)$$

where the one-electron Hamiltonian operator $\hat{h}_{KS}$ is given as

$$\hat{h}_{KS} = -\frac{1}{2}\nabla^2 + \sum_A \int \frac{Z_A \rho(\boldsymbol{r})}{|\boldsymbol{R}_A - \boldsymbol{r}|} d\boldsymbol{r} + \int \frac{\rho(\boldsymbol{r}')}{|\boldsymbol{r} - \boldsymbol{r}'|} d\boldsymbol{r}' + V_{XC}(\boldsymbol{r}), \quad (21)$$

consisting of kinetic energy, nuclear-electronic attraction, two-electron repulsion, and exchange-correlation potentials, respectively. The SCF procedure in KS-DFT is applied in an analogous manner to that in Hartree-Fock theory[78] to achieve convergence of the orbital occupation and orbital energies, making KS-DFT (and, indeed, DFT in general) a variational method.

Once the orbital occupation has been determined, properties such as the partial atomic charges may be calculated. There are certainly many approaches for accomplishing this; Mulliken population analysis is a common technique which assigns partial atomic charges directly based on the orbital occupation, distributing partial charge evenly in the case of orbital overlap[121-122].

More sophisticated techniques include the electrostatic potential (ESP) method, which attempts to assign partial charges such that the proper ESP at various points is replicated around the molecule[123-127]. The Bader method of partial charge analysis defines a series of zero-flux surfaces around atomic centers and integrates the electron density within the volumes defined by these surfaces in order to find the partial charge on each atom[128-132]. These more sophisticated techniques may present better choices for studies desiring extremely high-accuracy partial atomic charges. However, when only approximately accurate values are needed, a careful selection of basis set will render Mulliken population analysis a viable option.

2.2.2. Force Field Methods

When many atoms are present, force field methods are excellent tools for examining the behavior of a molecular system[72, 133]. Such methods are generally categorized as either molecular *mechanics* or molecular *dynamics*, with the clear distinction being the absence or presence of time

evolution, respectively[134-136]. In either case, however, force field methods study the variation in energy as a function of molecular geometry and atomic positions.

Generally, this variation is implicitly studied by way of a potential energy surface (PES), giving the relationship between the configurational energy of a molecule and its geometrical parameters[137-141]. In the case of water, for example, the PES captures the variation of energy with respect to O-H bond length and H-O-H bond angle. Of course, a more complicated species would give rise to a PES which cannot be easily visualized. With this in mind, a more versatile view of the dependence of energy on geometry and position takes the form of potential energy *functions* (PEF), a collection of which constitute a *force field*.

There are, broadly, two types of PEF: bonded and non-bonded interactions. The simplest bonded interactions are fairly intuitive, including such terms as bond stretching, bond angle bending, and dihedral angle torsion. Bond stretching energy, E_l, may be modeled as a harmonic potential, although this gives incorrect limiting behavior at large interatomic distances. A more appropriate choice of equation, generally referred to as the Morse potential[142-144], takes the form

$$E_l = D\left\{1 - \exp\left[\sqrt{k_l/2D}\,(l - l_0)\right]\right\}^2, \tag{22}$$

where D is the dissociation energy, k_l is the force constant associated with the potential well, and l_0 is the equilibrium bond length.

Bond angle bending energy, E_θ, may also be modeled as a harmonic potential close to the equilibrium bond angle, but this quickly fails at larger bond angles. For this reason, a *cosine* harmonic potential is often employed, commonly expressed as

$$E_\theta = \frac{1}{2} k_\theta (\cos\theta - \cos\theta_0)^2. \tag{23}$$

In a similar vein to the bond stretching potential, here k_θ represents the force constant associated with the angle bending and θ_0 represents the equilibrium bond angle.

Dihedral angle torsion energy, E_ϕ, requires a more complicated expression, owing to the fact that multiple stable dihedral angles exist for a given molecule. Since one minimum alone will not suffice, this term is frequently expressed as a sum over several terms. For example, a commonly used expression for this potential takes the form

$$E_\phi = \frac{1}{2}\sum k_\phi[1 + \cos(n\phi - \phi_0)], \tag{24}$$

with k_ϕ again serving as the force constant. ϕ_0 is, however, not directly the equilibrium torsion angle, but simply a minimum on the force curve of multiplicity n.

While other bonded interaction terms are sometimes employed – such as out-of-plane bending or cross terms like stretch-bend potentials – the three mentioned above are the most common and often the most important. The *non-bonded* interactions, by contrast, are nearly always limited to electrostatic potential and van der Waals potential terms. The former of these is simply a Coulombic interaction potential of the familiar form

$$E_{el} = q_A q_B / \epsilon R_{AB}, \tag{25}$$

where q_i represents the partial charge of atom i, ϵ represents the effective dielectric constant, and R_{AB} represents the interatomic distance. This expression demonstrates the importance of obtaining an accurate estimate of the partial atomic charges from EST. Quicker partial charge estimation schemes such as charge-equilibration[145] (QEq) or Gasteiger partial charges[146-147] can be insufficient for correct determination of energies based on molecular mechanics.

The van der Waals potential consists of attractive and repulsive energy contributions: the short-range interaction is strongly repulsive and follows an approximately exponential function, while at relatively long separation the attractive term proportional to R_{AB}^{-6} dominates. Combining these dependencies, a common expression (generally termed the "exponential-6" or Buckingham potential[148]) of the van der Waals interaction energy E_{vdW} becomes

$$E_{vdW} = \alpha \exp(-\beta R_{AB}) - \gamma / R_{AB}^6, \quad (26)$$

with α, β, and γ being empirically fitted parameters contained within the choice of force field. Although this expression is very accurate at most interatomic separations, it predicts unphysically attractive behavior at extremely short separations. An alternate expression which avoids this, best known as the Lennard-Jones potential, takes the form below[149]:

$$E_{vdW} = E_0[(R_0/R_{AB})^{12} - 2(R_0/R_{AB})^6] \quad (27)$$

This formulation is quite appealing in part because it avoids the unphysical behavior encountered by the Buckingham potential at extremely short interatomic separations; it is also significantly quicker to compute and contains within it the most salient features of the force curve – i.e., the equilibrium interatomic separation R_0 and minimum energy E_0.

An important application of the PEF defined in equations (22)-(27) is the minimization of the energy of a molecule on the PES. Such a procedure, termed geometry optimization, relies on gradient techniques such as the steepest descent or Newton-Raphson methods[150-152]. Although these approaches are designed to seek *minima* on the potential energy surface, an interesting application allows for transition states to be studied. Transition states exist as saddle points on the PES, being a minimum in all but one geometrical dimensions[153]. Molecular mechanics studies of these states require the Hessian matrix, an analytic formulation of which can be costly to obtain (if possible at all). Studying them can thus be considerably more difficult than geometry optimization.

The considerations discussed heretofore generally fully capture the scope of molecular *mechanics*; when considering the time evolution of a molecule or group of molecules, however, molecular *dynamics* necessitates several additional expressions. To begin, Newton's equations of motion are integrated and often expanded as a Taylor expansion of position as a function of time:

$$\boldsymbol{r}(t + \delta t) = 2\boldsymbol{r}(t) - \boldsymbol{r}(t - \delta t) + \frac{1}{m}\boldsymbol{F}(t)\delta t^2 \quad (28)$$

This second-order expansion, known as the Verlet algorithm[154], is noteworthy in that it is independent of atomic velocities. Instead, this algorithm depends only on the atomic positions from the current and previous timesteps and the forces upon each atom at the current timestep. Just as the partial atomic charges highlight the importance of EST to force field methods, so too does the Verlet algorithm expressed thusly highlight the importance of accurate PEF expressions to molecular dynamics. Naturally, there exist many variants of this algorithm (velocity Verlet, leapfrog integration, etc.[155-157]), but they all share the important dependence upon the PEF expressions that the Verlet algorithm displays.

As a system evolves, its properties will necessarily evolve as well. Some properties, however, ought to remain constant: the temperature, for example, is often a system parameter. It therefore should, on average, remain constant as the system evolves. System controls such as thermostats and barostats are often used to regulate parameters that are used to define the system.

One possible choice for these regulators are the Berendsen thermostat and barostat[158-160]. This thermostat regulates temperature by scaling the atomic velocities v_i of timestep i by a factor λ, given by

$$\lambda = [1 + (\delta t/\tau_T)(T_0/T)]^{1/2}, \tag{29}$$

where τ_T is a coupling constant of the system to a heat bath of constant temperature T_0. The ratio of the temperatures between the heat bath and the system is therefore the characteristic parameter which governs the scaling of the atomic velocities and thus the temperature regulation. The Berendsen barostat works analogously, maintaining constant system pressure by scaling the system volume by a parameter η, given by

$$\eta = [1 - \beta(\delta t/\tau_P)(P_0 - P)]^{1/3}. \tag{30}$$

Here β is simply the isothermal compressibility of the system, while τ_P and P_0 are constants associated with a pressurized reservoir analogous to the heat bath of the Berendsen thermostat. Like the Verlet algorithm, there are also many forms of thermostats and barostats (Andersen, Nosé-Hoover, etc.[161-165]).

2.2.3. Dissipative Particle Dynamics

Since molecular mechanics and molecular dynamics exclude explicit consideration of the electronic motion or orbital occupation (and thus also exclude any treatment of the Schrödinger equation), these methods can model large numbers of atoms quite effectively. When studying the time evolution of a system of several hundred or more atoms, however, even the methods outlined above become impractical. At this scale, it becomes necessary to employ some level of coarse-graining – that is, the reduction of a group of atoms into a single particle.

A powerful tool for analyzing the time evolution of a system of many atoms and molecules is dissipative particle dynamics[166-169] (DPD). As in all coarse-grained techniques, DPD reduces groups of many atoms into particles, commonly referred to as *beads*. Any DPD simulation will likely have at least two bead types, where each type represents a particular collection of atoms with specific properties. It should be noted that all beads in the system have the same mass[169]; therefore, a judicious set of bead type definitions from the original system becomes highly important. Additionally, in order to preserve a sense of chemical identity for the beads in the system, characteristics such as the stiffness of the different atomic/molecular species and the miscibility of each *pair* of species ought to be assigned properly to the molecules.

The time evolution of the DPD system originates in the presence of three forces exerted on the particles[168-169]. For any given particle i, the force upon this particle is given by

$$\boldsymbol{F}_{\mathrm{i}} = \sum_{\substack{\mathrm{j}\neq\mathrm{i} \\ r<r_c}} \left(\boldsymbol{F}_{\mathrm{ij}}^{C} + \boldsymbol{F}_{\mathrm{ij}}^{D} + \boldsymbol{F}_{\mathrm{ij}}^{R}\right). \tag{31}$$

As indicated by the summation bounds, each of these forces extends to all particles within a sphere of cutoff radius r_c. Particles outside of this cutoff radius are considered to have no interaction with particle i. The magnitude of r_c is frequently taken to be unity; however, in this discussion it will be left in its original form.

The first of the forces in equation (31), $\boldsymbol{F}_{\mathrm{ij}}^{C}$, is a conservative force which describes soft repulsion between particles i and j. For all $r_{\mathrm{ij}} < r_c$, its functional form is simple:

$$\boldsymbol{F}_{\mathrm{ij}}^{C} = a_{\mathrm{ij}}\left(1 - r_{\mathrm{ij}}/r_c\right)\hat{\boldsymbol{r}}_{\mathrm{ij}} \tag{32}$$

Of course, for $r_{\mathrm{ij}} \geq r_c$, the force reduces to zero. The prefactor a_{ij} is often termed the repulsion parameter; its magnitude is related to the Flory-Huggins χ-parameter through a simple linear scaling relationship dependent on ρ, the bead density[169]. For $\rho = 3.0$, this relation takes the form

$$a_{\mathrm{ij}} = 25 + 3.5\chi_{\mathrm{ij}}. \tag{33}$$

Note that the repulsion parameters are symmetrical (i.e., $a_{\mathrm{ij}} = a_{\mathrm{ji}}$).

Because the chemical identity of the species in the original system is primarily described by the repulsion parameter, a DPD simulation can only correspond accurately to a given physical system insofar as its repulsion parameters correspond accurately to the real miscibility between these species. As a consequence, accurately determining the χ-parameters between each pair of identifiable species in the original system directly impacts the extent to which the DPD simulation properly captures the behavior of the physical system; as mentioned earlier, this important goal will form the basis of Chapter 3.

The second and third forces in the DPD framework, represented by $\boldsymbol{F}_{\mathrm{ij}}^{D}$ and $\boldsymbol{F}_{\mathrm{ij}}^{R}$, are termed the dissipative and random forces, respectively. Together, these forces constitute a thermostat for the simulation system: the dissipative force introduces a drag proportional to the relative velocity

$\boldsymbol{v}_{\mathrm{ij}}$ between particles i and j which serves to reduce the beads' velocities, while the random force – also referred to as a random *thermal* force – serves to replicate the presence of atomic collisions and increase the beads' velocities to the system. The functional forms of these forces are simple:

$$\boldsymbol{F}_{\mathrm{ij}}^{D} = -\gamma\left(1 - r_{\mathrm{ij}}/r_c\right)^2\left(\hat{\boldsymbol{r}}_{\mathrm{ij}} \cdot \boldsymbol{v}_{\mathrm{ij}}\right)\hat{\boldsymbol{r}}_{\mathrm{ij}} \tag{34}$$

$$\boldsymbol{F}_{\mathrm{ij}}^{R} = \sigma\left(1 - r_{\mathrm{ij}}/r_c\right)\zeta_{\mathrm{ij}}\Delta t^{-1/2}\hat{\boldsymbol{r}}_{\mathrm{ij}} \tag{35}$$

Again, these forces extend only over the range $r_{\mathrm{ij}} < r_c$. The factor ζ_{ij} is a random variable, chosen independently at each timestep for each pair of interacting particles, with statistical properties

$$\langle\zeta_{\mathrm{ij}}\rangle = 0 \text{ and } \langle\zeta_{\mathrm{ij}}^2\rangle = 1. \tag{36}$$

For statistical reasons, the inclusion of the factor $\Delta t^{-1/2}$ in equation (35) is essential. (A detailed explanation of the origin of this factor is, however, beyond the scope of the present work.)

The amplitudes γ and σ of these two forces are related through the so-called fluctuation-dissipation theorem of DPD, which gives rise to the governing relationship

$$\sigma^2 = 2\gamma k_B T. \tag{37}$$

A justification for this relationship requires examination of the Fokker-Planck equation[168, 170-172]

$$\partial\rho/\partial t = \mathcal{L}_C\rho + \mathcal{L}_D\rho, \tag{38}$$

where $\rho = \rho(\boldsymbol{r}_i, \boldsymbol{p}_i, t)$ represents the probability distribution function corresponding to the system occupying position state $\boldsymbol{r}_i$ and momentum state $\boldsymbol{p}_i$ at time t. The operators $\mathcal{L}_C$ and $\mathcal{L}_D$ are more complicated; the former captures the conservative force described by equation (32), while the latter captures both the dissipative and the random forces described by equations (34) and (35). These operators are given by the following expressions:

$$\mathcal{L}_C = -\left(\sum_i \frac{\boldsymbol{p}_i}{m}\frac{\partial}{\partial \boldsymbol{r}_i} + \sum_i\sum_{j\neq i}\boldsymbol{F}_{\mathrm{ij}}^{C}\frac{\partial}{\partial \boldsymbol{p}_i}\right) \tag{39}$$

$$\mathcal{L}_D = \sum_i\sum_{j\neq i}\left(1 - r_{\mathrm{ij}}/r_c\right)^2\hat{\boldsymbol{r}}_{\mathrm{ij}}\frac{\partial}{\partial \boldsymbol{p}_i}\left[\gamma\left(\hat{\boldsymbol{r}}_{\mathrm{ij}} \cdot \boldsymbol{v}_{\mathrm{ij}}\right) + \frac{1}{2}\sigma^2\hat{\boldsymbol{r}}_{\mathrm{ij}}\left(\frac{\partial}{\partial \boldsymbol{p}_i} - \frac{\partial}{\partial \boldsymbol{p}_j}\right)\right] \tag{40}$$

Often it is useful for the equilibrium probability distribution ρ_{eq} – that is, the solution of setting equation (38) equal to zero – to be identical to the Boltzmann distribution. In such a case, the thermodynamics of the system may then be expressed accurately through the canonical ensemble of statistical mechanics, as previously described in equations (10) and (11). Requiring that equation (37) be satisfied is sufficient to ensure that ρ_{eq}, the steady-state solution to equation (38), will move toward the Boltzmann distribution $\rho = \exp(-\varepsilon_i/k_B T)$.

The actual implementation of molecular dynamics (i.e., time evolution) into the DPD system is typically accomplished through a modified form of the velocity Verlet algorithm[169]. Although there are several important distinctions in practice, the general form of the algorithm is similar enough to that presented in in equation (28) that further discussion will not be presented here. In any case, it should be noted that the most crucial distinction between molecular dynamics as implemented on a fully atomistic basis (i.e., as discussed earlier) and molecular dynamics as implemented in coarse-grained techniques such as DPD lies in the definition of the forces acting on the constituent species. Since coarse-grained techniques simplify actual molecules into particles, the force expressions in equations (22)-(27) are inapplicable. Instead, the expressions described in in equations (32), (34), and (35) must be used.

As a final note on the theoretical background of this work, there exists a natural progression connecting all of the areas discussed thus far in Chapter 2. Computational modeling and simulation of a micelle system exists at far too large of a scale for EST methods and is even too unwieldy for fully atomistic methods in molecular dynamics to handle. Coarse-grained techniques, however, necessarily strip the constituent species of chemical identity, so properties must be assigned to the particles in such techniques as DPD to recapture as much of this identity as possible.

These properties, such as interspecies miscibility, may be determined through the use of methods like (fully atomistic) molecular mechanics. The calculation of accurate properties from these force field methods in turn relies on EST techniques for the optimization of force field parameters and assignment of partial atomic charges, among many others. However, since thermodynamic properties such as the average interaction energy of a pair of molecules depend on all available molecular configurations, statistical mechanics must be employed to obtain a proper value of such quantities from a large sample of configurational space.

3. COMPUTATIONAL ESTIMATION OF FLORY-HUGGINS χ-VALUES

This chapter was adapted from a 2018 ChemPhysChem *publication by the author*[61].

The foregoing theoretical foundations serve to underscore the complexity of creating accurate computational models of large systems like MCMs. As a consequence, it seems natural to approach such a study in a hierarchical manner: first, analyses based in EST and atomistic molecular mechanics will be performed to study the properties of the chemical species at hand. Using these results, a coarse-grained simulation of the time evolution of a polymer-solvent mixture may be conducted to study the self-assembly of a micelle system and the resultant structures as a function of polymer composition.

The present work focuses on modeling MCMs composed of polymers with three distinct blocks of solvophilicity. Along the lines of the piecemeal approach outlined above, preliminary studies in this work have been divided into two major thrusts. A rigorous framework for computationally estimating the χ-parameter was developed, with satisfactory results compared to several systems of experimental study. Separately, an idealized DPD study (i.e., using χ-values specifically chosen to guarantee three distinct solvophilicities) was conducted in order to examine the effect of characteristics of polymer architecture such as the lengths and length ratios of the three polymer chain blocks. There exists a wealth of existing studies which demonstrate the applicability of DPD for the study of micelle structures[51, 60-61, 173-180], making this an ideal choice.

Previous studies related to the χ-parameter have highlighted the large spread of values generated by experimental measurements (e.g., by inverse gas chromatography[181-183], differential scanning calorimetry[184-187], or small-angle neutron scattering[188-191]), necessitating very precise control of experimental conditions. To compound all of these difficulties, even when such

precision is possible, there is no guarantee that the requisite data (Hildebrand or Hansen solubility parameters, cohesive energy densities, etc.) are known accurately, if at all.

Due to these significant limitations of experimental techniques for estimating the χ-parameter, it may be advantageous to consider computational techniques in studying the miscibility of two species. For one, calculating the χ-parameter through computer simulations instead of experimentation would greatly expedite the process of determining the miscibility of a given pair of molecules. In addition, the development of a temperature- and composition-sensitive model for estimating the χ-parameter would pave the way for full constructions of phase behavior.

In this chapter, a molecular modeling approach is presented which allows the χ-parameter to be estimated for a given pair of molecules. Combined with the existing theories and molecular modeling techniques, such as Flory-Huggins theory, density functional theory, molecular mechanics/dynamics simulation, and configurational statistics, this approach establishes a new procedure of normalizing the interaction energies using the molecular volume enclosed by the Connolly surface. This creates an interaction energy density which is analogous to, but distinct from, the cohesive energy density. From this study, it is apparent that this newly developed procedure produces accurate estimations for polymer miscibility.

As discussed in greater detail in Chapter 2.1, the Flory-Huggins χ-parameter is a useful tool for analyzing the miscibility of two chemical species. Unfortunately, most of the traditional experimental methods have presented challenges. For example, the χ-parameter between two polymers may be estimated via inverse gas chromatography[181-183] (IGC) by first determining the miscibility between a probe species (represented by 1) and each of two polymer species (represented by 2 and 3). These interactions can be determined according to the expression[181, 183]

$$\chi_{12} = \ln\left(\frac{273.15Rv_2}{V_g^{\circ}V_1P_1^{\circ}}\right) - 1 + \frac{V_1}{M_2v_2} - \left(\frac{B_{11}-V_1}{RT}\right)P_1^{\circ}, \quad (41)$$

where V_1, $P_1°$, and B_{11} represent the molar volume, saturated vapor pressure, and second virial coefficient (in the gaseous state), respectively, of the probe species. v_2 and M_2 represent the specific volume and molecular weight of a polymer, respectively. The parameter $V_g°$ represents the reduced specific retention volume. An analogous expression exists for χ_{13}. Although many of these parameters can be determined via experiment to satisfactory accuracy, Al-Saigh and Munk have noted that the parameters V_1, $P_1°$, and B_{11} are all subject to a relatively large amount of uncertainty[181], leading to uncertainty in χ_{12} and χ_{13}.

An expression that avoids the use of these parameters can be derived as well[181]:

$$\chi_{23} = \frac{1}{\mu\phi_2\phi_3}\left[\ln\left(\frac{V_{g,\text{blend}}}{w_2v_2+w_3v_3}\right) - \phi_2\ln\left(\frac{V_{g,2}}{v_2}\right) - \phi_3\ln\left(\frac{V_{g,3}}{v_3}\right)\right] \quad (42)$$

Here μ is a simple volumetric ratio and w_i and ϕ_i are the weight and volume fractions of species i, respectively. However, even if this expression is employed, the very low values of the retention volume V_g lead to large error in the χ-value[181]. For these reasons, although IGC offers an avenue for estimating the χ-parameter, it presents prohibitively large uncertainty to be a practical method.

It is also possible to estimate χ using small-angle neutron scattering[188-191] (SANS). This procedure measures the angle of refraction of neutrons through an experimental medium, in this case a solution of two polymer species, while varying angle of incidence in a manner analogous to small angle x-ray scattering. The interaction parameter between the two species can be calculated using the equation[189]

$$\chi_{\text{AB}} = \frac{1}{2}\left[\left[\phi Z_{\text{A}}\big(P(0) + NQ(0)\big)\right]^{-1} - (\phi Z_{\text{A}})^{-1} - \big((1-\phi)Z_{\text{B}}\big)^{-1}\right], \quad (43)$$

where ϕ represents volume fraction of B in A, Z_A and Z_B are the degree of polymerization of the two species, N represents the total number of B polymer chains per unit volume, and $P(q)$ and

$Q(q)$ represent the intramolecular and intermolecular components of scattering, respectively. The scattering vector q can be expressed using the equation

$$q = \frac{4\pi}{\lambda}\sin\left(\frac{\theta}{2}\right), \tag{44}$$

where λ represents the wavelength of the neutrons and θ represents scattering angle. Ito, Russell, and Wignall note that ϕ, Z_A, and Z_B are known from the composition of the solution and from the synthesis of each species. Thus, extrapolating $Q(q)$ at $q = 0$ yields the χ-parameter[189].

On the other hand, it is well established that χ varies with temperature. In particular, χ may be expressed as the sum of a temperature-independent entropic term and a temperature-dependent enthalpic term[71, 192], as shown below:

$$\chi(T) \approx A + \frac{B}{T}, \tag{45}$$

Determining an empirical equation for χ of this form requires that SANS be performed at each step in a range of temperatures and the resulting χ-values be fitted as a linear function of inverse temperature. For this reason, although SANS produces useful miscibility data, the time needed to prepare and test solutions at each relevant temperature makes it a cumbersome and impractical method of determining χ.

This study aims to revise the theory by utilizing molecular modeling methods. The initial step was to prepare molecules for miscibility analysis, building molecular structures in Cerius2 (Molecular Simulations Inc., San Diego, CA, USA). Rudimentary partial charge analysis and coarse geometry optimization were carried out via the QEq method[145] and molecular mechanics[193], respectively. Coarse geometry optimization via molecular mechanics in this stage improves convergence in the next, more robust, calculations using Mulliken population analysis and DFT.

After the coarse geometry optimization, the DFT geometry optimization and orbital occupation analysis were performed using Jaguar[194] in Maestro (Schrödinger, New York, USA)

with the GGA functional PBE and the basis set 6-31G** to refine the molecular structures. The atomic partial charges were obtained using Mulliken population analysis[121]. The SCF procedure was performed with a convergence threshold of 5×10^{-5} hartree.

Next, molecular dynamics simulations were performed on these molecules via the Forcite module of Materials Studio[195] (Accelrys, San Diego, USA) to sample low-energy conformations, which were employed for the miscibility analysis. These simulations were carried out at 298 K with a time step of 1 fs for a total simulation time of 50 ps. It should be noted that while 50 ps is nominally too small a timescale for molecular dynamics, in this case the limited conformational space of the small molecules being considered renders the use of a longer timescale unnecessary. A trajectory file was generated by saving a snapshot of the structure every 500 steps. The energy was calculated using Dreiding force field[196] and an NVT ensemble with random initial velocities. These same procedures were repeated for a second molecule with the same conditions. The process flow of the initial preparation of one molecule is shown in Figure 1.

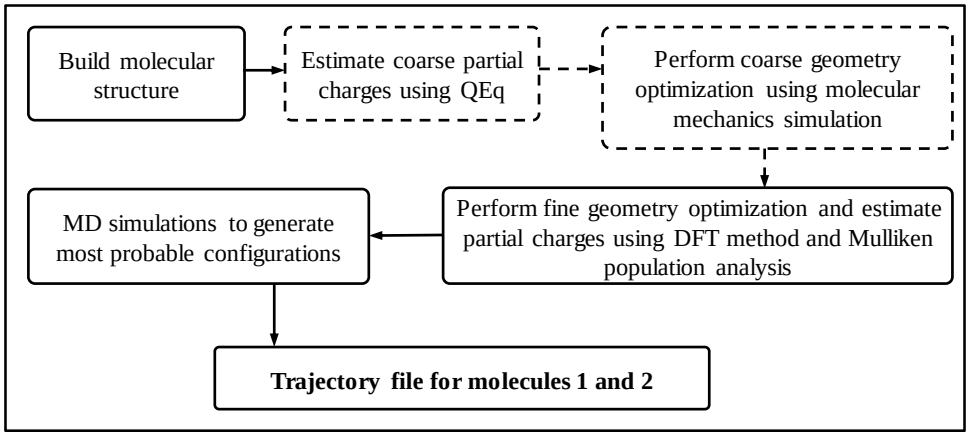

Figure 1. Preparation of molecules for miscibility analysis. Steps shown with a dashed border are optional, depending on the conformational diversity of the particular species.

The Dreiding force field was selected because it has been extensively demonstrated in previous work by the authors to be accurate and reliable for organic molecular systems[197-202].

Further, the attractively simple typing rules and implementation of force expressions makes the molecular dynamics simulations proceed efficiently.

With molecular structures for molecules 1 and 2 stored in trajectory files, miscibility simulations were performed using the Blends module of Materials Studio at 298 K. When undertaking this calculation, 1×10^6~1×10^7 samples were collected with an energy bin width of 0.02 kcal/mol. In order to determine the coordination number of each pairing of molecules, 1×10^4 cluster samples were taken with 20 iterations per cluster. The 1,000 lowest-energy sample frames were retained for further analysis. Similar to the Forcite calculation, here the Dreiding force field was employed to determine intermolecular interaction energies.

It should be noted that Blends module of Materials Studio has been observed to yield results with large variation[203-205]. To combat this, post-processing and data analysis steps developed by the authors were employed which improved the accuracy of the resultant χ-values significantly. A molecular mechanics task was executed in Perl within Materials Studio, as shown in Figure 2. During this process, a secondary geometry optimization was performed on each individual molecule and pair of molecules in the lowest-energy frames output by the Blends simulation, which allowed us to determine the energies and Connolly volumes of both the individual molecules and the pair of these two molecules.

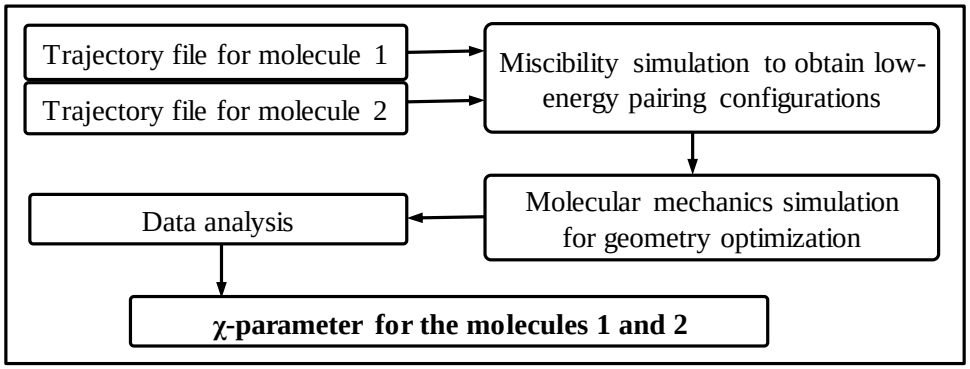

Figure 2. Miscibility simulations are performed using the trajectories as inputs. The simulation results are analyzed to obtain χ_{12}.

Once this was completed for each of the 1,000 lowest-energy frames, additional data refinement was carried out, in which the interaction energies were normalized by the volume enclosed by the Connolly surface[206-211] and then averaged via Boltzmann statistics. These two steps result in a more realistic picture of the interaction energy at any given point in time and fairly consider the effect that molecular size has on the apparent interaction strength.

This technique of Connolly volume normalization (CVN) is proposed on the basis that a direct calculation of the interaction energies between molecules does not fairly assess intermolecular interaction. Proper consideration of this possible issue cannot be assumed while utilizing the Blends module alone[212]. For example, two large molecules with weak interactions can appear to have the same affinity for one another that two small molecules with strong interactions have, which would lead to faulty conclusions about the segment-wise miscibility of these two species. Thus, in the expression for the Flory-Huggins χ-parameter between species 1 and 2 as shown in equation (6), an alternative expression is proposed for the exchange energy between the unmixed and mixed states, Δw_{12}:

$$\Delta w_{12} = \frac{1}{2} V_{\text{ref}} \{ (Z_{12} + Z_{21})(E_{12}^*/V_{12}) - [Z_{11}(E_{11}^*/V_{11}) + Z_{22}(E_{22}^*/V_{22})] \} \tag{46}$$

Here V_{ij} refers to the volume enclosed by the Connolly surface over the combined pair of molecules i and j. The reference volume V_{ref} and Boltzmann-averaged energy E^* are given as

$$V_{\text{ref}} = \phi_1 V_1 n_1^{-1} + \phi_2 V_2 n_2^{-1} \tag{47}$$

and

$$E^* = \frac{1}{\text{Q}^*} \sum_{k=1}^{N_\text{f}} E_k e^{-E_k/RT}, \tag{48}$$

respectively, where n_i refers to the degree of polymerization of species i, N_f is the number of low-energy frames returned from the blends calculation and Q^* is the pseudo-partition function of the corresponding system of N_f frames, as discussed in Chapter 2.1.

$$\mathrm{Q}^* = \sum_{k=1}^{N_\mathrm{f}} e^{-E_k/RT}, \tag{49}$$

Some discussion and justification of the new terms in equation (13) is warranted. The interaction energy E_{ij} is weighted by the Boltzmann factor to become E_{ij}^* in order to capture the statistical mechanical probability that would favor low-energy frames in a physical system. Further, the interaction energy density E_{ij}^*/V_{ij} is fundamentally a size-mitigation term. The contribution of an interaction E_{11}^* to the overall exchange energy Δw_{12} may be overestimated if the species 1 is particularly large. It would be unclear how much of that contribution arises from the species' *size* and how much arises from its *intrinsic interaction strength*. Therefore, the energy is normalized by the size of the molecule such that molecules only contribute to Δw_{12} based on their intrinsic interaction strength.

The introduction of the volume normalization term renders the expression dimensionally inconsistent with Δw_{12}, so some volume prefactor is necessary. The χ-parameter is nominally a *segment* interaction parameter[213], so to preserve this quality the volume prefactor should represent the "average" segment volume. $V_1 n_1^{-1}$ gives the Connolly volume of an individual segment of species 1 (and likewise for $V_2 n_2^{-1}$). Then V_ref is computed as the volume average of the individual segments, to obtain a representative "average" segment volume.

In the present work, miscibility analyses were performed on four principal systems. The first system is a blend consisting of poly(epichlorohydrin) (PECH, Figure 3) and poly(methyl acrylate) (PMA, Figure 3). The second consists of polyethylene glycol (PEG, Figure 3) and poly(methyl methacrylate) (PMMA, Figure 3). The last system is a triblock copolymer consisting of poly(acrylic acid) (Figure 3), poly(6-(4-formylphenoxy)hexyl acrylate) (Figure 3), and poly(pentafluorostyrene) (Figure 3) as blocks A, B, and C, respectively. All of the χ-parameters reported in this study correspond to mixtures with equally divided volume ratios.

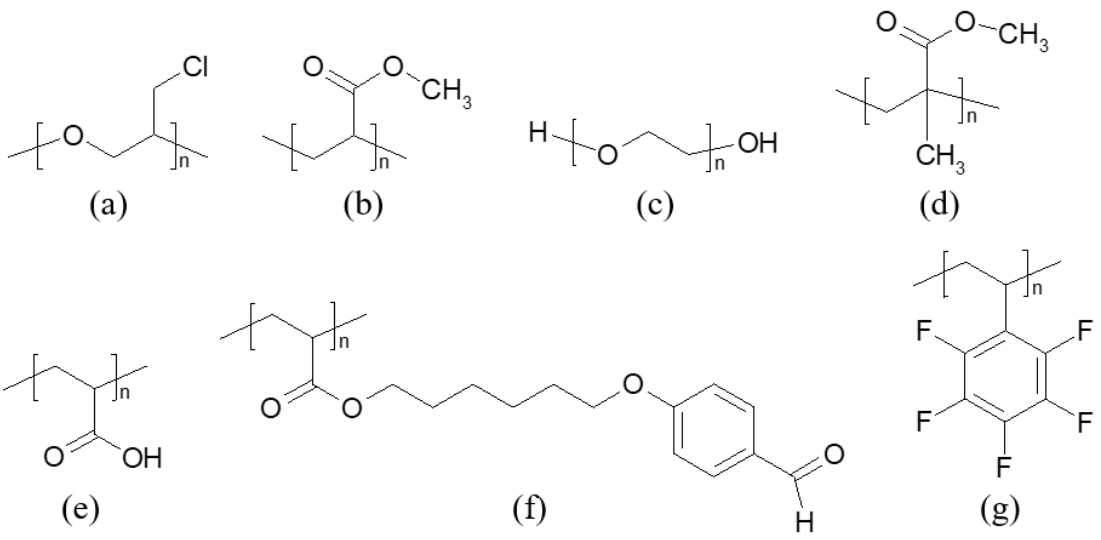

Figure 3. Chemical structures of species studied in this work: (a) poly(epichlorohydrin), (b) poly(methyl acrylate), (c) polyethylene glycol, (d) poly(methyl methacrylate), (e) poly(acrylic acid) (block A), (f) poly(6-(4-formylphenoxy) hexylacrylate) (block B), and (g) poly(pentafluorostyrene) (block C).

Finally, to further test the accuracy of this method with respect to experimental results, DPD simulations were carried out using the χ-values obtained as detailed above for the triblock copolymer system described in Figure 3. Using periodic boundary conditions in a simulated box size of 30x30x30 at a reduced temperature of 1.0, the simulation required a duration of 2.5×10^4 reduced DPD units with a timestep of 0.05 to reach equilibrium. Temperature and pressure were monitored to ensure that the system reached equilibrium. The system was composed of 10% triblock copolymer with a reduced architecture of $A_5B_{11}C_{13}$ (relative to the real experimental system of $A_{45}B_{110}C_{135}$) and 90% water with bead density ρ = 3. Repulsion interaction parameters a_{ij} were calculated directly from the χ_{ij}-values through equation (33), as outlined by Groot and Warren[169]. All dissipation parameters were equal to 4.5.

As previously stated, miscibility simulations were performed for a blend of PECH (Figure 3) and PMA (Figure 3). This system has previously been studied via IGC experiments[181-182]. Table 1 displays the minimum, average, maximum, and standard deviation of the experimental χ-values

obtained via IGC in comparison with computational results using both the updated model from equation (46) and the traditional Flory-Huggins formulation from equation (4).

Table 1. Comparison of χ-parameter for PECH-PMA pair between simulation and experiment.

	χ (experimental, via IGC[181-182])			
	$\chi_{\min}$	χ_{avg}	$\chi_{\max}$	σ_χ
349 K	-0.09	0.252	1.470	0.437
398 K	-0.07	0.146	1.010	0.259
	χ (simulated, via eq. (46))[1]			
	$\chi_{\min}$	χ_{avg}	$\chi_{\max}$	σ_χ
349 K	0.431	0.496	0.553	0.039
398 K	0.379	0.434	0.481	0.033
	χ (simulated, via traditional Flory-Huggins model)[1]			
	$\chi_{\min}$	χ_{avg}	$\chi_{\max}$	σ_χ
349 K	1.583	1.734	1.854	0.089
398 K	1.389	1.518	1.619	0.074

[1]The simulation data are averaged across 10 independent calculations, using dielectric screening by a water-like solvent ($\epsilon = 78.4$) in force field methods.

There are several striking results from this simulation. First, the method presented here quantitatively matches the data obtained via experimentation to a very satisfactory degree, with the average χ-value from simulation falling well within the range of values obtained from IGC for this polymer blend system at both 349 K and 398 K, the temperatures considered in Al-Saigh and Munk's work[181-182]. Moreover, the spread of the data obtained from this new computational methodology is far smaller than the spread in the experimental χ-values. Indeed, the computational methodology shown here reduces the standard deviation of the obtained data to only 10% of the data obtained via IGC experiments. It is also noteworthy that the results from the modified formulation of Flory-Huggins are much closer to experiment than those from traditional methods.

Finally, the results here were refined essentially as little as possible: only the monomers were considered, and the number of energy samples used did not exceed 1×10^6. By improving some of these simulation conditions, the accuracy and consistency of this miscibility analysis could be improved far beyond what can be extracted from physical experiments.

It is noteworthy that Knopp et al. have suggested that modeling the entire polymer is unnecessary to obtain reliable miscibility data. Instead, their work suggests that there is a threshold number of repeat units beyond which further increases in the degree of polymerization result in diminishingly small changes in the χ-value[185]. This suggests that appreciably accurate results can be obtained from relatively small molecules in a well-established simulation procedure.

Miscibility simulations were also performed for a blend of PEG (Figure 3) and PMMA (Figure 3), a system which has been studied experimentally using SANS[189]. Knopp et al. reported that using the monomer species to estimate polymer miscibility may be flawed in cases where the repeat unit chemistry is changed upon polymerization[185]. Thus, in order to more accurately capture the chemistry of PEG, the trimer form was used instead of the monomer, whereas only the monomer was considered for PMMA. The difference in degree of polymerization is normalized when calculating χ through the modified Flory-Huggins process introduced here; see equation (47). Figure 4 displays a comparison of the χ-parameter of this system obtained through SANS with that obtained from simulations.

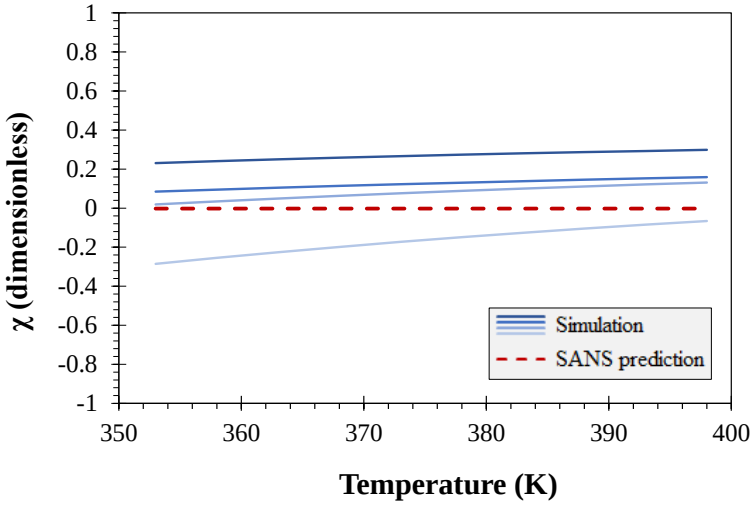

Figure 4. Change in χ-parameter as a function of temperature for the PEG-PMMA blend from both small-angle neutron scattering (dashed red line) and miscibility simulations (solid blue lines).

Notably, Ito, Russell, and Wignall found that the value of the χ-parameter for this system is very small – well under the θ-solvent condition of $\chi = 0.5$, indicating favorable miscibility[71, 189]. The modified Flory-Huggins simulation method yielded results in excellent quantitative agreement – across five independent trials, the average χ-value from simulation at all temperatures is only slightly larger than the value obtained from SANS. Qualitatively, it must be noted that the computational method resulted in a temperature-dependent χ-parameter in this range, which is not observed in SANS approaches. This result is not altogether unexpected, considering the aforementioned difficulties in addressing the temperature dependency of the χ-value in SANS experiments and the lack of explicit temperature dependence in equation (43).

Having verified the robustness and accuracy of this new methodology, the procedure was applied to an ABC triblock copolymer system consisting of poly(acrylic acid) (Figure 3), poly(6-(4-formylphenoxy) hexyl acrylate) (Figure 3), and poly(pentafluorostyrene) (Figure 3) as blocks A, B, and C, respectively. This system has been studied by the author for multicompartment micelle applications in collaboration with the Weck group at New York University. In this work, monomer, dimer, and trimer models were all studied so as to investigate the effect of the number of monomeric units on the calculation of χ-parameter.

Miscibility simulations were conducted on these molecules under a variety of conditions. First, simulations were performed on the monomer models, both with consideration given to dielectric screening effects (i.e., in the implicit presence of a water-like solvent with dielectric constant $\kappa = 78.4$) and without any dielectric screening. All simulations performed with dielectric screening used a dielectric constant of $\kappa = 78.4$, while those performed with no dielectric screening used $\kappa = 1$. Following this, the simulations were repeated for the dimer and trimer models with

dielectric screening to analyze the effect of number of monomeric units. These simulations were all performed multiple times, to examine the reproducibility of the present methodology.

Values of the χ-parameter as a function of temperature for each pair using monomer models with and without dielectric screening are shown in Figure 5, respectively. Flory-Huggins theory provides that χ = 0.5 corresponds to the θ-solvent condition[71]; thus, χ-values of less than 0.5 are known to be indicative of miscibility. Based on this, the simulation results for the monomer models in Figure 5 suggest full immiscibility in each pairing when dielectric screening is present, with pronounced immiscibility in the A-B and C-A blends.

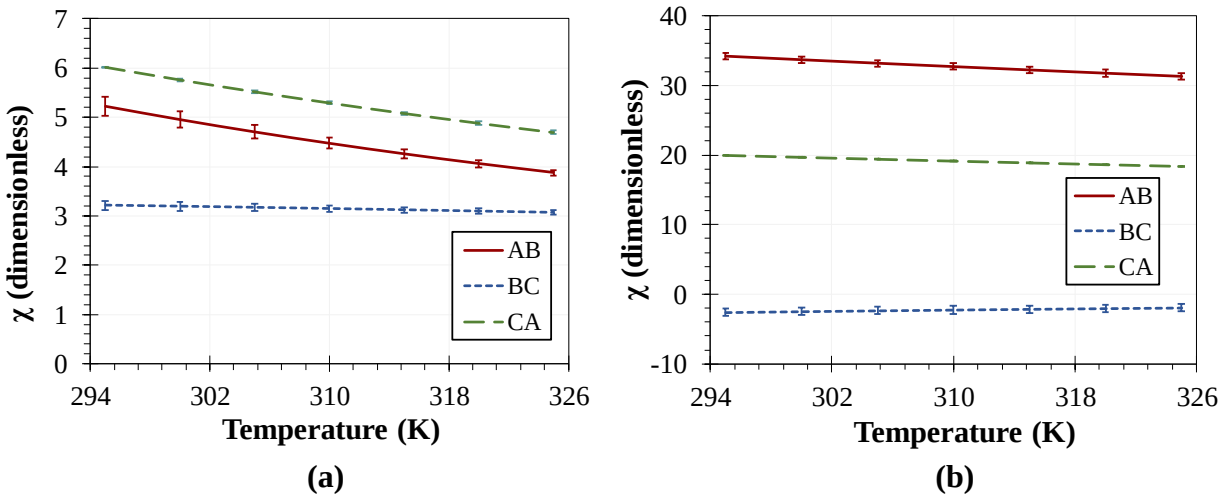

Figure 5. Change in χ-parameter as a function of temperature for each monomer model of triblock copolymer (Figure 3) (a) with dielectric screening and (b) without dielectric screening.

Here an important consideration arises with regards to force field conditions. In solution, while the hydrophilic A species will preferentially interact with water, the hydrophobic B and C species will be segregated from water, ultimately forming the core of the micelle. Because species A will be in contact with water, water-like dielectric screening (ϵ = 78.4) should be included for both the AB and the CA pairs.

However, there is no reason to believe that species B and C will be in contact with water in the equilibrium condition of the system (i.e., after micelle self-assembly). Thus, modeling the

B-C pair interaction with dielectric screening by a water-like solvent is an incorrect approach. Therefore, water-like dielectric screening ought to be omitted for the B-C interaction.

When these calculations are performed without dielectric screening, significantly different results are observed, as shown in Figure 5. Clearly, when the dielectric screening is removed, the B-C pair interaction becomes significantly more favorable. Indeed, the value of χ-parameter become negative in this region. Based on the difference between Figure 5, the importance of carefully selecting the dielectric constant should be quite clear. In the DPD simulations performed here, the AB and CA χ-values were obtained from simulations with dielectric screening and the BC values from simulations without dielectric screening.

These results suggest full phase separation between A and B, but only partial or no separation between B and C. As such, it would be expected that in a micellization experiment comprised of these blocks, there would only be two-compartment micelles formed. This was indeed confirmed via cryo-TEM by collaborators at New York University; the observed part of the micelle did not have internal phase segregation due to the miscibility of blocks B and C. This indicates remarkable success of the miscibility simulation and corresponding analysis presented here, especially since this was based on the monomers alone.

Moreover, it can be seen from Figure 5 that the χ-parameters calculated from molecular simulations are highly precise for the monomer model case. To illustrate this, Table 2 and Table 3 on the following page display simulation results used to calculate χ at 295 K both with and without dielectric screening, respectively. It is noteworthy that these are largely consistent between independent runs: miscibility calculations for each pair were performed ten times each and subsequently averaged in order to ensure repeatability of results.

Table 2. Parameters used to calculate χ at 295 K for the monomer case with dielectric screening.

	χ	Δw_{12}	$\frac{\Delta w_{12}}{V_{ref}}$	$\frac{E^*_{11}}{V_{11}}$	$\frac{E^*_{12}}{V_{12}}$	$\frac{E^*_{22}}{V_{22}}$	V_{11}	V_{12}	V_{22}	Z_{11}	Z_{12}	Z_{21}	Z_{22}
	-	$\frac{\text{kcal}}{\text{mol}}$	$\frac{\text{kcal}}{\text{mol}\cdot\text{Å}^3}$	$\frac{\text{kcal}}{\text{mol}\cdot\text{Å}^3}$	$\frac{\text{kcal}}{\text{mol}\cdot\text{Å}^3}$	$\frac{\text{kcal}}{\text{mol}\cdot\text{Å}^3}$	Å³	Å³	Å³	-	-	-	-
	5.24	3.07	0.0168	-0.0229	-0.0181	-0.0219	160.0	383.4	615.7	5.55	3.69	8.24	5.55
AB	5.03	2.95	0.0162	-0.0215	-0.0177	-0.0222	160.2	383.1	616.0	5.56	3.70	8.21	5.57
	5.41	3.17	0.0174	-0.0228	-0.0181	-0.0223	160.1	383.3	616.1	5.56	3.69	8.21	5.57
	3.10	1.82	0.0084	-0.0230	-0.0219	-0.0250	615.3	462.0	314.7	5.56	7.07	4.34	5.55
BC	3.24	1.90	0.0087	-0.0223	-0.0216	-0.0250	615.9	462.0	314.8	5.59	7.05	4.32	5.55
	3.29	1.93	0.0089	-0.0222	-0.0214	-0.0250	615.8	462.0	314.8	5.55	7.08	4.34	5.56
	6.01	3.52	0.0318	-0.0250	-0.0179	-0.0227	314.8	235.2	160.2	5.55	6.54	4.71	5.55
CA	6.00	3.52	0.0318	-0.0250	-0.0179	-0.0227	314.8	235.1	160.2	5.56	6.55	4.72	5.56
	6.03	3.53	0.0319	-0.0250	-0.0179	-0.0228	314.8	235.1	160.1	5.55	6.54	4.71	5.54

Table 3. Parameters used to calculate χ at 295 K for the monomer case without dielectric screening.

	χ	Δw_{12}	$\frac{\Delta w_{12}}{V_{ref}}$	$\frac{E^*_{11}}{V_{11}}$	$\frac{E^*_{12}}{V_{12}}$	$\frac{E^*_{22}}{V_{22}}$	V_{11}	V_{12}	V_{22}	Z_{11}	Z_{12}	Z_{21}	Z_{22}
	-	$\frac{\text{kcal}}{\text{mol}}$	$\frac{\text{kcal}}{\text{mol}\cdot\text{Å}^3}$	$\frac{\text{kcal}}{\text{mol}\cdot\text{Å}^3}$	$\frac{\text{kcal}}{\text{mol}\cdot\text{Å}^3}$	$\frac{\text{kcal}}{\text{mol}\cdot\text{Å}^3}$	Å³	Å³	Å³	-	-	-	-
	34.38	20.14	0.1108	-0.0811	-0.0322	-0.0283	157.2	378.5	613.1	5.54	3.68	8.27	5.55
AB	34.50	20.21	0.1112	-0.0817	-0.0318	-0.0270	157.3	378.4	612.9	5.53	3.67	8.26	5.57
	33.72	19.76	0.1087	-0.0810	-0.0317	-0.0264	157.3	378.6	613.2	5.54	3.68	8.26	5.59
	-2.44	-1.43	-0.0066	-0.0268	-0.0246	-0.0214	612.9	457.2	310.6	5.56	7.10	4.31	5.55
BC	-3.24	-1.90	-0.0087	-0.0261	-0.0247	-0.0215	612.8	457.2	310.6	5.57	7.12	4.30	5.56
	-2.16	-1.27	-0.0058	-0.0272	-0.0248	-0.0214	613.0	457.5	310.6	5.59	7.12	4.29	5.56
	20.05	11.74	0.1062	-0.0215	-0.0316	-0.0811	310.5	232.2	157.5	5.57	6.56	4.72	5.55
CA	19.88	11.65	0.1053	-0.0214	-0.0317	-0.0811	310.6	232.2	157.2	5.56	6.56	4.72	5.54
	19.97	11.70	0.1058	-0.0215	-0.0316	-0.0811	310.5	232.3	157.3	5.55	6.56	4.71	5.54

In order to analyze the miscibility of the dimer models, additional geometry optimizations were performed prior to Blends simulation due to the larger conformational diversity of the dimer species in comparison to the monomers. The additional optimization was performed in Forcite with a convergence threshold of 1×10^{-8} hartree using a smart convergence algorithm consisting of steepest descent[214], adopted basis Newton-Raphson[215], and quasi-Newton techniques[216-219].

From the data displayed below in Figure 6, it should be evident that the dimers behave quite similarly to the monomers (as seen in Figure 5). Comparing Figure 5 and Figure **6**, both the

monomers and the dimers display χ-values of close magnitudes. It is clear that the B-C pair is miscible in the dimer case regardless of dielectric screening, in contrast to same pair in the monomer case. Comparing the cases without dielectric screening, as observed in Figure 5 and Figure **6**, it is clear that the dimer and monomer models show similar miscibility behavior, although the dimer model results demonstrate slightly more immiscibility for the A-B pair than the monomer model results.

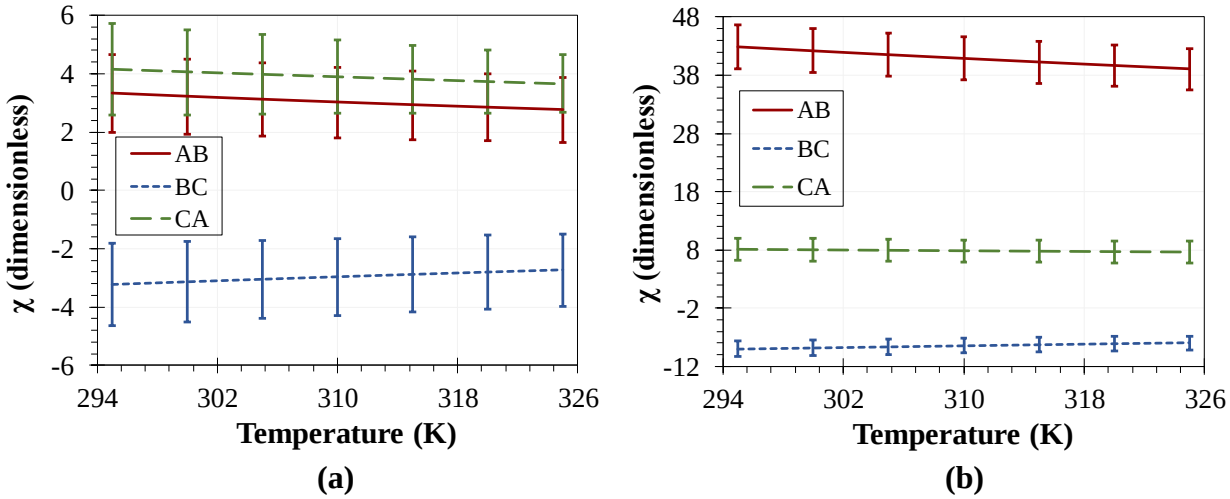

Figure 6. Change in χ-parameter as a function of temperature for each dimer model of triblock copolymer (Figure 3) (a) with dielectric screening and (b) without dielectric screening.

Overall, the relative miscibility behavior is in excellent agreement with the monomer results in each case – with dielectric screening present, as in Figure 5 and Figure **6**, the C-A pair interaction is the least favorable, while the B-C pair interaction appears to be most favorable. On the contrary, the cases without dielectric screening (Figure 5 and Figure **6**) point to the A-B pair as the least miscible, while the B-C pair is still the most miscible of the three.

For the trimer model, an additional geometry optimization was again performed prior to Blends simulations to combat the significantly higher conformational diversity of the trimer molecules; the settings of this additional optimization are identical to those in the dimer case. These simulations produced surprisingly precise results, especially considering the sizable

conformation space for each trimer. The variation of the χ-parameter with temperature for the trimer blends is shown in Figure 7.

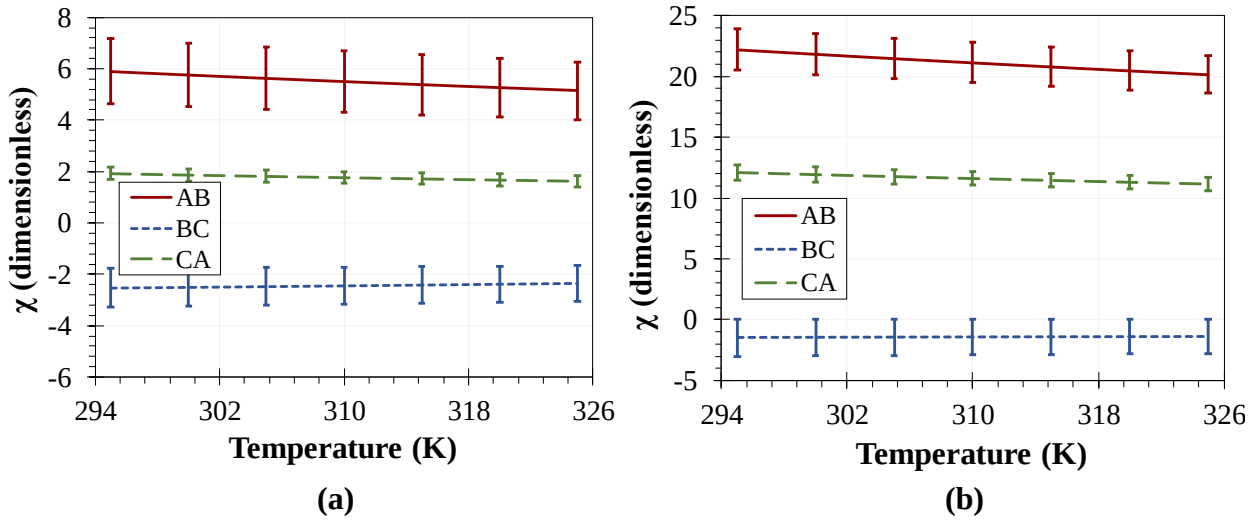

Figure 7. Change in χ-parameter as a function of temperature for each trimer model of triblock copolymer (Figure 3) (a) with dielectric screening and (b) without dielectric screening.

Figure 7 demonstrates that the B-C pair is highly miscible while the A-B and C-A pairs are immiscible. Again, these results are in good agreement with cryo-TEM results, confirming that the phase segregation between blocks B and C does not occur in the micelle, while the phase segregation between blocks A and B does indeed occur. The results from the trimer models are in agreement with those from the monomer and dimer models, although the relative ordering of the χ-parameters for the A-B and C-A pairs is reversed in the trimer model. It is likely that result can be attributed to the effect of conformational diversity, given that the results were normalized by the number of repeating units as well as Connolly volume, as discussed earlier. This appears probable due to the fact that the B-C pair interaction is unfavorable in the monomer model but becomes significantly more favorable in the dimer and trimer models.

Several points are evident in all of the studies performed on the miscibility of species A, B, and C. Principally, it is clear that the B-C pair is always the least immiscible, and in fact it is

predicted to be completely miscible in every study except that of monomers with dielectric screening, where the attractive interactions between these species are shielded by the dielectric medium (Figure 5). Additionally, the magnitude of the χ-parameter is in all cases significantly higher when dielectric screening is not present, which is of course to be expected.

These results suggest that while miscibility analysis does not require time-consuming explicit solvation modeling, it is essential to give careful consideration of the implicit solvent effects in order to correctly replicate the behavior of the polymer system. Overall, this investigation satisfactorily demonstrates that molecular modeling can provide an accurate and predictive method for phase separation of polymer-polymer systems, which should be a useful tool to design polymer architectures for multicompartment micelle-based nanoreactors.

To examine the application of our miscibility studies to micelle system, DPD simulations were performed on the ABC triblock copolymer system. As recalled from equation (33), the repulsion parameter of the DPD method can be connected directly to the χ-parameter through a simple linear scaling relation, the precise form of which is dependent on the bead density[169]. Results from these DPD simulations can be seen in Figure 8.

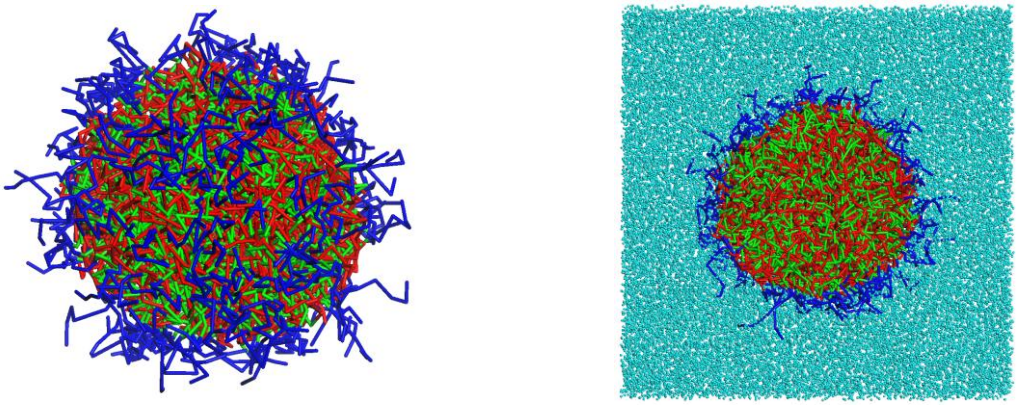

(a) (b)

Figure 8. DPD simulations results for micellization of triblock copolymer system in water (cyan). (a) Full micelle with water visibility disabled. (b) Cross-sectional view. Block A is phase-separated to form a shell (blue) while Blocks B (red) and C (green) have no phase-separation in the core.

Figure 8 displays complete microphase separation between the outermost A-block and the other two blocks, due to the favorable interaction between species A and water in the system (water beads omitted from Figure 8 for clarity). The cross-sectional view in Figure 8 shows that there is no microphase separation between blocks B and C within the core of the micelle. This is, of course, to be expected from the miscibility results obtained from the earlier χ-parameter analysis.

As noted previously, cryo-TEM work performed on micelles of the same system (with higher block lengths) show no visible microphase separation between the B and C blocks. Further development of the computational methodology introduced here is needed in order to achieve a higher level of correspondence between a real experimental system and its DPD representation. Nonetheless, these results underscore DPD as a viable avenue for studying the self-assembly of multiblock copolymers into micelles.

4. STRUCTURAL TUNABILITY OF LINEAR TRIBLOCK MICELLES

This chapter was adapted from a 2018 J. Phys. Chem. B *publication by the author*[66].

The self-assembled micelle structures formed by a triblock copolymer in solution can vary quite widely, even if the constituent species chosen are held constant. Other variables associated with the architecture of the copolymer may drastically affect the resultant structures. A trivial example lies in the difference between so-termed ABC and BAC micelles in water, where blocks A, B, and C are generally taken to represent hydrophilic, lipophilic, and fluorophilic (HLF) blocks, respectively; these systems have been observed to generate markedly different structures, even if the identities of species A, B, and C are identical[41-44, 60, 176, 220-221].

In particular, micelles formed by ABC triblock copolymers have been studied quite extensively[41, 60, 174-176]. These polymers readily form layered spheroids (referred to as "onion" morphologies[222-226]) composed of a fluorophilic core, an intermediate lipophilic layer, and a hydrophilic corona. Such morphologies are readily obtained from linear ABC triblock copolymers. If, however, the block sequence is modified to BAC, more exotic morphologies may easily be formed depending on the HLF block lengths.

Due to the complexity associated with the particular polymer architecture, then, a proper understanding of the dependence of micelle structure on the corresponding polymer architecture is essential in designing a multicompartment micelle (MCM) system. When considering such a study from a computational perspective, an important consideration arises straightaway: because micelle systems may contain tens of thousands of atoms, fully atomistic simulations prove to be impractical, if not outright inviable.

Coarse-graining techniques render many-atom systems more tractable to computational methods, but also carry the drawback of introducing varying degrees of abstraction to the system.

In order to simplify a system, groups of atoms or molecules are condensed into particles, which are then assigned properties that strive to capture the original chemical species that they represent. In DPD, these particles are referred to as *beads*[168-169] and may be assigned pairwise repulsion parameters to capture the values of their Flory-Huggins χ-parameters with other species[169].

Consequently, the degree of coarse-graining directly affects the correspondence with the physical system that the simulation model represents. It should be noted that for a given system, a decreasing extent of coarse-graining corresponds to increasing physicality. A comb-like polymer with bulky side-chains in a fully atomistic system would consider all bonded and non-bonded interactions, including electrostatic and van der Waals interactions[153, 193]; such a representation would be extremely computationally expensive.

Introducing coarse-graining by way of a method like DPD simplifies the representation of the system, reducing many-atom side chains to strings of beads whose characteristics attempt to capture the chemical identity of the original side chain. Even further coarse-graining reduces the side-chains into the backbone beads, yielding a purely linear polymer. While such a simplification is certainly insufficient for a complete understanding of a system, high-level coarse-graining presents an excellent preliminary method for studying the general effects of system variables. Moreover, it offers a versatile tool for determining the characteristics of the computational model which are most important in establishing correspondence with the real system.

In this DPD study, the effect of polymer architecture of an HLF triblock copolymer on the resultant aqueous MCM morphology are examined as a function of the sequence, length, and length ratio of the three polymer blocks. First, the structural differences ABC and BAC triblock copolymers are studied under the assumption that the molecule may be modeled as strictly linear rather than comb-like – i.e., with a high degree of coarse-graining. Following this, a more detailed

study of the BAC system highlights the dependence of the micelle structure on the lipophilic-to-fluorophilic block length ratio. In this study, this ratio is defined for a purely linear chain as

$$\mathcal{R}_l = \tilde{b}_L/\tilde{b}_F, \tag{50}$$

where $\tilde{b}_L$ and $\tilde{b}_F$ represent the reduced DPD block lengths corresponding to a real polymer of lipophilic and fluorophilic block lengths b_L and b_F. The variation in micelle structure as a function of $\mathcal{R}_l$ is studied at several fixed hydrophilic block lengths.

Based on the favorability of contributions from bulk interactions to the reduction of total energy, three morphological regimes are predicted to arise based on the $\mathcal{R}_l$-value of the constituent triblock copolymer. For $\mathcal{R}_l$-values either much greater than or much less than unity, it is expected that volume free energy contributions of the excess species will dominate and lead to the formation of spheroidal micelles comprised of a lipophilic (if $\mathcal{R}_l \gg 1$) or fluorophilic (if $\mathcal{R}_l \ll 1$) core covered by patches of the species with the lower $\tilde{b}$-value and finally a hydrophilic corona.

By contrast, for $\mathcal{R}_l$ near unity, it is predicted that a single-cored structure will be destabilized by the volume free energy contributions arising from the large amounts of both the lipophilic and the fluorophilic species. Instead, polymers with $\mathcal{R}_l$ near unity are expected to result in morphologies ranging from segmented worm-like structures to agglomerates of multiple cores (not to be equated with *multicore* micelles, which generally contain hydrophilic regions in between lipophilic and fluorophilic cores).

For the DPD simulations performed in this study, the system was defined as 5% polymer and 95% water – this is, of course, much larger polymer concentration than would be necessary in a real physical system; the larger polymer concentration is chosen in order to ensure a significant amount of polymer interactions. The simulation box size was defined to be 30x30x30 with grid spacing of 1.0 and a bead density of 3.0, allowing equation (33) to be applied[169].

Total simulation time was generally taken to be αt_e, where t_e is the minimum time required to achieve pressure equilibration. The constant α, chosen arbitrarily to be equal to 2.5, allows the simulation to continue for a fixed amount of time after initially reaching the equilibration stage, so as to ensure that the system has settled into a fully equilibrated state. For a time step of 0.05 reduced DPD unit, a total time of 8.75×10^3 reduced DPD units was determined to be satisfactory for all simulations. (The reduced DPD unit time is taken to be the amount of time necessary for a bead to diffuse a distance of its own radius due to thermal fluctuations[168-169].)

It should be noted that choosing a time step greater than 0.05 reduced unit is discouraged. As noted by Groot and Warren[169], employing a time step greater than this value results in artificial temperature increases in violation of equipartition. Indeed, selecting a time step of 0.1 reduced unit leads to increases in temperature on the order of 10%, certainly higher than is acceptable. The physical soundness of the DPD simulation can be gauged by examining the variation in system temperature and system pressure over the entire simulation time, as shown in Figure 9 on the following page.

Repulsion parameters for this study were assigned in order to ensure immiscibility between the A, B, and C blocks between both each other and water. The exact values were based first on χ-values calculated via the method introduced in Chapter 3, converted to repulsion parameters via equation (33), and finally adjusted in order to guarantee distinct three-phase separation upon self-assembly. Table 4 on the following page summarizes the values of these repulsion parameters.

To justify a more detailed study of the structural variation present in BAC micelle systems, a comparative look at both ABC and BAC micelle systems is warranted. As noted previously, it is expected that ABC micelles exhibit significantly less structural variation than the corresponding BAC micelles. Of course, this expectation is quite reasonable: the ABC block sequence aligns well

with the relative ordering of hydrophilicities between the three blocks. By contrast, the BAC block sequence requires alternate structures in order to minimize the free energy, since the traditional layered morphology will not always be possible.

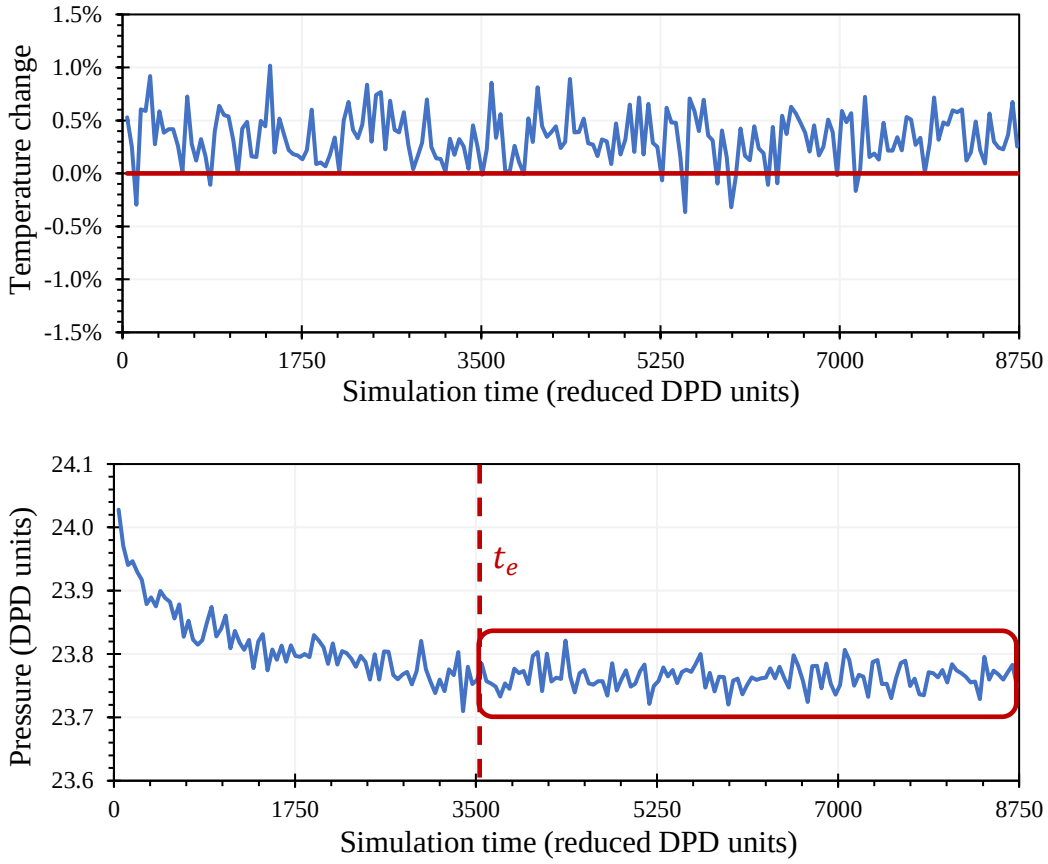

Figure 9. System temperature and pressure for a representative DPD simulation as a function of simulation time. The variation in temperature reveals an acceptably small average deviation from equipartition of approximately 0.3%, while the variation in pressure gives t_e = 3×10^3 reduced DPD units.

Table 4. Repulsion parameters a_{ij} between each pair of species in the DPD simulation system. Note that a_{ii} = 25.0 by definition[169] [see equation (33)]. Values in shaded cells are implied by other cells due to the fact that $a_{ij} = a_{ji}$.

	A	**B**	**C**	**W**
A	25.0	37.5	57.5	27.5
B	37.5	25.0	40.0	47.5
C	57.5	40.0	25.0	60.0
W	27.5	47.5	60.0	25.0

Indeed, simulation results bear out this prediction quite satisfactorily. Figure 10 displays the differences which arise between ABC and BAC micelle systems for $\mathcal{R}_l$ less than, equal to, and greater than unity (with the reduced hydrophilic block length held constant at $\tilde{b}_H$ = 15); water visibility is disabled in all figures for clarity. When the fluorophilic block length exceeds the

lipophilic block length (i.e., $\mathcal{R}_l$ is less than unity), the ABC and BAC systems form nearly identical structures. As the $\mathcal{R}_l$-value approaches unity, however, the BAC system diverges from a single-cored structure. In the limit as $\mathcal{R}$ becomes much greater than unity, the fluorophilic block becomes the deficient species, causing a significant structural change in the BAC system and a significant divergence between the two systems (Figure 10). The ABC system displays no structural changes as a result of modifying $\mathcal{R}_l$; an onion-like morphology is favored in each case. Increasing the $\mathcal{R}_l$-value in the ABC system corresponds only to generating a thicker lipophilic layer and a smaller fluorophilic core, while in the BAC system it causes a complete core inversion.

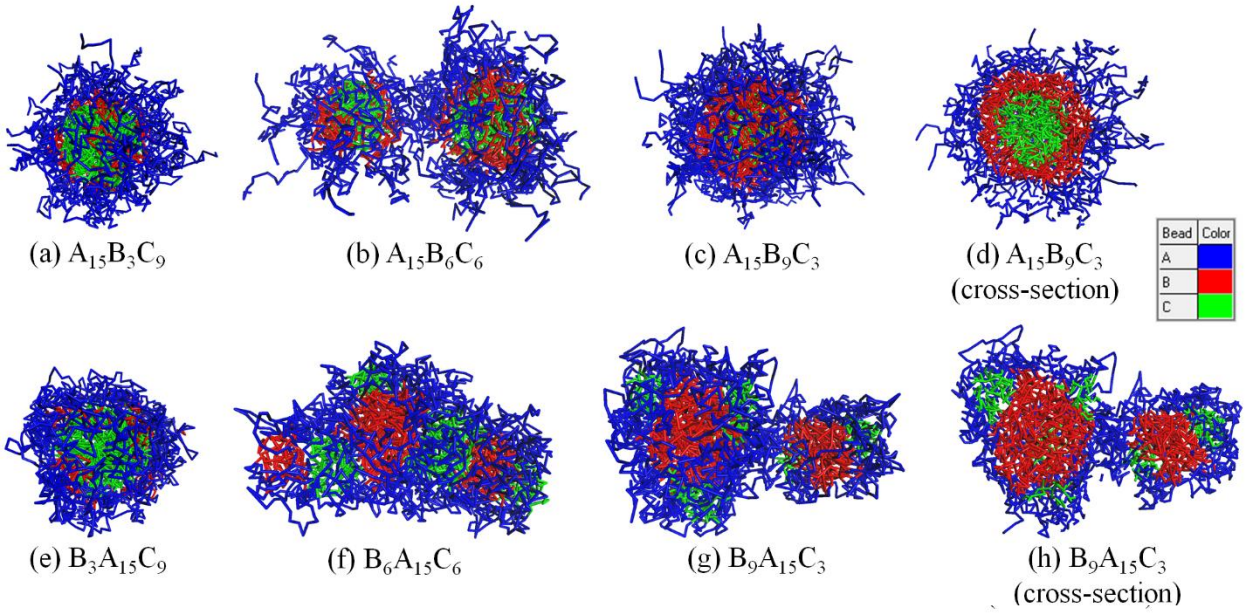

Figure 10. Morphological differences between (a-d) ABC and (e-h) BAC micelles as a function of $\mathcal{R}_l$ with $\tilde{b}_H$ = 15. As seen in the cross-sectional views in (d) and (h), the two systems result in markedly different morphologies for $\mathcal{R}_l$-values much greater than unity.

The difference between the two systems becomes quite pronounced in the limit of $\mathcal{R}_l \gg 1$. In fact, even when the hydrophilic block is shortened, ABC micelle systems still exhibit a dominant preference for fluorophilic-cored spheroidal micelles across all $\mathcal{R}_l$-values, as shown in Figure 11. BAC systems, by contrast, again display a complete inversion of the ABC morphology for large $\mathcal{R}_l$, forming micelles with fluorophilic patches surrounding a lipophilic core.

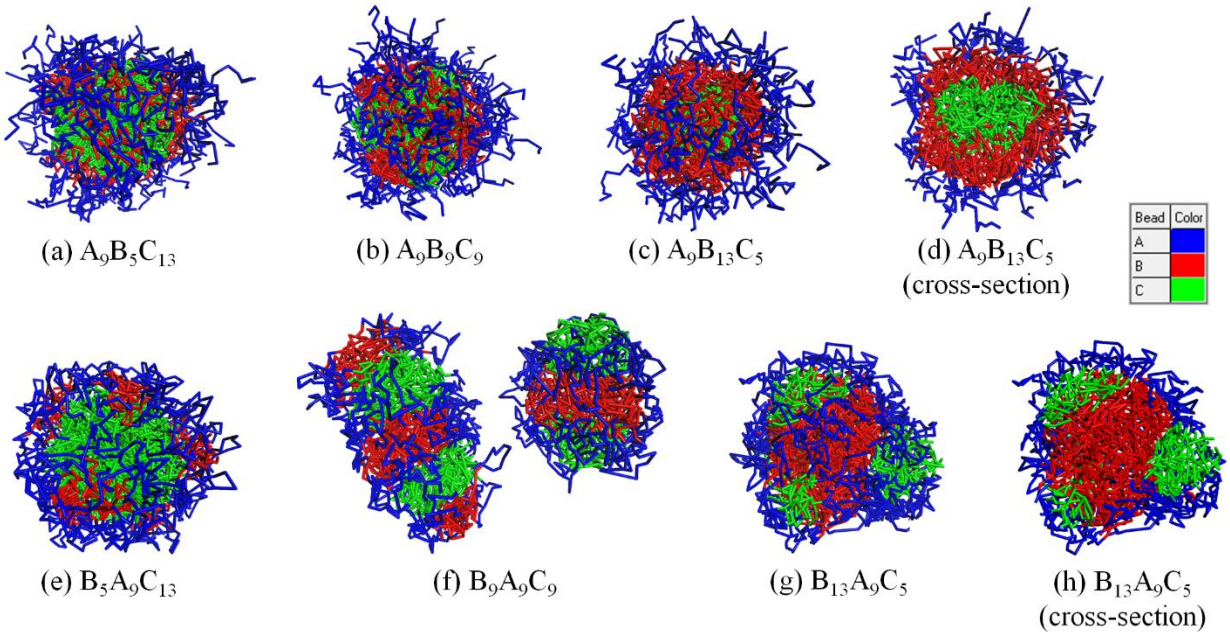

Figure 11. Morphological differences between (a-d) ABC and (e-h) BAC micelles as a function of $\mathcal{R}_l$ with $\tilde{b}_H$ = 9.

These results demonstrate that ABC micelle systems are relatively insensitive to changes in the $\mathcal{R}_l$-value, instead forming characteristically onion-like morphologies irrespective of this controlling parameter. When considering BAC systems, however, modifying the $\mathcal{R}_l$-value leads to a wider range of micelle morphologies. Indeed, as predicted previously, BAC systems exhibit three distinct structural regimes based upon $\mathcal{R}_l$. Considering the lipophilic and fluorophilic blocks as the two deciding species, when $\mathcal{R}_l$ strongly deviates from unity in either direction, there is a strong tendency to form spheroidal micelles with the deficient species forming into patches around a core composed of the excess species. For $\mathcal{R}_l$-values close to unity, neither species forms a dominant core and spheroidal morphologies are abandoned in favor of a more segmented structure. In all cases, the hydrophilic species forms an outer shell around the micelle – curiously, there does not appear to be a governing structural pattern in the modification of $\tilde{b}_H$.

Simulation results for a series of BAC micelle systems with a spectrum of $\mathcal{R}_l$-values are presented in Figure 12, where the horseshoe-like shape highlights the structural similarities at

either extreme of $\mathcal{R}_l$. For improved clarity, due to the thickness of the hydrophilic shell, visibility of the hydrophilic block is disabled in Figure 12. Note that the reduced hydrophilic block length $\tilde{b}_H$ = 18 for all simulations in Figure 12.

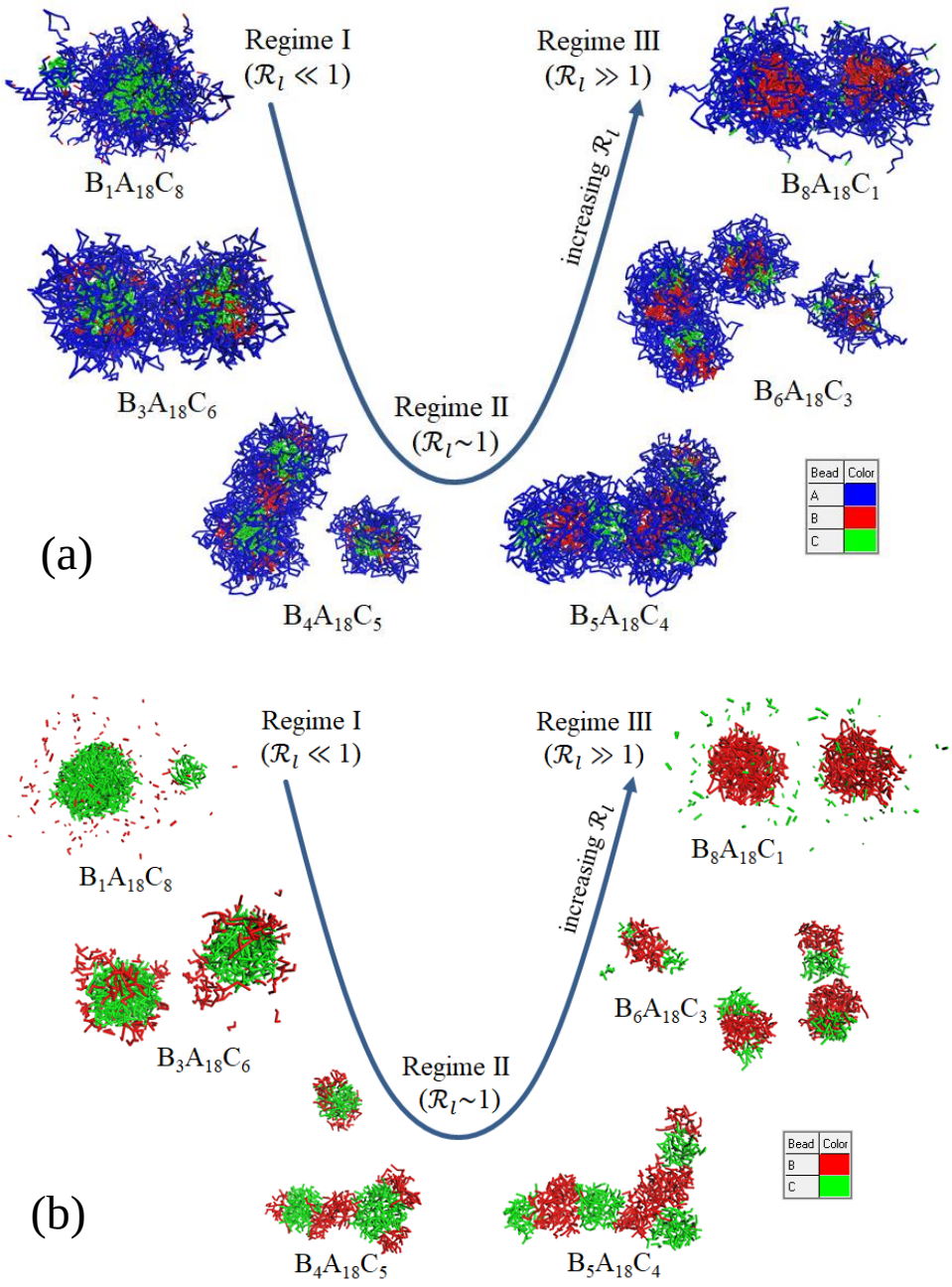

Figure 12. (a) A horseshoe diagram demonstrating the structural variation of a hydrophilic-rich ($\tilde{b}_H$ = 18) BAC micelle as a function of $\mathcal{R}_l$. Regimes I and III display morphological similarities, highlighting the importance of $\mathcal{R}_l$ as a morphological parameter. (b) The same simulation results with hydrophilic-block visibility disabled.

It is clear that the preference for the formation of a strongly spheroidal morphology increases as $\mathcal{R}_l$ becomes further from unity. Patches of the deficient species surround the core in these extremes (namely, regimes I and III). As $\mathcal{R}_l$ approaches unity, however, these patches become larger; near $\mathcal{R}_l$ = 1, the micelle structure becomes decidedly non-spheroidal (regime II). It is clear that segmented worm-like morphologies arise for $B_4A_{18}C_5$ and $B_5A_{18}C_4$. This behavior is especially evident in Figure 12, where the hydrophilic block visibility is disabled.

The *total* polymer length (i.e., $\tilde{b}_H + \tilde{b}_L + \tilde{b}_F$) was constrained to 27 in all simulations performed in this study, so as to guarantee a maximum extended polymer length shorter than the simulation box size in all dimensions. As a result of this constraint, simulations with smaller $\tilde{b}_H$ may take on larger values of $\tilde{b}_L$ and $\tilde{b}_F$ and, as a consequence, have access to a wider range of $\mathcal{R}_l$-values. Based on Figure 12, then, it should be expected that BAC triblock copolymers with larger $\mathcal{R}_l$-values should have a stronger preference to form spheroidal structures upon self-assembly.

Indeed, results from simulations performed for $\tilde{b}_H$-values of 15, 12, and 9 clearly demonstrate increasingly spheroidal morphologies in the regime I and III limits (where $\mathcal{R}_l$ is far from unity), as seen in the horseshoe diagrams in Figure 13-Figure **15**, beginning on the following page. Micelles in the intermediate range between regimes I/III and II characteristically display patches of the deficient species (again, either lipophilic or fluorophilic) with the core comprised of the excess species. As an extension of the patches observed at intermediate $\mathcal{R}_l$, micelles in regime II display the predicted agglomerates composed of multiple similarly-sized cores of both lipophilic and fluorophilic species.

It bears noting that no predominant structural patterns arise as a result of the decrease in $\tilde{b}_H$. This value appears to correspond solely to the thickness of the hydrophilic shell which surrounds the micelle, rather than any direct morphological changes. Certainly there is no obvious

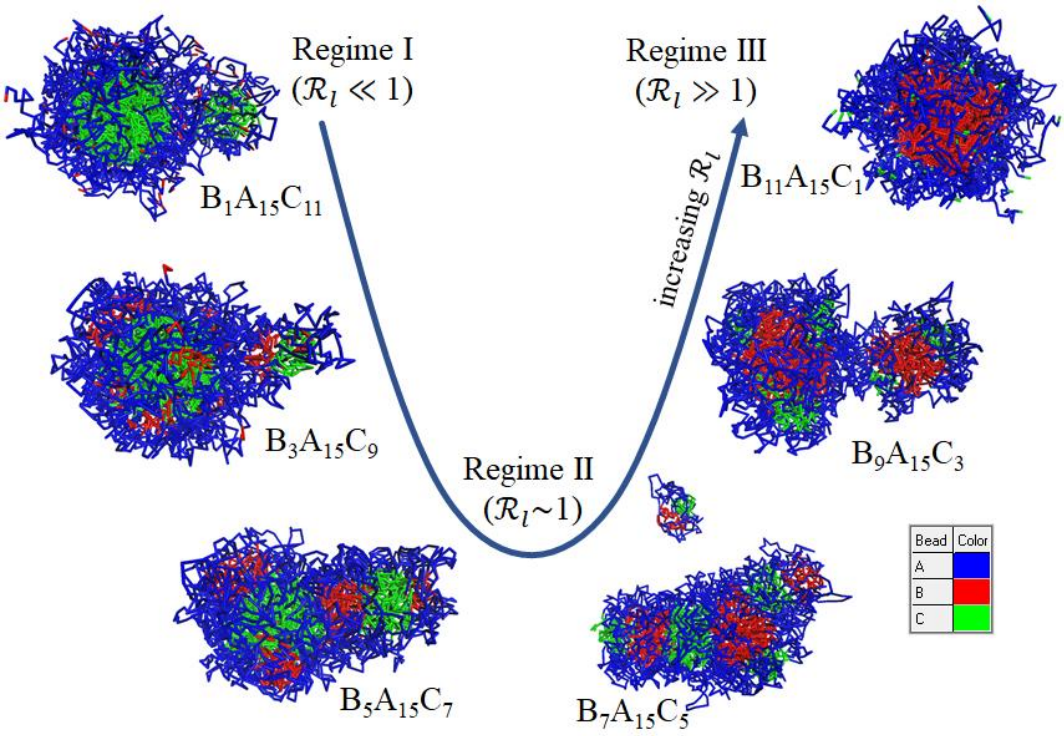

Figure 13. Structural variation of a BAC micelle with $\tilde{b}_H$ = 15 as a function of $\mathcal{R}_l$.

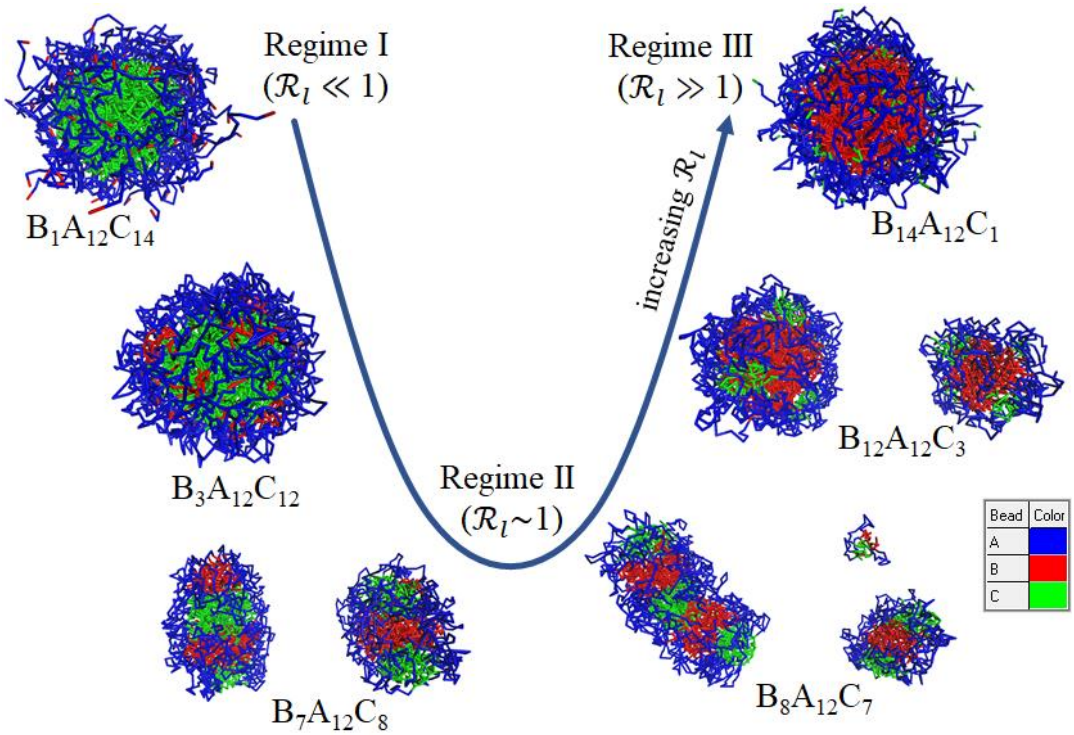

Figure 14. Structural variation of a BAC micelle with $\tilde{b}_H$ = 12 as a function of $\mathcal{R}_l$.

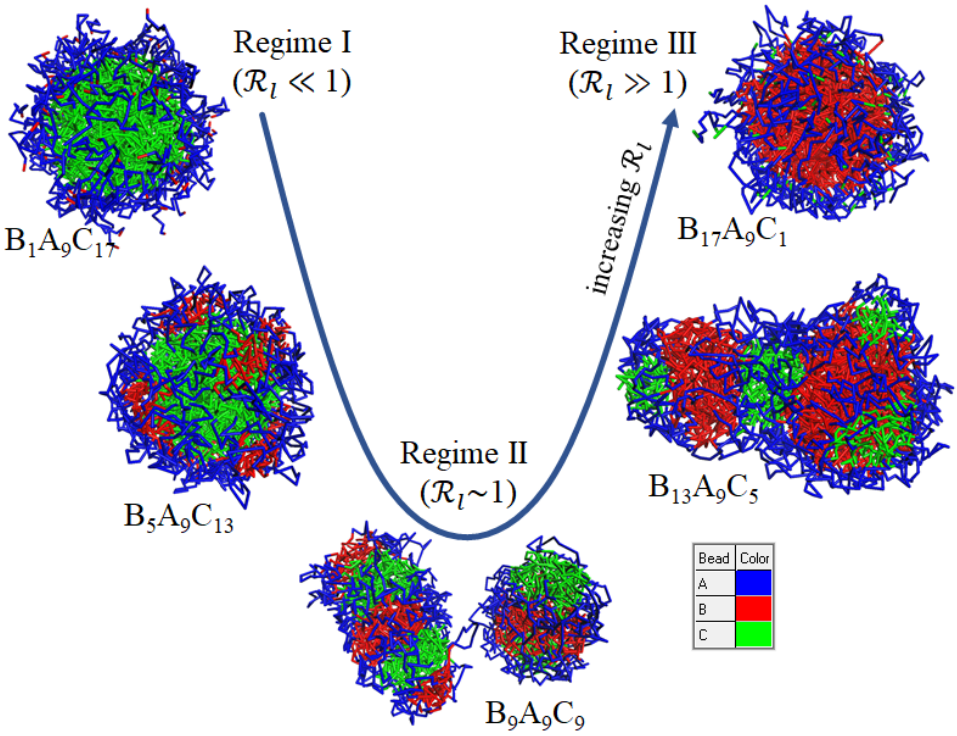

Figure 15. Structural variation of a relatively hydrophilic-poor ($\tilde{b}_H$ = 9) BAC micelle as a function of $\mathcal{R}_l$.

pattern in regimes I and III. Moreover, any trend in regime II appears to be exceedingly minor if present at all. In fact, this observation is not without precedent; Wang et al. reported results showing that further increasing $\tilde{b}_H$ beyond the point of full encapsulation of the micelle by the hydrophilic shell has the sole effect of increasing the shell thickness[227].

For systems of triblock copolymers with bulky side chains, intuition suggests that there exists a natural extension of the structural parameter $\mathcal{R}_l$ into a more general form $\mathcal{R}$ which does not require the aforementioned assumption of copolymer linearity. Precise determination of the quantitative relationship between block length, side-chain length, and micelle structure is the focus of the following chapter. Nonetheless, for systems where the assumption of copolymer linearity is applicable, the parameter $\mathcal{R}_l$ serves as an excellent predictive tool of micelle structure.

5. STRUCTURAL TUNABILITY OF BRANCHED TRIBLOCK MICELLES

This chapter was adapted from a 2019 J. Phys. Chem. B *publication by the author*[67].

As discussed previously, the spectrum of morphologies achievable through modification of the polymer architecture has been well documented to date[41-44, 60, 66, 176, 220-221]. Although micelles consisting of polymers with a hydrophilic-lipophilic-fluorophilic (often termed "ABC") block sequence typically result in layered onion-like spheroids[41, 60, 66, 176, 222-226, 228-229], a wider variety of morphologies have been observed when the copolymer block sequence is modified to lipophilic-hydrophilic-fluorophilic ("BAC")[43, 66, 227]. In Chapter 4, it was demonstrated that purely linear (i.e., without side chains) triblock copolymers with BAC block sequence result in morphologies that can be effectively tuned by modifying the lipophilic-fluorophilic block length ratio ($\mathcal{R}_l$)[66]. Because of the ease with which the block lengths may be modified during copolymer synthesis, the structural parameter $\mathcal{R}_l$ provides a direct avenue for the MCM morphology to be controlled in order to improve the catalytic performance of the MCM nanoreactor system.

However, despite the accuracy of the $\mathcal{R}_l$-parameter in predicting micelle morphology for triblock copolymer systems with (approximately) linear polymer architecture, its effectiveness is notably diminished for triblock copolymers which cannot be modeled as linear, including species with bulky side chains. This limitation can be problematic, since the principal consideration when selecting the constituent species of the triblock copolymer is the solvophilicity of each species.

It is natural, then, to seek a more generalized structural parameter $\mathcal{R}$ that does not require the assumption of linearity of the polymer architecture that limits the applicability of the $\mathcal{R}_l$-parameter. In this computational study, the dissipative particle dynamics (DPD) simulation method[166-169] is employed to study the variation in MCM morphologies as a function of the lipophilic-fluorophilic block length and side chain length ratios in order to explore the form of

such a generalized parameter. This study will also examine the extent to which the lipophilic and fluorophilic side chains have a similar effect on MCM morphology to that exhibited by the block lengths of these species. Finally, the relative importance of the polymer architecture will be discussed in comparison with the overall composition to remark upon the influence of linearity in deciding the final MCM morphology.

As defined in Chapter 4, the lipophilic-fluorophilic block length ratio is given by

$$\mathcal{R}_l = \tilde{b}_L/\tilde{b}_F, \tag{50a}$$

where $\tilde{b}_L$ and $\tilde{b}_F$ represent the reduced (i.e., coarse-grained) DPD block lengths corresponding to a real polymer of lipophilic and fluorophilic block lengths b_L and b_F, respectively[66]. It is worth noting that because the scaling factor should be very nearly identical for both the lipophilic and the fluorophilic blocks, the definition above may be alternatively written as

$$\mathcal{R}_l \approx b_L/b_F. \tag{50b}$$

In a BAC micelle system composed of purely linear triblock copolymers, this expression also captures the composition ratio between the lipophilic and the fluorophilic blocks; when bulky side chains are present, however, it is only one component of the composition ratio. To capture the effect of side chains, we introduce an analogous parameter $\mathcal{R}_s$:

$$\mathcal{R}_s = \tilde{s}_L/\tilde{s}_F \approx s_L/s_F, \tag{51}$$

where $\tilde{s}_L$ and $\tilde{s}_F$ represent the reduced side chain lengths within the lipophilic and fluorophilic blocks, respectively. We note that, depending on the nature of the species in these blocks in a real polymer, the "true" side chain lengths s_L and s_F may or may not retain physical meaning. In cases where the side chain cannot be modeled as a series of repeating units, we recommend the use of standard estimates of statistical side chain dimension[71] ($\langle R^2 \rangle^{1/2}$, R_g, etc.) in place of s_L and s_F.

Although the specific form of the generalized lipophilic-fluorophilic ratio parameter $\mathcal{R}$ will be discussed later in this work, at this point it is instructive to highlight two major requirements for this quantity. First, it is expected that, in the absence of side chains (or in systems that can be modeled with linear polymers), it simplifies to the linear form $\mathcal{R}_l$. Second, it is expected to serve as a reasonably good predictor of the micelle morphology based on the lipophilic and fluorophilic block and side chain lengths.

In order to determine the form of the $\mathcal{R}$-parameter, the simulation systems were set to have 5% polymer and 95% water. Although this polymer concentration is larger than would be used in a real physical system, a larger concentration is employed in our simulations in order to ensure more intensive polymer-polymer interactions and thus to better study the self-assembly process. The simulation box size was defined as 30×30×30 with a grid spacing of 1.0 and a bead density of 3.0, enabling the use of the linear relationship between the DPD repulsion parameter a_{ij} for species i and j and the corresponding Flory-Huggins χ_{ij}-parameter[169], as given in equation (33).

Ensuring the physicality of the DPD simulations and of the micelle self-assembly process requires monitoring the simulation pressure and temperature as a function of time. Total simulation time was chosen in all cases as αt_e, where t_e gives the minimum time required to achieve pressure equilibration (i.e., no monotonic change in pressure over time). The constant α, chosen arbitrarily here to be equal to 2.5, allows the simulation to proceed for a fixed amount of time after the equilibration stage is achieved in order to ensure a fully equilibrated state in the system. Using a time step of 0.05 reduced DPD unit, a total simulation time of 8.75×10^3 reduced units provided equilibrated results for all simulations. Reduced DPD unit time is taken as the duration necessary for a bead to diffuse a distance of its own radius due to thermal fluctuations[168-169].

The χ-values for each pair of species used in this study were first calculated via the method introduced in Chapter 3. These χ-parameter values were then converted into repulsion parameters via equation (33) and slightly adjusted to improve distinct phase separation upon self-assembly; the repulsion parameters used in these DPD simulations therefore represent idealized values for model study. Table 5 summarizes the a_{ij}-values for each pair of species used in this simulation system.

Table 5. Repulsion parameters a_{ij} between each pair of species in the DPD simulation system. Note that a_{ii} = 25.0 by definition[169] [see equation (33)]. Values in shaded cells are implied by other cells due to the fact that $a_{ij} = a_{ji}$.

	A	**B**	**C**	**W**
A	25.0	40.0	45.0	27.5
B	40.0	25.0	40.0	47.5
C	45.0	40.0	25.0	60.0
W	27.5	47.5	60.0	25.0

Finally, in order to facilitate the communication of structural information for triblock copolymers, we here use a condensed notation such that $X_{\tilde{b}_i,\tilde{s}_i}$ represents a block of species i with block length $\tilde{b}_i$ and side chain length $\tilde{s}_X$. Figure 16 provides a visual representation of this notation for additional clarity. While branched triblock copolymers were indeed the focus of this study, simulations of several purely linear copolymers were also performed with compositions identical to select branched triblock copolymers. These linear copolymers were included in our study in order to probe the extent to which micelle morphology depends on polymer architecture. For all branched copolymers in this study, the total block length was constrained to $\tilde{b}_L + \tilde{b}_H + \tilde{b}_F = 30$, while the total side chain length was constrained to $\tilde{s}_L + \tilde{s}_H + \tilde{s}_F = 8$.

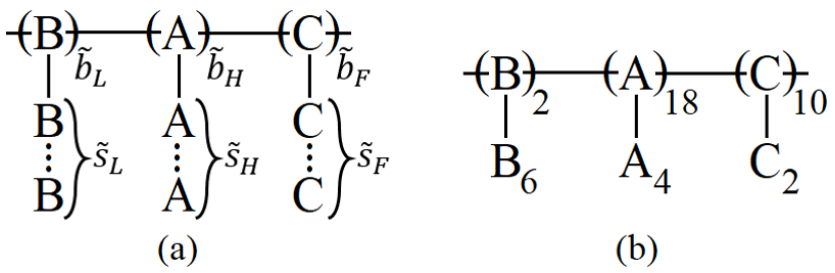

Figure 16. (a) A visual representation of the notation convention followed in this work, wherein $X_{\tilde{b}_i,\tilde{s}_i}$ represents a block of species i with reduced block and side chain lengths in DPD of $\tilde{b}_i$ and $\tilde{s}_i$, respectively. The triblock copolymer presented in (b) is thus represented as $B_{2,6}A_{18,4}C_{10,2}$.

In order to probe the full spectrum of morphologies as a function of polymer architecture, simulations were performed for five $\mathcal{R}_l$-values ($\mathcal{R}_l \ll 1$, $\mathcal{R}_l < 1$, $\mathcal{R}_l = 1$, $\mathcal{R}_l > 1$, and $\mathcal{R}_l \gg 1$). At each of these $\mathcal{R}_l$-values, five $\mathcal{R}_s$-values were tested (with a range similar to the $\mathcal{R}_l$-values), yielding a total of twenty-five architectures tested. It is important to note that, beyond a base length sufficient to ensure proper micelle coverage, the hydrophilic block length has been observed to have a minimal impact on the resultant morphology[66, 227]. The preliminary simulations indicated a similar trend in the impact of the hydrophilic side chain length. For these reasons, we here choose a constant hydrophilic block length of $\tilde{b}_H = 18$ and hydrophilic side chain of $\tilde{s}_H = 4$ in all cases.

At this point, we introduce the generalized form of the structural lipophilic-fluorophilic ratio parameter:

$$\mathcal{R} = \left[\tilde{b}_L(\tilde{s}_L + 1)\right]/\left[\tilde{b}_F(\tilde{s}_F + 1)\right] \approx \left[b_L(s_L + 1)\right]/\left[b_F(s_F + 1)\right] \qquad (52)$$

The reader may note that this form is essentially the composition ratio between the lipophilic and fluorophilic species. This form also simplifies to the simple $\mathcal{R}_l$-value given in equation (50a) in systems without side chains (i.e., when $\tilde{s}_i = 0$ for all species i), satisfying one of the major requirements set forth at the onset of this study.

As with the $\mathcal{R}_l$-parameter, the generalized $\mathcal{R}$-parameter enables predictions of micelle morphology based on the block lengths and side chain lengths of the lipophilic and fluorophilic

blocks. For systems where $\mathcal{R} \ll 1$ or $\mathcal{R} \gg 1$, the expected morphologies are quite similar: the micelles formed are spheroidal, largely preferring a single core composed of either the lipophilic or the fluorophilic species, whichever is in excess. The deficient species forms smaller patches surrounding the core, while the entire spheroid is covered with a layer of the hydrophilic species whose thickness is determined primarily by the hydrophilic block length. As established in Chapter 4, these morphologies represent regimes I (where $\mathcal{R} \ll 1$) and III ($\mathcal{R} \gg 1$). The intermediate regime II (where $\mathcal{R} \approx 1$) is characterized by notably less spheroidal morphologies containing multiple cores of both lipophilic and fluorophilic species.

5.1. Micelle Morphologies with $\mathcal{R}_l \ll 1$

The first set of simulations was performed with a lipophilic block length of $\tilde{b}_L = 2$ and a fluorophilic block length of $\tilde{b}_F = 10$, representing the $\mathcal{R}_l \ll 1$ extreme of the horseshoe diagram. These simulation results are presented in Figure 17, along with the corresponding polymer architectures and $\mathcal{R}$-values; water visibility is disabled in all figures for visual clarity. When $\mathcal{R} \ll 1$, as in the case of the $B_{2,2}A_{18,4}C_{10,6}$ micelle, the system preferentially forms a characteristically spheroidal regime I morphology with a fluorophilic core and many small lipophilic patches. However, as Figure 17 demonstrates, increasing the $\mathcal{R}_s$-value of the constituent polymers (and, by extension, increasing the $\mathcal{R}$-value) leads to the development of a smaller number of larger patches.

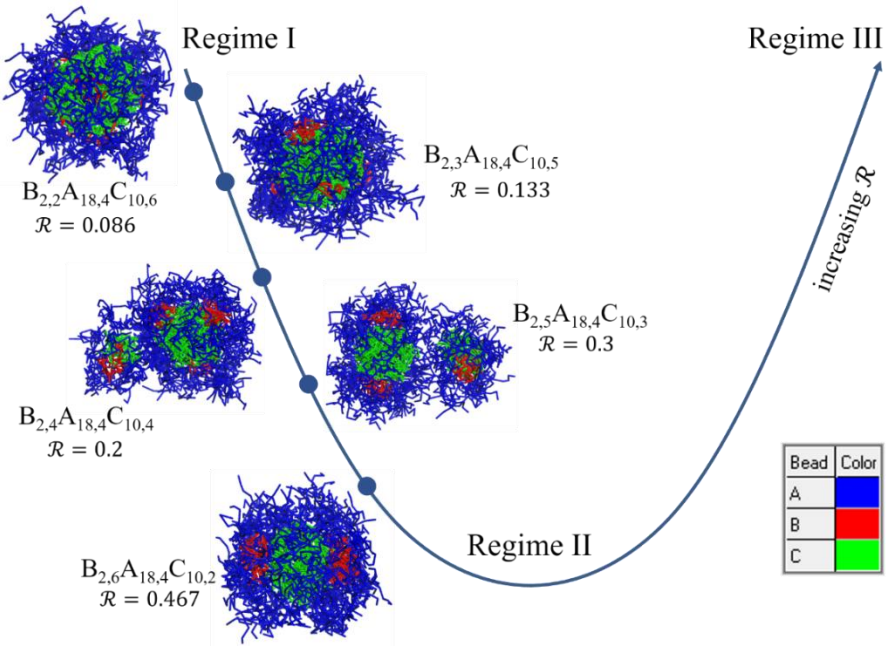

Figure 17. A horseshoe diagram demonstrating the structural variation of strongly fluorophilic-rich ($\mathcal{R}_l \ll 1$) BAC micelles as a function of the generalized structural predictor $\mathcal{R}$. Despite a constant $\mathcal{R}_l$-value in all cases, tunability from regime I to near regime II is observed, highlighting the importance of $\mathcal{R}$ as a governing structural parameter.

In particular, a clear morphological difference can be observed between the morphologies of the $B_{2,2}A_{18,4}C_{10,6}$ and the $B_{2,6}A_{18,4}C_{10,2}$ micelles: while the latter retains a fluorophilic core, it nonetheless displays a morphology intermediate in character to regimes I and II. These morphologies are well reflected by the difference in the corresponding $\mathcal{R}$-values ($\mathcal{R} = 0.086$ and $\mathcal{R} = 0.467$, respectively). The lack of morphologies in the regime II-III range is also explained by the range of $\mathcal{R}$-values surveyed, as $\mathcal{R} < 1$ for all architectures studied.

5.2. Micelle Morphologies with $\mathcal{R}_l < 1$

The second set of simulations was performed with $\tilde{b}_L = 4$ and $\tilde{b}_F = 8$, representing the $\mathcal{R}_l < 1$ region of the horseshoe diagram. Several features of these simulations are of note. As shown in Figure 18 on the following page, the first polymer architecture tested ($B_{4,2}A_{18,4}C_{8,6}$) results in a nearly identical morphology to that of the $B_{2,4}A_{18,4}C_{10,4}$ architecture in Figure 17, as predicted by their $\mathcal{R}$-values ($\mathcal{R} = 0.214$ and $\mathcal{R} = 0.2$, respectively). Since the regime II

morphologies dominate near $\mathcal{R} \approx 1$, it would be expected that the $B_{4,6}A_{18,4}C_{8,2}$ micelle ($\mathcal{R} = 1.167$) would disfavor a spheroidal single-cored morphology; indeed, Figure 18 confirms this, with this architecture instead forming a more segmented morphology.

5.3. Micelle Morphologies with $\mathcal{R}_l = 1$

Simulations in the $\mathcal{R}_l = 1$ region were performed with $\tilde{b}_L = \tilde{b}_F = 6$. For these simulations, the architectures tested span a range of $0.429 < \mathcal{R} < 2.333$, providing an effective representation of the tunability possible in BAC micelle systems. Although regimes I and III are not fully accessible based on the $\mathcal{R}_l$- and $\mathcal{R}_s$-values chosen, as Figure 19 on the following page demonstrates, the micelles at either end of the spectrum still display the characteristic similarity predicted based on their R-values: the $B_{6,2}A_{18,4}C_{6,6}$ and $B_{6,6}A_{18,4}C_{6,2}$ micelles both exhibit a spheroidal structure with the core composed of the species in excess and a small number of larger

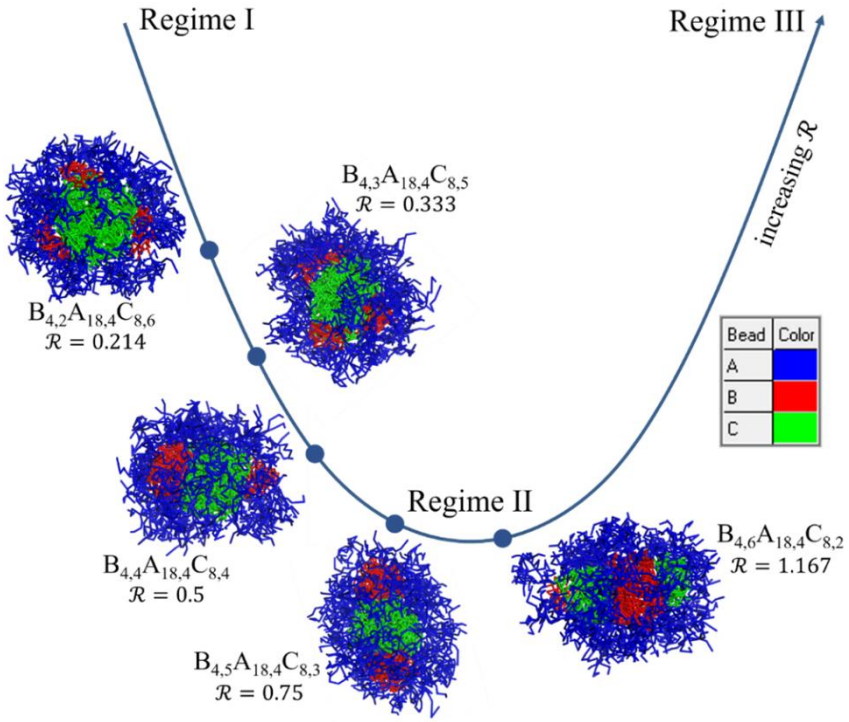

Figure 18. Structural variation of weakly fluorophilic-rich ($\mathcal{R}_l < 1$) BAC micelles as a function of the generalized structural predictor $\mathcal{R}$. Tunability between regimes I and II is observed.

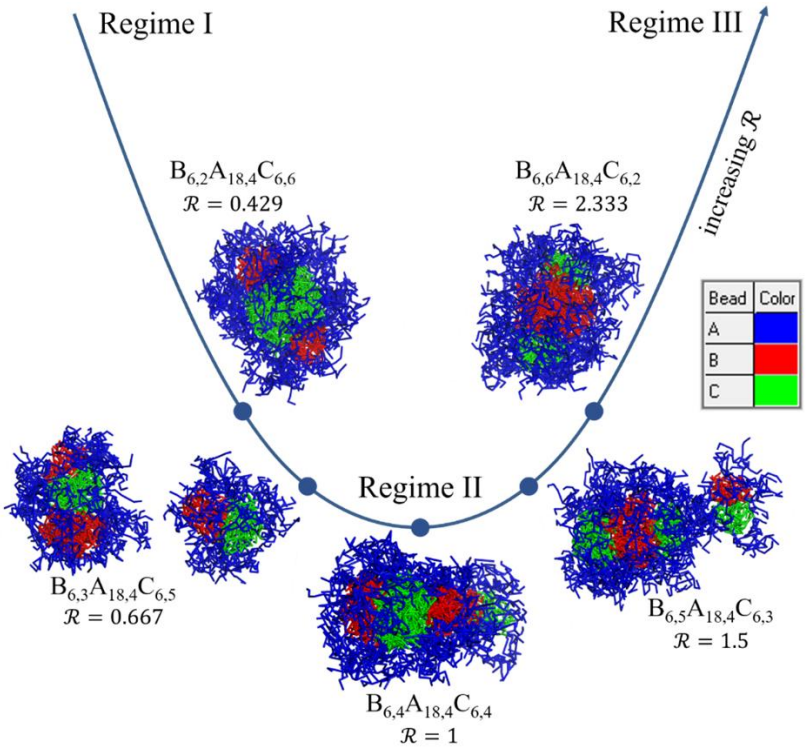

Figure 19. Structural variation of balanced ($\mathcal{R}_l = 1$) BAC micelles as a function of the generalized structural predictor $\mathcal{R}$. Slight tunability across all regimes is observed.

patches composed of the deficient species. Likewise, as the micelles' $\mathcal{R}$-values approach unity from either direction, the regions of the deficient species grow large enough to rival the regions of the dominant species, leading to a destabilization of the single-cored structure as expected.

5.4. Micelle Morphologies with $\mathcal{R}_l > 1$

The set of simulations performed with $\tilde{b}_L = 8$ and $\tilde{b}_F = 4$ represent the $\mathcal{R}_l > 1$ region of the horseshoe diagram, with the resultant morphologies shown in Figure 20. Notably, the horseshoe diagram associated with these simulations mirrors the diagram displayed in Figure 18. In particular, the $B_{8,6}A_{18,4}C_{4,2}$ architecture ($\mathcal{R} = 4.667$) forms a morphology that is essentially an inversion of the $B_{4,2}A_{18,4}C_{8,6}$ architecture ($\mathcal{R} = 4.667^{-1}$). Both the $B_{8,2}A_{18,4}C_{4,6}$ and the $B_{8,3}A_{18,4}C_{4,5}$ micelles form similar morphologies, as both polymer architectures display $\mathcal{R}$-values

near unity ($\mathcal{R} = 0.857$ and $\mathcal{R} = 1.333$, respectively). However, as the $\mathcal{R}_s$- and $\mathcal{R}$-values increase, the lipophilic core grows and the systems favor spheroidal morphologies in the regime III limit.

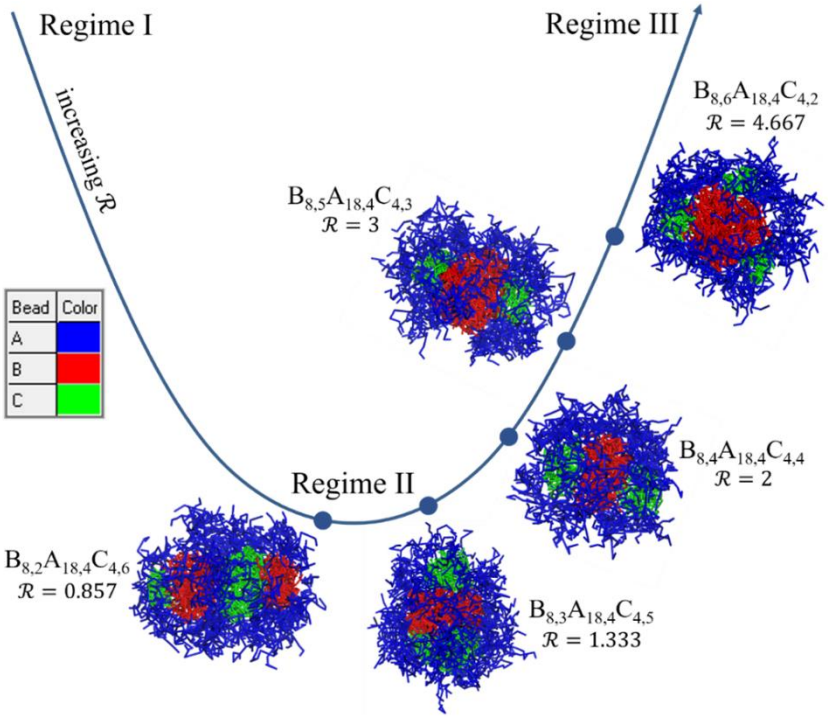

Figure 20. Structural variation of weakly lipophilic-rich ($\mathcal{R}_l > 1$) BAC micelles as a function of the generalized structural predictor $\mathcal{R}$. Tunability between regimes II and III is observed.

5.5. Micelle Morphologies with $\mathcal{R}_l \gg 1$

In a similar vein, Figure 21 displays the set of simulations which studies the $\mathcal{R}_l \gg 1$ extreme of the horseshoe diagram, with lipophilic and fluorophilic block lengths of $\tilde{b}_L = 10$ and $\tilde{b}_F = 2$, respectively. The spectrum of morphologies generated from these polymer architectures in turn mirrors the diagram shown in Figure 17. When $\mathcal{R} \gg 1$, as in the case of the $B_{10,6}A_{18,4}C_{2,2}$ micelle, the system exhibits the characteristic regime III morphology with a single lipophilic core and several smaller fluorophilic patches. This morphology is, in essence, an inversion of the $B_{2,2}A_{18,4}C_{10,6}$ micelle in Figure 17, as expected from the $\mathcal{R}$-values of each micelle ($\mathcal{R} = 11.667$ and $\mathcal{R} = 11.667^{-1}$, respectively). As the $\mathcal{R}$-value is decreased toward unity, the fluorophilic patches grow in size and approach the non-spheroidal morphologies found in regime

II; however, regime I remains fully inaccessible for the given micelles because $\mathcal{R} > 1$ for all copolymer architectures.

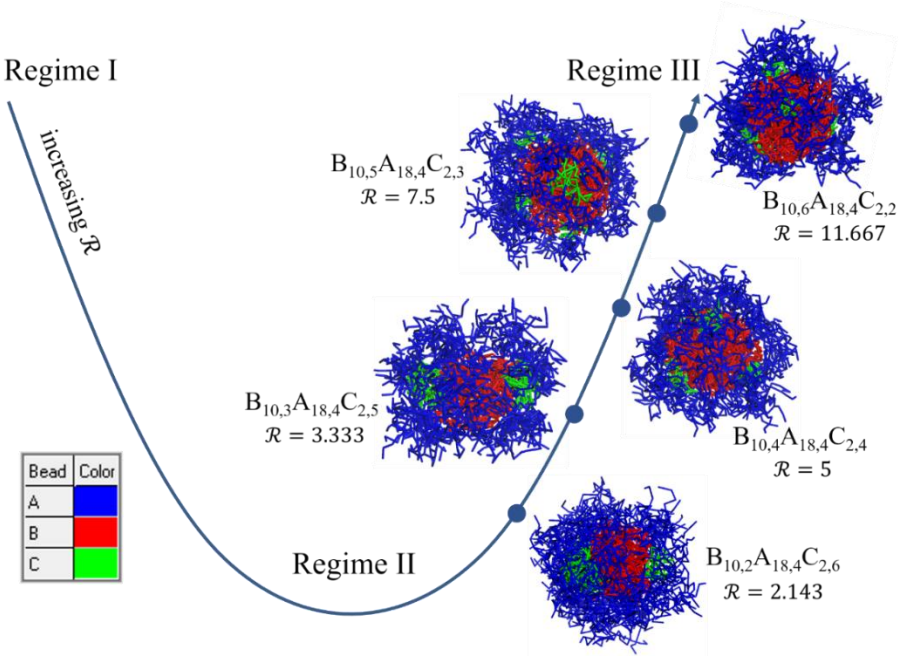

Figure 21. Structural variation of strongly lipophilic-rich ($\mathcal{R}_l \gg 1$) BAC micelles as a function of the generalized predictor $\mathcal{R}$. Tunability from near regime II to regime III is observed.

5.6. Comparison of Branched Architecture to Linear Architecture

Finally, in order to further study the effect of polymer architecture on micelle morphology in comparison to that of composition alone, simulations were performed with compositions identical to those studied previously, but with purely linear architectures instead of architectures with side chains. Figure 22 shows a side-by-side comparison between each branched architecture and the corresponding linear architecture with identical composition and $\mathcal{R}$-value. As can be seen from Figure 22, for $\mathcal{R}$-values of 0.086, 0.429, and 2.143, the linear and branched micelles display similar morphologies. However, in other cases, the linear architectures result in a markedly lower extent of patchiness in comparison with the branched architecture. We ascribe this result primarily to chain entanglement occurring in cases with much larger block lengths, as well as the difficulty

of forming small patches surrounding the core when the mean end-to-end distance of the polymer chains are larger than the characteristic patch size associated with the corresponding $\mathcal{R}$-value.

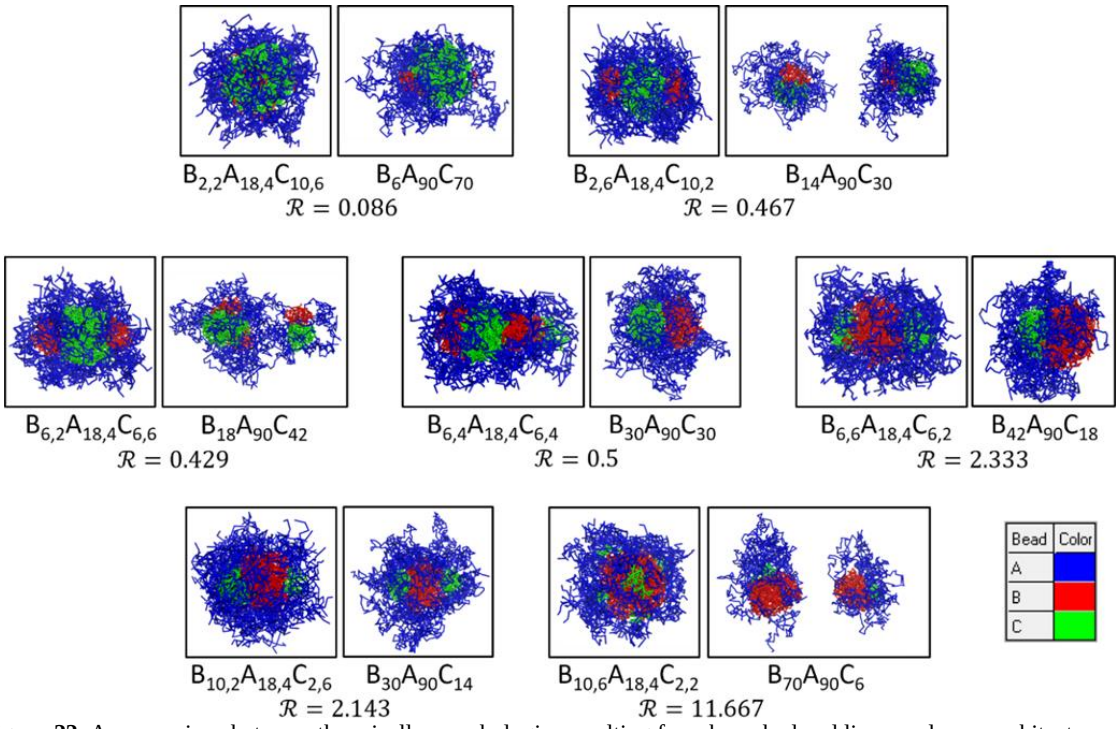

Figure 22. A comparison between the micelle morphologies resulting from branched and linear polymer architectures of identical $\mathcal{R}$-value.

The morphological differences observed between the branched and linear architectures are not necessarily detrimental; indeed, the range of morphologies generated between the branched and linear architectures for some $\mathcal{R}$-values establishes an additional layer of tunability even at constant $\mathcal{R}$. Because the patches surrounding the core represent distinct catalytic regions and can serve as entry points for reactants or exit points for products, it is useful to consider all avenues of structural tunability when designing a multicompartment micelle system for nanoreactor applications. These avenues may therefore include modification of the $\mathcal{R}_l$- or $\mathcal{R}_s$-values as well as extent of linearity in polymer architecture.

The morphologies formed by branched BAC triblock copolymers are highly consistent with those formed by linear BAC triblock copolymers in systems with short to intermediate block

lengths. For $\mathcal{R} \ll 1$ or $\mathcal{R} \gg 1$, copolymers preferentially form spheroidal morphologies with a single core composed of either the lipophilic or the fluorophilic species, whichever is in excess, while the deficient species forms patches surrounding the core. By contrast, for $\mathcal{R} \approx 1$, copolymers instead form non-spheroidal micelles with multiple "cores" of both lipophilic and fluorophilic species. In all cases, patchiness is noticeably decreased for copolymers with very long block lengths when compared to branched copolymers of the same composition and $\mathcal{R}$-value.

While this phenomenological study has provided quite satisfactory insights into the dependence of multicompartment BAC micelle morphologies on polymer architecture (and, by extension, the structural tunability of these systems), deeper mechanistic analysis is still required to understand the reason for the morphological trends observed in these systems. Moreover, a free-energy analysis may uncover heretofore unobserved morphologies of interest in immobilized catalysis applications. Through coarse-grained molecular mechanics calculations (e.g., approaches based on mean-field theory or free energy perturbation), the energetic contributions leading to the stability of patchy spheroids (regimes I and III) and multi-core agglomerates (regime II) may be identified. These contributions will provide essential insights into the morphological diversity of multicompartment BAC micelle systems, allowing for finer structural control than ever before.

6. STRUCTURAL TUNABILITY OF LINEAR TETRABLOCK MICELLES

The preceding chapters have highlighted the lipophilic-fluorophilic compositional ratio as a key structural parameter in the aforementioned BAC systems which allows for morphological predictions to be made on the basis of the polymer architecture alone. These studies demonstrated the effectiveness of this parameter in both linear[66] and branched[67] BAC triblock copolymer systems, allowing direct morphological control at the copolymer synthesis stage in order to optimize the catalytic performance of the resultant micelles.

Currently, studies may be found which demonstrate the feasibility of forming micelles from tetrablock copolymers[195, 230-234], but the full range of morphologies achievable in this system is not yet fully known. Although the $\mathcal{R}$-value was quite effective in triblock systems, this parameter in its previous formulations is inapplicable to micelle systems containing polymers comprised of more than three blocks. Since MCM structures offering wider morphological control in turn offer greater catalytic potential, it is therefore desirable to examine the self-assembly of tetrablock copolymers in order to identify morphological trends that can be harnessed for enhanced nanoreactor performance.

In this computational study, the dissipative particle dynamics (DPD) simulation method[166-169] is employed to study the variation in MCM morphologies as a function of both block sequence and relevant block length ratios in tetrablock copolymer micelles with four mutually immiscible blocks. Six different block sequences will be studied, in order to showcase a wide range of possible morphologies. As a result of these studies, a new form of the structural parameter $\mathcal{R}$ is presented which offers accurate predictions for these tetrablock systems and is robust with respect to block sequence. Finally, this study also highlights an auxiliary structural parameter $\mathcal{R}_a$ which does not arise in triblock systems and its importance in influencing the tunability of tetrablock micelles.

The block lengths of the lipophilic (B), fluorophilic (C), and superhydrophobic (D) species will be varied, while leaving the hydrophilic (A) block length unchanged in all simulations. As introduced in the preceding chapters, the notation $\tilde{b}_i$ will be used to denote the reduced (i.e., coarse-grained) block length of species i in DPD, corresponding to a polymer with block length b_i. The hydrophilic, lipophilic, fluorophilic, and superhydrophobic reduced block lengths are thus given as $\tilde{b}_H$, $\tilde{b}_L$, $\tilde{b}_F$, and $\tilde{b}_S$, respectively.

A generalized structural parameter, $\mathcal{R}$, was identified in Chapter 5 which serves as a predictor of micelle morphology in triblock copolymer systems of both linear and branched architectures[67]. This parameter is given by

$$\mathcal{R} = \left[\tilde{b}_L(\tilde{s}_L + 1)\right] / \left[\tilde{b}_F(\tilde{s}_F + 1)\right] \approx [b_L(s_L + 1)] / [b_F(s_F + 1)], \qquad (52)$$

where $\tilde{s}_i$ and s_i denote the reduced and true side chain lengths, the latter of which may be more accurately described by standard measurements of chain length[71] ($\langle R^2 \rangle^{1/2}$, R_g, etc.). The present study will focus on linear tetrablock copolymers for simplicity (i.e., $\tilde{s}_i = 0$ for all species i), though prior studies by the authors suggest that similar trends exist in triblock copolymers for both linear and branched architectures.

DPD simulation systems were performed with a composition of 5% polymer and 95% water. Although this polymer concentration is larger than would be used in a real physical system, a larger concentration is employed in our simulations in order to ensure more intensive polymer-polymer interactions and thus to better study the self-assembly process. The simulation box size was defined as 40×40×40 with a grid spacing of 1.0 and a bead density of 3.0, enabling the use of the linear relationship between the DPD repulsion parameter a_{ij} for species i and j and the corresponding Flory-Huggins χ_{ij}-parameter[169], as presented in equation (33).

The simulation pressure and temperature as a function of time to ensure that the DPD simulations and micelle self-assembly proceeded in a physically realistic way. Total simulation time was chosen in all cases as αt_e, where t_e gives the minimum time required to achieve pressure equilibration (i.e., no monotonic change in pressure over time). The constant α, chosen arbitrarily here to be equal to 1.5, allows the simulation to proceed for a fixed amount of time after the equilibration stage is achieved in order to ensure a fully equilibrated state in the system. Using a time step of 0.04 reduced DPD unit, a total simulation time of 1.0×10^4 reduced units provided equilibrated results for all simulations. Reduced DPD unit time is taken as the duration necessary for a bead to diffuse a distance of its own radius due to thermal fluctuations[168-169]. A time step less than 0.05 reduced unit was selected in order to avoid the artificial and unphysical increase in system temperature that may result from the use of larger time steps[169].

Table 6 summarizes the a_{ij}-values for each pair of species used in this simulation system. The repulsion parameters used in these DPD simulations therefore represent idealized values for model study. The specific repulsion parameter values between each pair of species in the system were determined based on those used in previous DPD studies by the authors[61, 66-67].

Table 6. Repulsion parameters a_{ij} between each pair of species in the DPD simulation system. Note that a_{ii} = 25.0 by definition[169] [see equation (33)]. Values in shaded cells are implied by other cells due to the fact that $a_{ij} = a_{ji}$.

	A	**B**	**C**	**D**	**W**
A	25.0	40.0	45.0	52.5	27.5
B	40.0	25.0	40.0	47.5	47.5
C	45.0	40.0	25.0	40.0	60.0
D	52.5	47.5	40.0	25.0	70.0
W	27.5	47.5	60.0	70.0	25.0

With four distinct species present in the tetrablock copolymers, there are clearly twelve *distinct* block sequences to choose from $({}_4\mathrm{P}_4/2)$. In this study, we will consider five values of $\tilde{b}_L$ for each block sequence and, further, a range of $\tilde{b}_F/\tilde{b}_S$ ratios for each lipophilic block length. The hydrophilic block length is held constant in all simulations, as previous literature suggests that its impact on the resultant morphologies is limited, provided that it is large enough to ensure micelle

formation[66-67, 227]. Since each simulation was performed several times with unique random number seeds (used in the DPD random thermal function[195]) in order to observe several different time evolutions of the same simulation conditions, the number of simulations and corresponding volume of results obtained would quickly grow quite difficult to display if all twelve block sequences were examined herein.

Consequently, we divide the twelve sequences into two groups, viz. those which contain the hydrophilic block as an "internal" (i.e., non-terminal) block and those which do not. Finding both groups to show considerable promise, this study concerns itself with the former for the reason that, in linear triblock copolymer micelles, the ABC block sequence has been observed to display lower morphological diversity than corresponding BAC polymers of equivalent block lengths[43, 66-67, 227]. To be specific, this work considers the BACD, BADC, BCAD, BDAC, CABD, and CBAD block sequences; the remainder will be considered in a separate study.

Nonetheless, the authors wish to note that the relatively lower tunability of ABC micelle morphologies compared to BAC micelles does not guarantee that such a trend would extend to tetrablock systems. In tetrablock systems with a terminal hydrophilic block, one might naturally wonder if the available permutations of the B, C, and D blocks alone may generate a wide range of possible morphologies, while still retaining the relative ease of achieving complete hydrophilic coverage present in ABC micelles. Thus, tetrablock copolymers with terminal hydrophilic blocks still warrant further study.

As discussed previously, the present work seeks to extend the $\mathcal{R}$-parameter to tetrablock systems. This is accomplished herein by modeling the structural parameter as a lever with the hydrophilic block as the fulcrum, as shown in Figure 23. As is also displayed in Figure 23, the proposed functional form of this structural parameter is given as

$$\mathcal{R} = \sum_{\text{Group 1}} \tilde{b}_{\text{i}} / \sum_{\text{Group 2}} \tilde{b}_{\text{j}} \approx \sum_{\text{Group 1}} b_{\text{i}} / \sum_{\text{Group 2}} b_{\text{j}}, \quad (53)$$

where the species on one side of the hydrophilic block are collectively referred to as "group 1" and those on the opposite side, if any are present, are referred to as "group 2". By convention, group 1 here will be taken to be the group containing the lipophilic species. Thus, in the block sequence BACD, only the lipophilic block is present in group 1, while group 2 contains both the fluorophilic block (C) and the superhydrophobic block (D); in the CABD block sequence, by contrast, group 1 contains blocks B and D, while group 2 contains block C. Using this flexible definition of the $\mathcal{R}$-parameter, we are nearly equipped to describe all architectures with one general parameter.

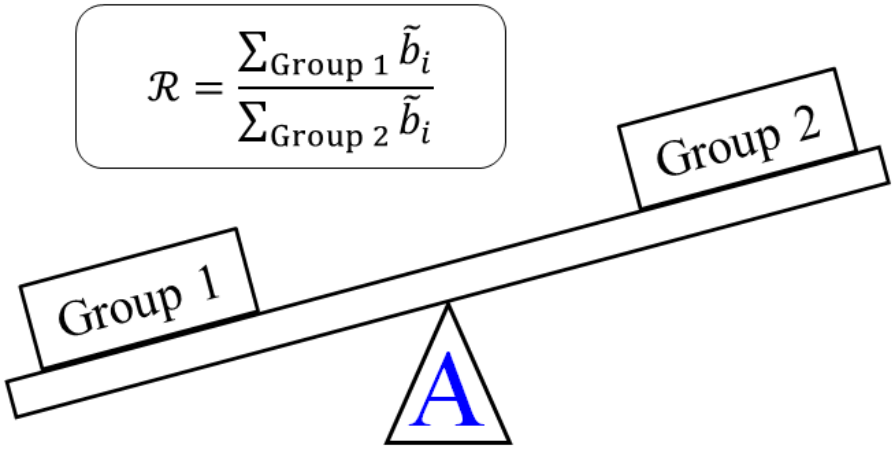

Figure 23. A diagram illustrating the proposed lever principle of the tetrablock micelle systems in this study. The hydrophilic block (A) behaves as a fulcrum, with the species on one side of the hydrophilic block ("group 1") on one end of the lever and the species on the other side of the hydrophilic block ("group 2") on the other end. By convention, here group 1 is taken to be the group containing the lipophilic block (B).

However, one additional parameter will prove useful in the course of discussing the morphologies which will be examined in this study. As there four blocks in each polymer, there is an additional vector of tunability in addition to the $\mathcal{R}$-value – namely, the block length ratio of the two species on the same side of the hydrophilic block. For convenience, we will use the nomenclature "terminal" and "internal" to refer to the two blocks in question, such that in the BCAD sequence, the lipophilic block is terminal and the fluorophilic block is internal. Thus, we introduce the parameter $\mathcal{R}_a$ to capture this auxiliary structural ratio:

$$\mathcal{R}_a = \tilde{b}_{\text{internal}}/\tilde{b}_{\text{external}} \approx b_{\text{internal}}/b_{\text{external}} \tag{54}$$

In the block sequence BACD, for example, $\mathcal{R}_a = \tilde{b}_F/\tilde{b}_S$, while in the block sequence CBAD, $\mathcal{R}_a = \tilde{b}_L/\tilde{b}_F$.

Although each block sequence will be discussed in detail later, a small collection of results of identical block length ratios but different block sequences is presented in Figure 24 on the following page in order to illustrate the range of morphologies predicted by the $\mathcal{R}$-value. The proposed form of the structural parameter for tetrablock systems offers the same general predictions of the $\mathcal{R}_l$- and $\mathcal{R}$-values of prior studies by the authors, as shown in Figure 24. Architectures that have an $\mathcal{R}$-value either much less than or much greater than unity strongly favor a spheroidal morphology, while those with an $\mathcal{R}$-value of approximately unity tend to form predominantly linear, segmented morphologies. Further morphological tunability in these systems is achieved by modifying the ratio of the species on the same side of the hydrophilic block.

One final comment regarding all six block sequence is warranted; while similar tunability is possible in all block sequences, some block sequences display less desirable hydrophilic coverage despite a constant hydrophilic block length in all simulations ($\tilde{b}_H = 18$), due to the difficulty of configuring the micelle with the hydrophilic species facing the solvent while simultaneously shielding other species from it. Thus, if the remaining six block sequences (with the terminal hydrophilic block) do not display the relatively lower tunability exhibited by many triblock copolymers with terminal hydrophilic blocks, they may offer more promising morphologies in some cases due to the greater ease of achieving hydrophilic coverage.

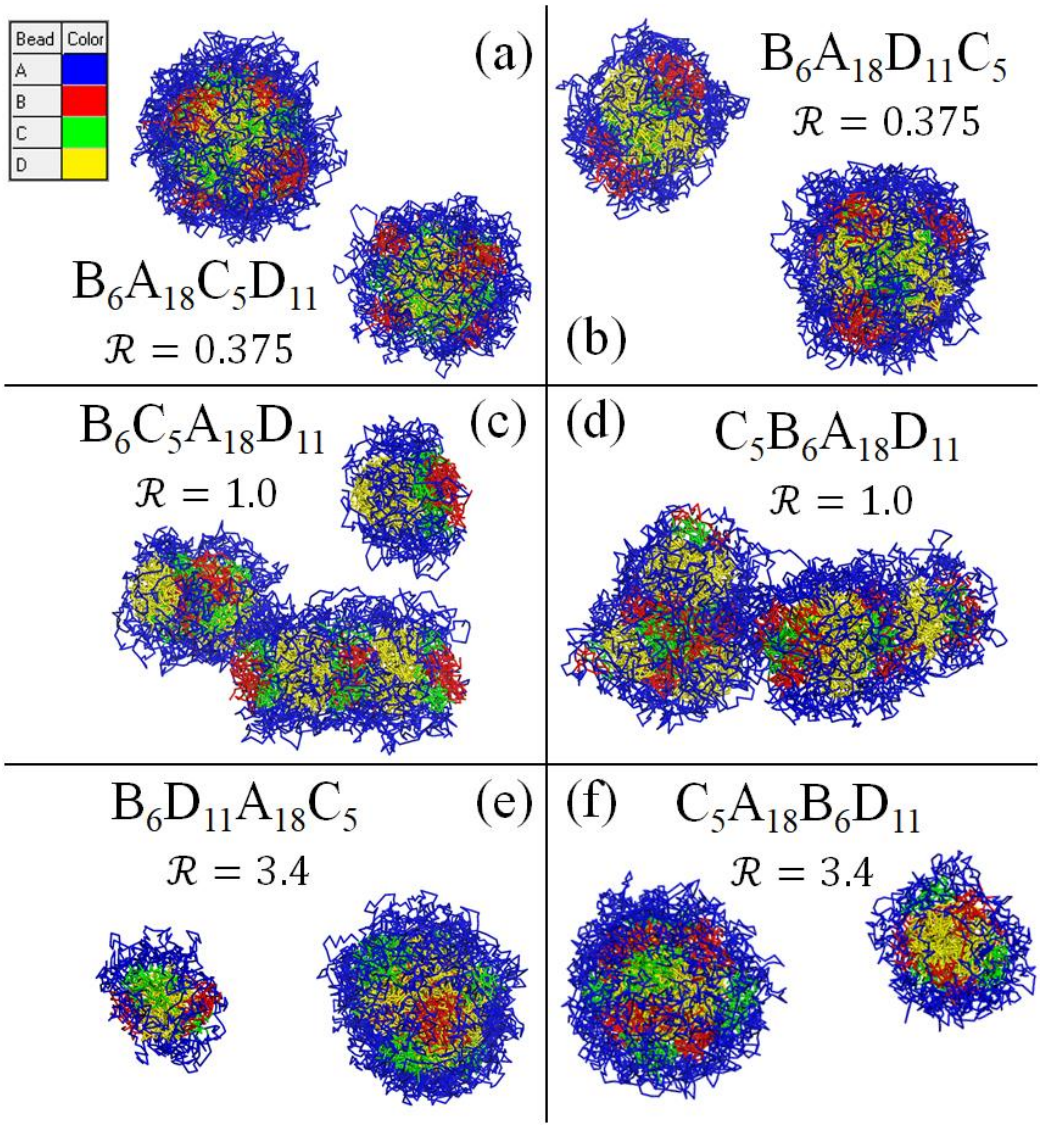

Figure 24. A demonstration of the proposed lever principle in tetrablock micelles using results from DPD simulations with identical block lengths, but six different block sequences.

The results of individual block sequences will be presented in pairs, such that both of the sequences in each pair have the same species in group 1 and in group 2. This style of presentation is chosen for two reasons. First, this allows the two sets of results to be compared directly, as their $\mathcal{R}$-values match exactly. Second, and more importantly, the morphologies formed by architectures in each pair (e.g., $B_8C_{12}A_{18}D_2$ and $C_{12}B_8A_{18}D_2$) are similar in many cases, with the reversal of the species on the side of the hydrophilic block that has two species being the chief difference. In all cases, the visibility of the water beads is disabled for visual clarity.

6.1. Polymer Architectures with Block Sequence BACD or BADC

The design of experiment used in this study led to a hierarchy of variables, with results grouped first by block sequence and second by lipophilic block length, with the plotted results showing a spectrum of morphologies based on the changing fluorophilic and superhydrophobic block lengths. For all architectures in this study, both the hydrophilic block length and the *total* chain length were held constant. Consequently, for both the BACD and BADC block sequences, all of the results with the same lipophilic block length yield identical $\mathcal{R}$-values. Figure 25 and Figure **26** on pages 73-74 show the results of the BACD and BADC block sequences, respectively, which highlight the connection between the $\mathcal{R}$-value and the resultant micelle morphology.

Overwhelmingly spheroidal morphologies were formed for $\tilde{b}_L = 6$ and for $\tilde{b}_L = 16$, in agreement with the predictions offered by the $\mathcal{R}$-values of each case (0.38 and 2.67, respectively). For $\tilde{b}_L = 6$, all BACD morphologies displayed layered cores composed of superhydrophobic species in the center with a surrounding layer of fluorophilic species, which were in turn surrounded by several patches of lipophilic species. As the value of $\mathcal{R}_a$ decreases, the superhydrophobic core increases in size, while the fluorophilic layer thins. BADC morphologies were quite similar, with the sole difference being that the layered cores were composed of fluorophilic species in the center with a surrounding layer of superhydrophobic species.

The morphologies with $\tilde{b}_L = 16$ displayed comparable behavior; in this case, all micelles exhibited a lipophilic core, with layered patches surrounding the overall micelle core. In BACD micelles, these layered patches were composed of superhydrophobic cores and fluorophilic coatings, while in BADC micelles, the two species were reversed. These morphologies are quite interesting in that they display a combination of features of ABC and BAC micelles, forming both layered "onion-like" morphologies often observed in ABC micelles and the patchy nanostructures

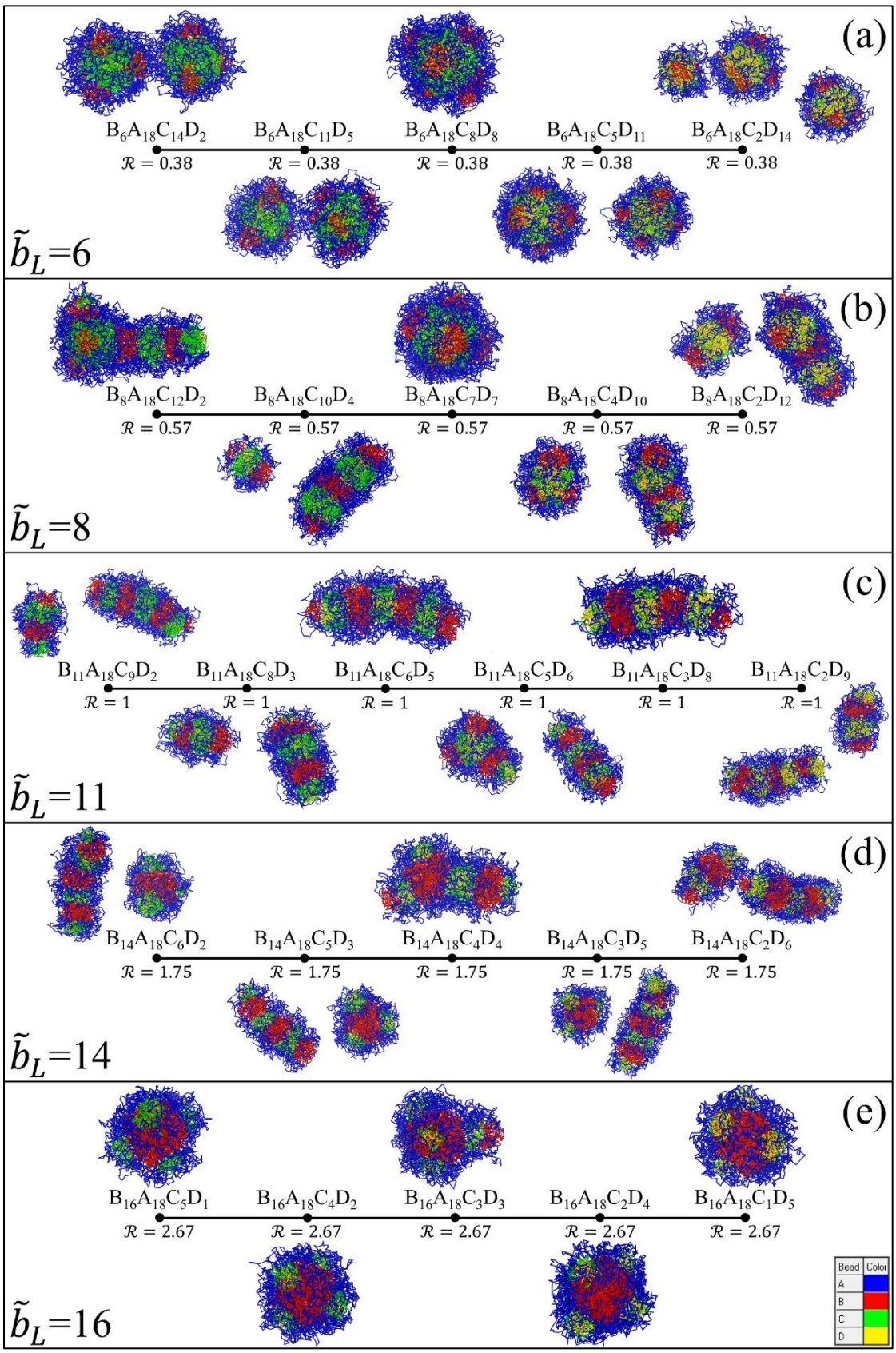

Figure 25. DPD results for tetrablock copolymers with the BACD block sequence, separated by lipophilic block (B) length.

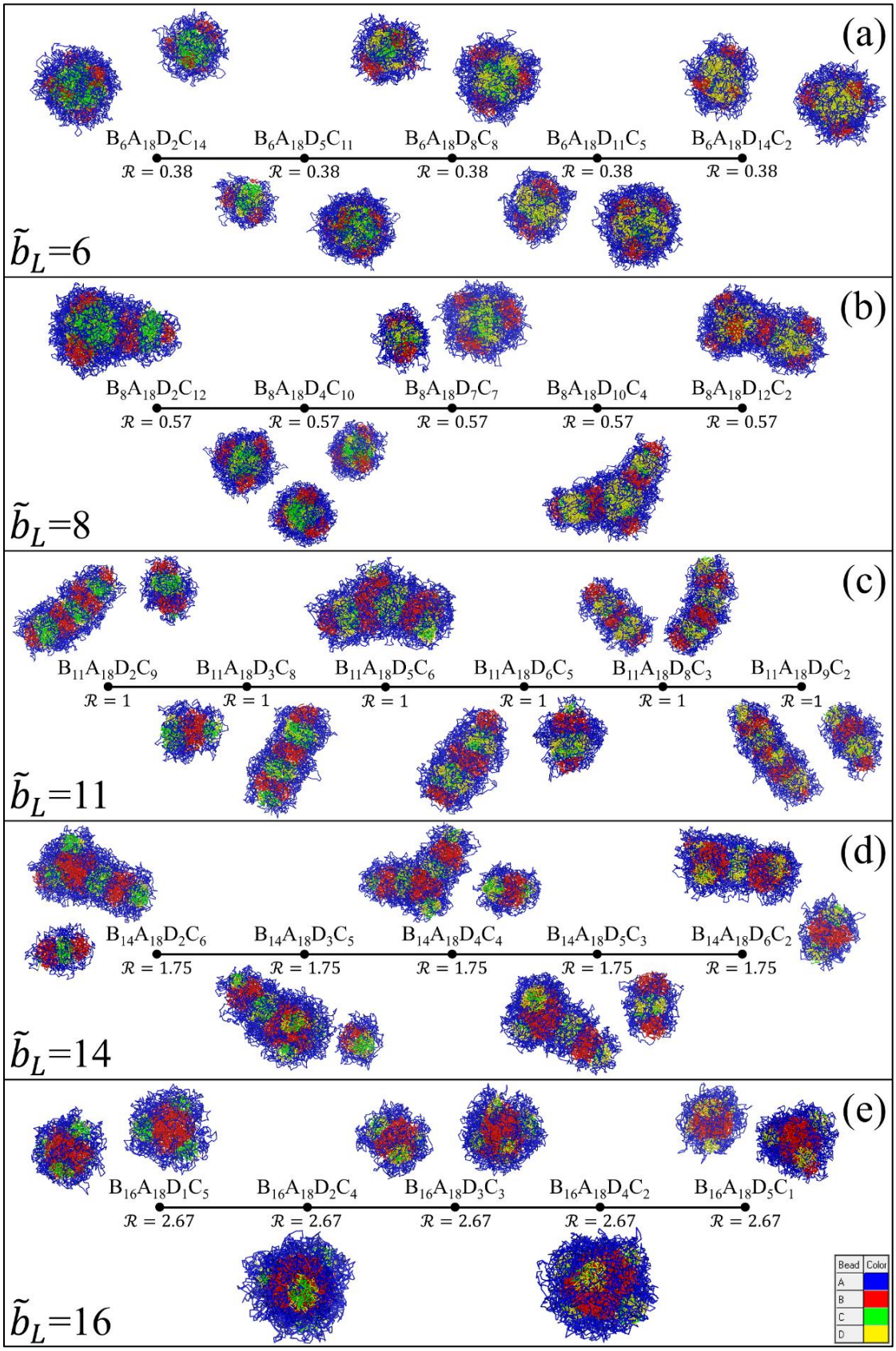

Figure 26. DPD results for tetrablock copolymers with the BADC block sequence, separated by lipophilic block (B) length.

more commonly seen in BAC morphologies[43-44, 66-67].

Architectures with $\tilde{b}_L = 8$ or $\tilde{b}_L = 14$ display a wider range of morphologies, owing to the intermediate $\mathcal{R}$-values (0.57 and 1.75, respectively). While most of the morphologies for $\tilde{b}_L = 8$ are pronounced in their linearity, the $B_8A_{18}C_7D_7$ architecture consistently formed spheroidal micelles. This exception is observed for both $B_8A_{18}D_4C_{10}$ and $B_8A_{18}D_7C_7$ as well, as seen in Figure 26, leading to the possibility that a secondary stabilizing effect is present in addition to the overall effect of the $\mathcal{R}$-value. Moreover, the presence of some spheroidal BACD micelles in the $\tilde{b}_L = 14$ group leads the authors to suggest that the $\mathcal{R}$-value of a particular architecture leads to a strong preference for a class of morphologies, rather than a strict adherence to this class.

Finally, the micelles with $\tilde{b}_L = 11$ displayed strongly linear, segmented morphologies, as predicted by the $\mathcal{R}$-value of exactly unity in this group. Here, neither lipophilic-cored micelles nor micelles with fluorophilic or superhydrophobic cores are stabilized enough to favor a spheroidal morphology, so alternating morphologies are favored. In this group we also observe the first example of a trend which will be seen to continue in other block sequences: in segmented morphologies, segments are formed of either all of the groups on one side of the lever or all of the groups on the other (e.g., alternating segments of B and C/D, in the case of these two sequences).

6.2. Polymer Architectures with Block Sequence BCAD or CBAD

The morphologies of architectures with BCAD and CBAD block sequences are shown in Figure 27 and Figure **28** on pages 76-77, respectively. These two block sequences exhibited very similar results, with the predominant difference being the reversal of the lipophilic and fluorophilic regions between the two sets of results. It should be noted that, unlike micelles with BACD or BADC block sequences, many of the micelles with the BCAD block sequence exhibited incomplete or even somewhat poor hydrophilic coverage.

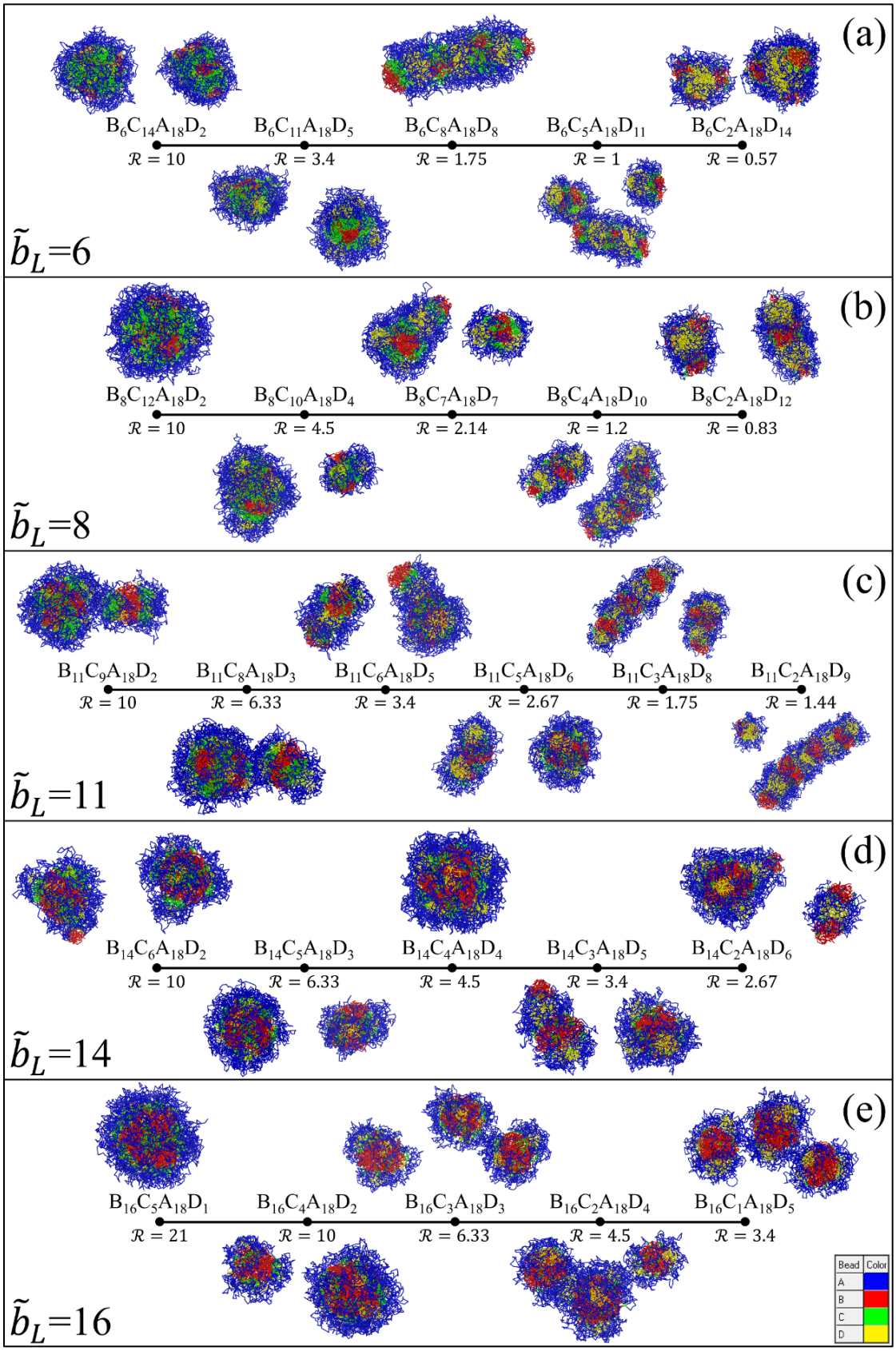

Figure 27. DPD results for tetrablock copolymers with the BCAD block sequence, separated by lipophilic block (B) length.

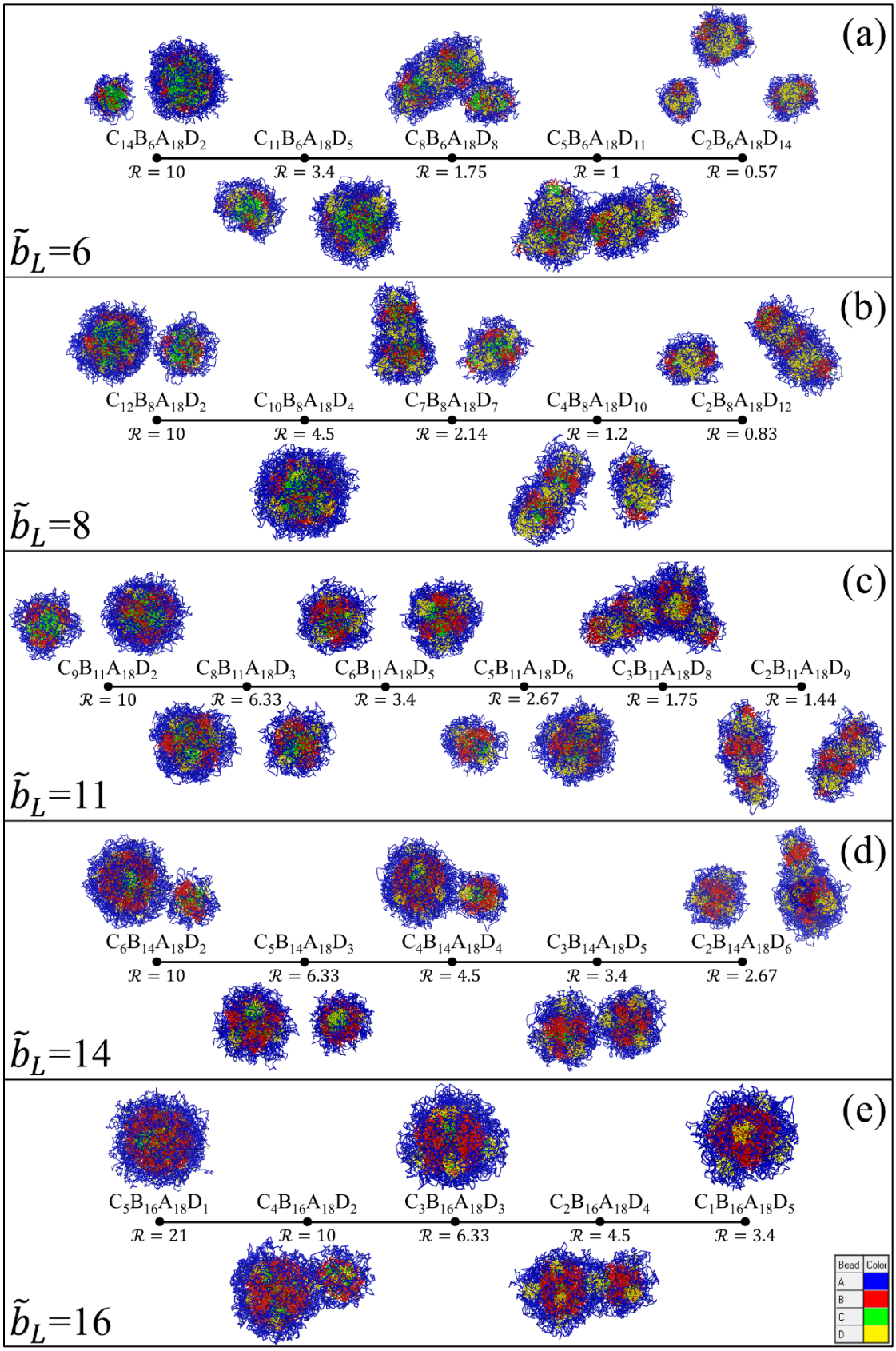

Figure 28. DPD results for tetrablock copolymers with the CBAD block sequence, separated by lipophilic block (B) length.

For architectures with $\tilde{b}_L = 6$, a wide range of tunability was observed. As in the case of BAC micelles[66-67], micelles with $\mathcal{R} \ll 1$ (e.g., $B_6C_2A_{18}D_{14}$) or $\mathcal{R} \gg 1$ (e.g., $B_6C_{14}A_{18}D_2$) formed spheroids with the species on the heavier end of the lever comprising the core and the species at the lighter end forming patches surrounding the core. By contrast, for $\mathcal{R}$ near unity, significantly less spheroidal morphologies were observed, with a preference for linear, segmented morphologies arising instead. In either case, the relative layering of the lipophilic and fluorophilic blocks was determined by the polymer architecture: the terminal block formed the core, while the internal block formed a layer surrounding it.

Similar trends in both self-assembly and tunability were observed for longer lipophilic blocks as well, although for the block lengths tested, the stabilizing effect of the increasing lipophilic block length made micelles with superhydrophobic cores increasingly difficult to achieve. Indeed, in BCAD systems, no spheroidal micelles with cores composed of the superhydrophobic species were observed beyond $\tilde{b}_L = 8$, due the difficulty of achieving $\mathcal{R} \ll 1$ with the lipophilic block length becoming increasingly large; none were observed beyond $\tilde{b}_L = 6$ in systems with the CBAD block sequence. Moreover, beyond $\tilde{b}_L = 11$, no linear segmented micelles were formed in systems with either block sequence, as the block lengths tested made achieving $\mathcal{R} \approx 1$ impossible as well. For $\tilde{b}_L = 14$ and $\tilde{b}_L = 16$, exclusively spheroidal micelles were formed, with superhydrophobic patches of varying size. In BCAD systems, the core was composed of the terminal (lipophilic) species for all architectures with $\tilde{b}_L = 14$ or $\tilde{b}_L = 16$.

By contrast, in CBAD systems, the terminal (fluorophilic) species occupied the core in most of the architectures with $\tilde{b}_L = 11$, $\tilde{b}_L = 14$, or $\tilde{b}_L = 16$, but for architectures with $\mathcal{R}_a \gtrapprox 5$, the fluorophilic species was present in too small an amount to form a stable core. In these cases, the fluorophilic core begins to form arms extending outward toward the superhydrophobic patches

surrounding the core, while the lipophilic layer moves inward and supplants the fluorophilic species in the micelle core. For large $\mathcal{R}_a$-values, such as the cases of $C_2B_{16}A_{18}D_4$ and $C_1B_{16}A_{18}D_5$, the lipophilic species essentially displaced the fluorophilic species from the core altogether.

6.3. Polymer Architectures with Block Sequence BDAC or CABD

The morphologies of the final two sets of block sequences, BDAC and CABD, are shown in Figure 29 and Figure **30** on pages 80-81, respectively. Although the general morphologies corresponded well to the $\mathcal{R}$-values in both cases, BDAC morphologies exhibited worse hydrophilic coverage than any other block sequence tested in this study. A small number of CABD morphologies also demonstrated poor hydrophilic coverage, but this was predominantly limited to architectures with short lipophilic block lengths (among CBAD architectures tested, incomplete coverage was observed only in those with $\tilde{b}_L = 6$). By contrast, large regions of exposed lipophilic species were present in BDAC micelles across all lipophilic block lengths tested.

Aside from this, the trends in both BDAC and CABD micelles were quite similar to those observed for BCAD and CBAD micelles, respectively, with the role of the fluorophilic and superhydrophobic species reversed. For micelles with BDAC or CABD block sequences, wider ranges of tunability were present in architectures with shorter lipophilic block lengths ($\tilde{b}_L = 6$ or $\tilde{b}_L = 8$). In these architectures, for $\mathcal{R} \gg 1$, spheroidal micelles were formed in both block sequences, with the terminal block (lipophilic in the case of BDAC and superhydrophobic in the case of CABD) forming the core and the internal block forming a layer surrounding the core. The fluorophilic species formed patches surrounding the micelle core. For $\mathcal{R} \approx 1$, segmented micelles formed with alternating fluorophilic blocks and blocks composed of cores of the terminal species surrounded by layers of the internal species. Finally, architectures with $\mathcal{R} \ll 1$ formed spheroids with fluorophilic cores surrounded by layered patches composed of a core of the terminal species

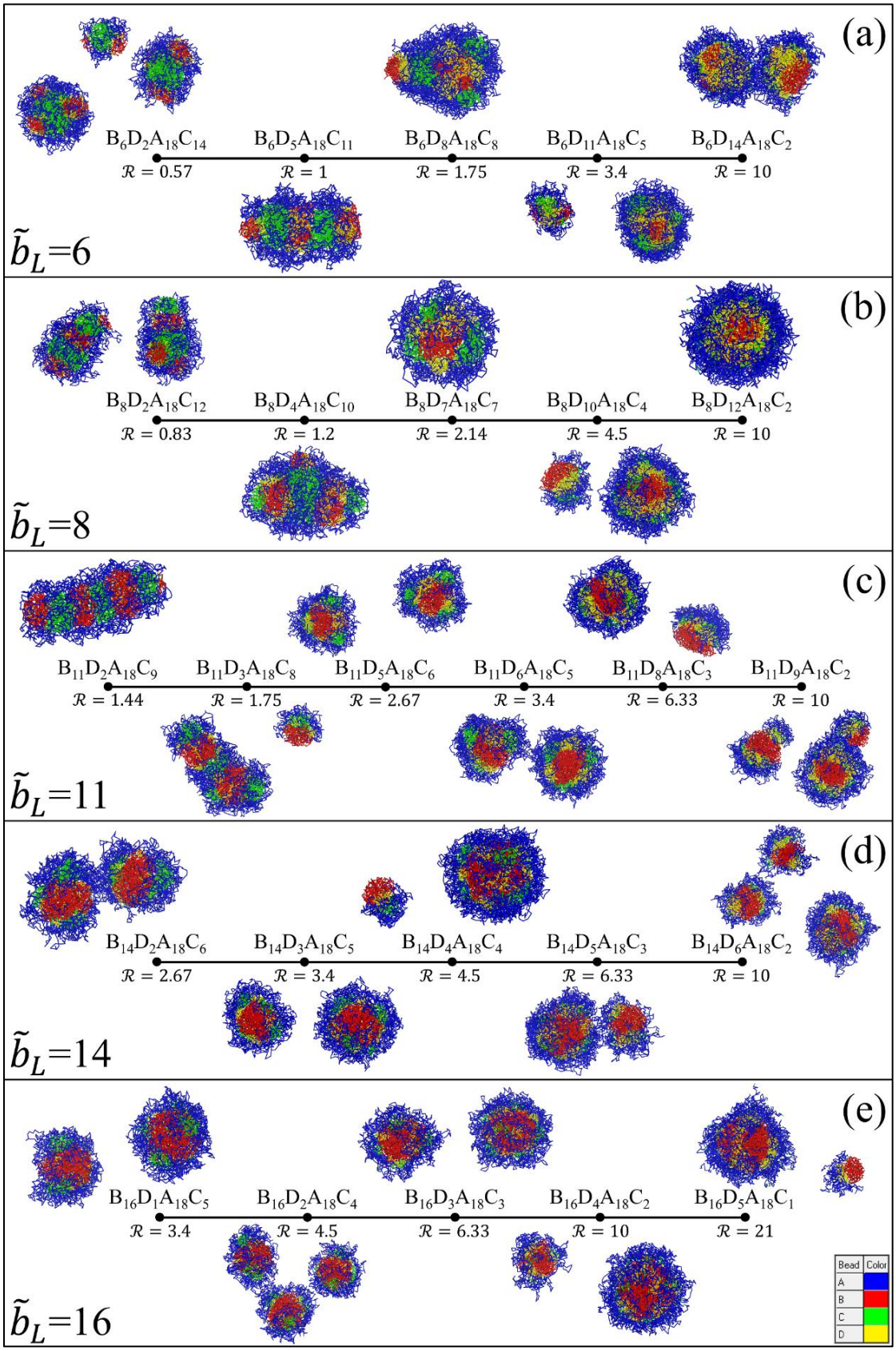

Figure 29. DPD results for tetrablock copolymers with the BDAC block sequence, separated by lipophilic block (B) length.

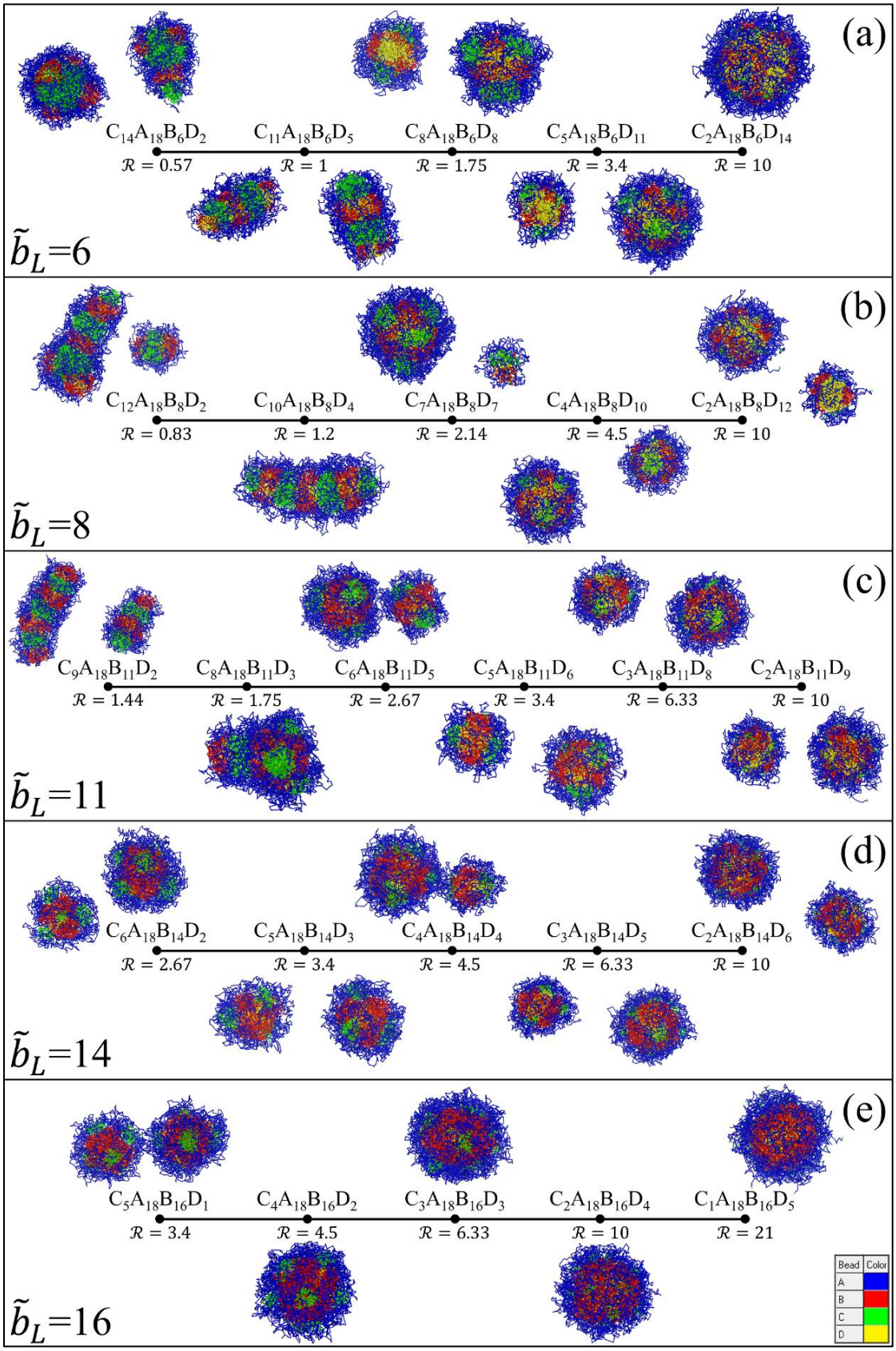

Figure 30. DPD results for tetrablock copolymers with the CABD block sequence, separated by lipophilic block (B) length.

surrounded by a layer of the internal species.

As in the case of BCAD and CBAD micelles, increasing the length of the lipophilic block made spheroidal micelles with fluorophilic cores harder to achieve, in agreement with the increasing $\mathcal{R}$-values. Indeed, no such micelles were formed beyond $\tilde{b}_L = 8$ for either the BDAC or the CABD block sequences; beyond $\tilde{b}_L = 11$, no linear micelles were formed, due to the $\mathcal{R}$-value being considerably higher than unity beyond this point.

For micelles with $\tilde{b}_L = 14$ and $\tilde{b}_L = 16$, only spheroidal micelles were formed, with the cores being composed of the (lipophilic) block in all BDAC micelles. Instead of a complete coating around the micelle core, the superhydrophobic species formed in large patches surrounding the core, behaving identically to the fluorophilic species. By contrast, in CABD micelles, the micelle core was still composed of the terminal (superhydrophobic) species in most cases, but was displaced in the core by the internal (lipophilic) block in cases where $\mathcal{R}_a$ was quite large; as in the case of CBAD micelles, beginning in architectures with $\mathcal{R}_a \gtrapprox 5$, as the terminal block began to be displaced in the core by the internal block, the terminal block began to extend outward in arms toward the patches composed of the species on the opposite side of the hydrophilic block (in this case, the fluorophilic species).

This computational study has led to a compact expression which has proven robust and applicable to all six of the block sequences studied. Equation (53) presents this quite general expression, but the authors acknowledge that while this expression allows for structural predictions to be made for copolymers beyond three blocks in length, it requires the assumption of linearity in its application. Nonetheless, by analogy with previous studies[66-67], a potential expression may be suggested which avoids this assumption:

$$\mathcal{R}' = \sum_{\text{Group 1}} \tilde{b}_{\text{i}}(\tilde{s}_{\text{i}} + 1) / \sum_{\text{Group 2}} \tilde{b}_{\text{j}}\left(\tilde{s}_{\text{j}} + 1\right) \tag{55}$$

Here an alternative expression without reduced lengths may again be substituted, as in equation (53), as the coarse-graining scaling factor should be similar for all species.

The expression in equation (53) offers much of the same appeal as the earlier structural parameters put forth in Chapters 4-5, particularly in its simplicity and ability to characterize the micelle morphology formed by a particular polymer using only architectural elements of the polymer itself. Equation (53) also collapses into the previous linear form when considering linear triblock copolymers, and the expression for $\mathcal{R}'$ in equation (55) would collapse into the previous generalized form of equation (52) when considering branched triblock copolymers, although the author cautions that equation (55) is merely a predicted equation based on prior studies and has not yet been tested through simulation studies.

In the case of tetrablock copolymer micelles, an auxiliary structural parameter arises in the form of $\mathcal{R}_a$, which allows for additional tunability even at constant $\mathcal{R}$. Copolymers with more than four blocks may see the appearance of additional auxiliary structural parameters. As such, it is advisable to seek additional trends in more complex polymer systems, in order to maximize the control that the experimental chemist may exert over micelle morphology.

Finally, it should be noted that the structural parameters set forth in this and in prior studies, while offering accurate predictions for the chosen systems, do not necessarily generalize to other systems with markedly different repulsion parameters (i.e., χ-parameters/interspecies miscibility). It is expected that there will be some flexibility in the proposed structural parameters with respect to the miscibility of various species, but this flexibility will undoubtedly have limitations, and systems with drastically different ranges of miscibility may see lower accuracy in the predictions generated by the $\mathcal{R}$-value. As such, further studies are underway in order to expand the $\mathcal{R}$-value to consider the thermodynamic effect of different repulsion parameters as well.

7. CONCLUSION

The foregoing chapters form the complete narrative of a computational study beginning with the development of a computational methodology for approximating the Flory-Huggins χ-parameter and continuing through several coarse-grained simulation studies on micelle self-aggregation. In order to design realistic coarse-grained simulation systems, miscibility calculations were performed through the methodology outlined in Chapter 3, then converted into repulsion parameters for use in dissipative particle dynamics simulations. The coarse-grained simulation studies described in great detail in Chapters 4-6 are focused around the progressive development of a generalized structural parameter $\mathcal{R}$ which offers accurate predictions as to the morphology of both triblock and tetrablock micelles with internal hydrophilic blocks.

Following the tetrablock study discussed in Chapter 6, the structural parameter for linear systems assumes the general form given below, where group 1 refers to the species on the same side of the hydrophilic block as the lipophilic block and group 2 to those on the opposite side:

$$\mathcal{R} = \frac{\sum_{\text{Group 1}} \tilde{b}_{\text{i}}}{\sum_{\text{Group 2}} \tilde{b}_{\text{j}}} \approx \frac{\sum_{\text{Group 1}} b_{\text{i}}}{\sum_{\text{Group 2}} b_{\text{j}}}$$

The lipophilic block is chosen as a defining species only in order to preserve the ability to compare this expression to those derived earlier. In particular, when group 1 contains only the lipophilic species (B) and group 2 contains only the fluorophilic species (C), $\mathcal{R}$ simplifies into the *linear* structural parameter $\mathcal{R}_l$ discussed in Chapter 4. A proposed extension of this parameter was given near the end of Chapter 6, which in turn collapses into the structural parameter for *branched* triblock copolymer micelles. If no lipophilic block is present in the system, another species may be substituted without loss of generality; the operative concept of this model is that the hydrophilic block acts as a fulcrum in all copolymer systems in which it comprises an internal block.

8. FUTURE WORK

Despite the success of the preceding studies, there exists room for further refinement in both the miscibility analysis methodology and the form of the structural parameter $\mathcal{R}$. In the case of the former, additional studies into the effect of various factors offer the potential to further increase the accuracy of the χ-parameter simulation method. These factors include the effect of Coulombic interactions which use a linearly varying dielectric constant instead of a constant which is irrespective of interatomic separation, as well as the effect of coordination number on the overestimation of the binding energy in using Materials Studio's Blends module[195]. Initial investigations into these effects have been undertaken by other computational colleagues of the author, but a formal review will help establish a conclusive answer as to their significance.

Several avenues toward further generalizing the $\mathcal{R}$-value have been proposed by the author in preceding chapters as well. The most intriguing of these is the introduction of thermodynamic data into the $\mathcal{R}$-parameter itself; the studies conducted herein present a range of morphological tunability based on a specific set of repulsion parameters (and thus, by extension, χ-values). It is expected that the general predictions established by this set of representative repulsion parameters will extend to other systems, but the values at which the transitions between morphological regimes occur are likely to differ from those discussed here (namely, the straightforward division of regimes by $\mathcal{R} \ll 1$, $\mathcal{R} \approx 1$, and $\mathcal{R} \gg 1$).

In order to offer more refined predictive accuracy, a study presently underway by the author and colleagues to incorporate thermodynamic information will hopefully prove illustrative. In addition to these thermodynamic studies, six other tetrablock sequences (specifically, those with terminal hydrophilic blocks) remain unexplored; these sequences may offer new and useful morphologies and are therefore worthy of study.

Finally, transport characteristics based on micelle morphology would be of great interest to synthetic chemists. An existing study by a colleague of the author demonstrates the feasibility of this study using dissipative particle dynamics[58]. Additional studies which apply this technique to additional morphologies will uncover volumes of essential information regarding the applicability of these micelle systems to nanoreactor applications.

REFERENCES

1. Trost, B. M. The Atom Economy--a Search for Synthetic Efficiency. *Science* **1991**, *254*, 1471-1477.
2. Trost, B. M. Atom Economy—a Challenge for Organic Synthesis: Homogeneous Catalysis Leads the Way. *Angewandte Chemie International Edition in English* **1995**, *34*, 259-281.
3. Sheldon, R. A. Atom Efficiency and Catalysis in Organic Synthesis. *Pure and Applied Chemistry* **2000**, *72*, 1233-1246.
4. Lam, A. Y. S.; Li, V. O. K. Chemical-Reaction-Inspired Metaheuristic for Optimization. *IEEE Transactions on Evolutionary Computation* **2010**, *14*, 381-399.
5. Lam, A. Y. S.; Li, V. O. K. Chemical Reaction Optimization: A Tutorial. *Memetic Computing* **2012**, *4*, 3-17.
6. Szeto, W. Y.; Wang, Y.; Wong, S. C. The Chemical Reaction Optimization Approach to Solving the Environmentally Sustainable Network Design Problem. *Computer-Aided Civil and Infrastructure Engineering* **2014**, *29*, 140-158.
7. Winnacker, M.; Vagin, S.; Rieger, B. Cooperative Catalysis in Polymerization Reactions. In *Cooperative Catalysis: Designing Efficient Catalysts for Synthesis*, 2015.
8. McCarroll, A. J.; Walton, J. C. Programming Organic Molecules: Design and Management of Organic Syntheses through Free-Radical Cascade Processes. *Angewandte Chemie International Edition* **2001**, *40*, 2224-2248.
9. Madhavan, N.; Jones, C. W.; Weck, M. Rational Approach to Polymer-Supported Catalysts: Synergy between Catalytic Reaction Mechanism and Polymer Design. *Accounts of Chemical Research* **2008**, *41*, 1153-1165.
10. Weck, M.; Jones, C. W. Mizoroki−Heck Coupling Using Immobilized Molecular Precatalysts: Leaching Active Species from Pd Pincers, Entrapped Pd Salts, and Pd Nhc Complexes. *Inorganic Chemistry* **2007**, *46*, 1865-1875.
11. Long, W. Designing Immobilized Catalysts for Chemical Transformations: New Platforms to Tune the Accessibility of Active Sites. Dissertation, Georgia Institute of Technology, Atlanta, 2012.
12. End, N.; Schöning, K.-U. Immobilized Catalysts in Industrial Research and Application. In *Immobilized Catalysts: Solid Phases, Immobilization and Applications*, Kirschning, A., Ed. Springer-Verlag: Berlin, 2004; Vol. 242.
13. Trapp, O.; Troendlin, J. Studies of Immobilized Catalysts. In *Molecular Catalysts: Structure and Functional Design*, Gade, L. H.; Hofmann, P., Eds. Wiley-VCH: 2014.
14. Hübner, S.; de Vries, J. G.; Farina, V. Why Does Industry Not Use Immobilized Transition Metal Complexes as Catalysts? *Advanced Synthesis & Catalysis* **2016**, *358*, 3-25.
15. Cozzi, F. Immobilization of Organic Catalysts: When, Why, and How. *Advanced Synthesis & Catalysis* **2006**, *348*, 1367-1390.
16. Sabater, S.; Mata, J. A.; Peris, E. Catalyst Enhancement and Recyclability by Immobilization of Metal Complexes onto Graphene Surface by Noncovalent Interactions. *ACS Catalysis* **2014**, *4*, 2038-2047.
17. Huang, H.; Denard, C. A.; Alamillo, R.; Crisci, A. J.; Miao, Y.; Dumesic, J. A.; Scott, S. L.; Zhao, H. Tandem Catalytic Conversion of Glucose to 5-Hydroxymethylfurfural with an Immobilized Enzyme and a Solid Acid. *ACS Catalysis* **2014**, *4*, 2165-2168.
18. Lohr, T. L.; Marks, T. J. Orthogonal Tandem Catalysis. *Nature Chemistry* **2015**, *7*, 477.

19. Chapuis, C.; Barthe, M.; de Saint Laumer, J. Y. Synthesis of Citronellal by Rhi-Catalysed Asymmetric Isomerization of N,N-Diethyl-Substituted Geranyl- and Nerylamines or Geraniol and Nerol in the Presence of Chiral Diphosphino Ligands, under Homogeneous and Supported Conditions. *Helvetica Chimica Acta* **2001**, *84*, 230-242.
20. Rosser, T. E.; Reisner, E. Understanding Immobilized Molecular Catalysts for Fuel-Forming Reactions through Uv/Vis Spectroelectrochemistry. *ACS Catalysis* **2017**, *7*, 3131-3141.
21. Bullock, R. M.; Das, A. K.; Appel, A. M. Surface Immobilization of Molecular Electrocatalysts for Energy Conversion. *Chemistry – A European Journal* **2017**, *23*, 7626-7641.
22. Song, C. E.; Yang, J. W.; Roh, E. J.; Lee, S. G.; Ahn, J. H.; Han, H. Heterogeneous Pd-Catalyzed Asymmetric Allylic Substitution Using Resin-Supported Trost-Type Bisphosphane Ligands. *Angewandte Chemie International Edition* **2002**, *41*, 3852-3854.
23. Annis, D. A.; Jacobsen, E. N. Polymer-Supported Chiral Co(Salen) Complexes: Synthetic Applications and Mechanistic Investigations in the Hydrolytic Kinetic Resolution of Terminal Epoxides. *J. Am. Chem. Soc.* **1999**, *121*, 4147-4154.
24. Peukert, S.; Jacobsen, E. N. Enantioselective Parallel Synthesis Using Polymer-Supported Chiral Co(Salen) Complexes. *Organic Letters* **1999**, *1*, 1245-1248.
25. Poli, R. Site Isolation for Non-Orthogonal Tandem Catalysis in Confined Nanospaces. In *Effects of Nanoconfinement on Catalysis*, Poli, R., Ed. Springer International Publishing: Cham, 2017; pp 209-258.
26. Shunichi, F.; Yong-Min, L.; Wonwoo, N. Immobilization of Molecular Catalysts for Enhanced Redox Catalysis. *ChemCatChem* **2018**, *10*, 1686-1702.
27. Yang, H.; Fu, L.; Wei, L.; Liang, J.; Binks, B. P. Compartmentalization of Incompatible Reagents within Pickering Emulsion Droplets for One-Pot Cascade Reactions. *J. Am. Chem. Soc.* **2015**, *137*, 1362-1371.
28. Dydio, P.; Ploeger, M.; Reek, J. N. H. Selective Isomerization–Hydroformylation Sequence: A Strategy to Valuable A-Methyl-Branched Aldehydes from Terminal Olefins. *ACS Catalysis* **2013**, *3*, 2939-2942.
29. Jain, S.; Zheng, X.; Jones, C. W.; Weck, M.; Davis, R. J. Importance of Counterion Reactivity on the Deactivation of Co−Salen Catalysts in the Hydrolytic Kinetic Resolution of Epichlorohydrin. *Inorganic Chemistry* **2007**, *46*, 8887-8896.
30. Lu, J.; Dimroth, J.; Weck, M. Compartmentalization of Incompatible Catalytic Transformations for Tandem Catalysis. *J. Am. Chem. Soc.* **2015**, *137*, 12984-12989.
31. Hopwood, D. A.; Sherman, D. H. Molecular Genetics of Polyketides and Its Comparison to Fatty Acid Biosynthesis. *Annual Review of Genetics* **1990**, *24*, 37-62.
32. Arigoni, D.; Sagner, S.; Latzel, C.; Eisenreich, W.; Bacher, A.; Zenk, M. H. Terpenoid Biosynthesis from 1-Deoxy-D-Xylulose in Higher Plants by Intramolecular Skeletal Rearrangement. *Proceedings of the National Academy of Sciences of the United States of America* **1997**, *94*, 10600-10605.
33. Agapakis, C. M.; Boyle, P. M.; Silver, P. A. Natural Strategies for the Spatial Optimization of Metabolism in Synthetic Biology. *Nature Chemical Biology* **2012**, *8*, 527.
34. Shi, J.; Zhang, L.; Jiang, Z. Facile Construction of Multicompartment Multienzyme System through Layer-by-Layer Self-Assembly and Biomimetic Mineralization. *ACS Applied Materials & Interfaces* **2011**, *3*, 881-889.

35. Miller, A. L., II; Bowden, N. B. A Materials Approach to the Dual-Site Isolation of Catalysts Bonded to Linear Polymers and Small, Ionic Molecules for Use in One-Pot Cascade Reactions. *Advanced Materials* **2008**, *20*, 4195-4199.
36. Slomkowski, S., et al. Terminology of Polymers and Polymerization Processes in Dispersed Systems. *Pure and Applied Chemistry* **2011**, *83*, 2229.
37. Hartley, G. S. *Aqueous Solutions of Paraffin-Chain Salts; a Study in Micelle Formation*; Hermann & cie: Paris, 1936.
38. Laschewsky, A. Polymerized Micelles with Compartments. *Current Opinion in Colloid & Interface Science* **2003**, *8*, 274-281.
39. Kubowicz, S.; Baussard, J. F.; Lutz, J. F.; Thünemann, A. F.; von Berlepsch, H.; Laschewsky, A. Multicompartment Micelles Formed by Self-Assembly of Linear Abc Triblock Copolymers in Aqueous Medium. *Angewandte Chemie International Edition* **2005**, *44*, 5262-5265.
40. Lutz, J. F.; Laschewsky, A. Multicompartment Micelles: Has the Long-Standing Dream Become a Reality? *Macromolecular Chemistry and Physics* **2005**, *206*, 813-817.
41. Marsat, J.-N.; Heydenreich, M.; Kleinpeter, E.; Berlepsch, H. v.; Böttcher, C.; Laschewsky, A. Self-Assembly into Multicompartment Micelles and Selective Solubilization by Hydrophilic−Lipophilic−Fluorophilic Block Copolymers. *Macromolecules* **2011**, *44*, 2092-2105.
42. Li, Z.; Kesselman, E.; Talmon, Y.; Hillmyer, M. A.; Lodge, T. P. Multicompartment Micelles from Abc Miktoarm Stars in Water. *Science* **2004**, *306*, 98-101.
43. Moughton, A. O.; Hillmyer, M. A.; Lodge, T. P. Multicompartment Block Polymer Micelles. *Macromolecules* **2012**, *45*, 2-19.
44. Moughton, A. O.; Sagawa, T.; Yin, L.; Lodge, T. P.; Hillmyer, M. A. Multicompartment Micelles by Aqueous Self-Assembly of M-a(Bc)N Miktobrush Terpolymers. *ACS Omega* **2016**, *1*, 1027-1033.
45. Lal, M.; Kumar, N. D.; Joshi, M. P.; Prasad, P. N. Polymerization in a Reverse Micelle Nanoreactor: Preparation of Processable Poly(P-Phenylenevinylene) with Controlled Conjugation Length. *Chemistry of Materials* **1998**, *10*, 1065-1068.
46. Vriezema, D. M.; Comellas Aragonès, M.; Elemans, J. A. A. W.; Cornelissen, J. J. L. M.; Rowan, A. E.; Nolte, R. J. M. Self-Assembled Nanoreactors. *Chemical Reviews* **2005**, *105*, 1445-1490.
47. Peters, R. J. R. W.; Louzao, I.; van Hest, J. C. M. From Polymeric Nanoreactors to Artificial Organelles. *Chemical Science* **2012**, *3*, 335-342.
48. Adıgüzel, R.; Taşcıoğlu, S. Micelle Nano-Reactors as Mediators of Water-Insoluble Ligand Complexation with Cu(Ii) Ions in Aqueous Medium. *Chemical Papers* **2013**, *67*, 456-463.
49. Marguet, M.; Bonduelle, C.; Lecommandoux, S. Multicompartmentalized Polymeric Systems: Towards Biomimetic Cellular Structure and Function. *Chemical Society Reviews* **2013**, *42*, 512-529.
50. Longstreet, A. R.; McQuade, D. T. Organic Reaction Systems: Using Microcapsules and Microreactors to Perform Chemical Synthesis. *Accounts of Chemical Research* **2013**, *46*, 327-338.
51. Wang, H.; Liu, Y.-T.; Qian, H.-J.; Lu, Z.-Y. Dissipative Particle Dynamics Simulation Study on Complex Structure Transitions of Vesicles Formed by Comb-Like Block Copolymers. *Polymer* **2011**, *52*, 2094-2101.

52. Bakshi, M. S. Colloidal Micelles of Block Copolymers as Nanoreactors, Templates for Gold Nanoparticles, and Vehicles for Biomedical Applications. *Advances in Colloid and Interface Science* **2014**, *213*, 1-20.
53. Lee, L.-C.; Lu, J.; Weck, M.; Jones, C. W. Acid–Base Bifunctional Shell Cross-Linked Micelle Nanoreactor for One-Pot Tandem Reaction. *ACS Catalysis* **2016**, *6*, 784-787.
54. Scarso, A. Micellar Nanoreactors. In *Encyclopedia of Inorganic and Bioinorganic Chemistry*, Scott, R. A., Ed. 2016.
55. Trinh, T.; Chidchob, P.; Bazzi, H. S.; Sleiman, H. F. DNA Micelles as Nanoreactors: Efficient DNA Functionalization with Hydrophobic Organic Molecules. *Chemical Communications* **2016**, *52*, 10914-10917.
56. Boucher-Jacobs, C.; Rabnawaz, M.; Katz, J. S.; Even, R.; Guironnet, D. Encapsulation of Catalyst in Block Copolymer Micelles for the Polymerization of Ethylene in Aqueous Medium. *Nature Communications* **2018**, *9*, 841.
57. De Martino, M. T.; Abdelmohsen, L. K. E. A.; Rutjes, F. P. J. T.; van Hest, J. C. M. Nanoreactors for Green Catalysis. *Beilstein Journal of Organic Chemistry* **2018**, *14*, 716-733.
58. Lee, S. M.; Bond, N.; Callaway, C.; Clark, B.; Farmer, E.; Mallard, M.; Jang, S. S. Dissipative Particle Dynamics Simulation of Multicompartment Micelle Nanoreactor with Channel for Reactants. *RSC Advances* **2018**, *8*, 37866-37871.
59. Wanderlind, E. H.; Orth, E. S.; Medeiros, M.; Santos, D. M. P. O.; Westphal, E.; Gallardo, H.; Fiedler, H. D.; Nome, F. Aqueous Micelles as Catalytic Nanoreactors for Dephosphorylation Reactions. *Journal of the Brazilian Chemical Society* **2014**, *25*, 2385-2391.
60. Chou, S.-H.; Tsao, H.-K.; Sheng, Y.-J. Morphologies of Multicompartment Micelles Formed by Triblock Copolymers. *The Journal of Chemical Physics* **2006**, *125*, 194903.
61. Callaway, C. P.; Hendrickson, K.; Bond, N.; Lee, S.; Sood, P.; Jang, S. S. Molecular Modeling Approach to Determine the Flory-Huggins Interaction Parameter for Polymer Miscibility Analysis. *ChemPhysChem* **2018**, *19*, 1655-1664.
62. Sears, J. S.; Sherrill, C. D. Assessing the Performance of Density Functional Theory for the Electronic Structure of Metal−Salens: The 3d0-Metals. *The Journal of Physical Chemistry A* **2008**, *112*, 3466-3477.
63. Sears, J. S.; Sherrill, C. D. Assessing the Performance of Density Functional Theory for the Electronic Structure of Metal−Salens: The D2-Metals. *The Journal of Physical Chemistry A* **2008**, *112*, 6741-6752.
64. Takatani, T.; Sears, J. S.; Sherrill, C. D. Assessing the Performance of Density Functional Theory for the Electronic Structure of Metal−Salens: The D6-Metals. *The Journal of Physical Chemistry A* **2009**, *113*, 9231-9236.
65. Takatani, T.; Sears, J. S.; Sherrill, C. D. Assessing the Performance of Density Functional Theory for the Electronic Structure of Metal−Salens: The M06 Suite of Functionals and the D4-Metals. *The Journal of Physical Chemistry A* **2010**, *114*, 11714-11718.
66. Callaway, C. P.; Bond, N.; Hendrickson, K.; Lee, S. M.; Jang, S. S. Structural Tunability of Multicompartment Micelles as a Function of Lipophilic–Fluorophilic Block Length Ratio. *The Journal of Physical Chemistry B* **2018**, *122*, 12164-12172.
67. Callaway, C. P.; Lee, S. M.; Mallard, M.; Clark, B.; Jang, S. S. Effect of Block Length and Side Chain Length Ratios on Determining a Multicompartment Micelle Structure. *The Journal of Physical Chemistry B* **2019**, *123*, 4784-4791.
68. Flory, P. J. Thermodynamics of High Polymer Solutions. *J. Chem. Phys.* **1942**, *10*, 51-61.
69. Huggins, M. L. Theory of Solutions of High Polymers. *J. Phys. Chem.* **1942**, *64*, 1712-1719.

70. Aminabhavi, T. M.; Balundgi, R. H. A Simple and Alternative Method to Derive Delta-Hmix in Flory-Huggins Lattice Theory. *J. Chem. Educ.* **1986**, *63*, 581-581.
71. Rubinstein, M.; Colby, R. H. *Polymer Physics*; Oxford University Press: New York, 2003.
72. Jensen, F. *Introduction to Computational Chemistry*, 2 ed.; Wiley: Chichester, 2007.
73. Pathria, R. K.; Beale, P. D. *Statistical Mechanics*, 3 ed.; Butterworth-Heinemann: Oxford, 2011.
74. Hehre, W. J. Ab Initio Molecular Orbital Theory. *Accounts of Chemical Research* **1976**, *9*, 399-406.
75. Hehre, W. J.; Radom, L.; Schleyer, P. v. R.; Pople, J. *Ab Initio Molecular Orbital Theory*, 1 ed.; Wiley-Interscience: New York, 1986.
76. Hartree, D. R. The Wave Mechanics of an Atom with a Non-Coulomb Central Field. Part I. Theory and Methods. *Mathematical Proceedings of the Cambridge Philosophical Society* **2008**, *24*, 89-110.
77. Gaunt, J. A. A Theory of Hartree's Atomic Fields. *Mathematical Proceedings of the Cambridge Philosophical Society* **2008**, *24*, 328-342.
78. Slater, J. C. The Self Consistent Field and the Structure of Atoms. *Physical Review* **1928**, *32*, 339-348.
79. Echenique, P.; Alonso, J. L. A Mathematical and Computational Review of Hartree–Fock Scf Methods in Quantum Chemistry. *Molecular Physics* **2007**, *105*, 3057-3098.
80. Fock, V. Näherungsmethode Zur Lösung Des Quantenmechanischen Mehrkörperproblems. *Zeitschrift für Physik* **1930**, *61*, 126-148.
81. Stone, A. J. *The Theory of Intermolecular Forces*, 2 ed.; Oxford University Press: Oxford, 2013.
82. Cramer, C. J. *Essentials of Computational Chemistry: Theories and Models*, 1 ed.; Wiley: Chichester, 2002.
83. Maurice, D.; Head-Gordon, M. Analytical Second Derivatives for Excited Electronic States Using the Single Excitation Configuration Interaction Method: Theory and Application to Benzo[a]Pyrene and Chalcone. *Molecular Physics* **1999**, *96*, 1533-1541.
84. Head-Gordon, M.; Rico, R. J.; Oumi, M.; Lee, T. J. A Doubles Correction to Electronic Excited States from Configuration Interaction in the Space of Single Substitutions. *Chemical Physics Letters* **1994**, *219*, 21-29.
85. Purvis, G. D.; Bartlett, R. J. A Full Coupled-Cluster Singles and Doubles Model: The Inclusion of Disconnected Triples. *The Journal of Chemical Physics* **1982**, *76*, 1910-1918.
86. Raghavachari, K.; Trucks, G. W.; Pople, J. A.; Head-Gordon, M. A Fifth-Order Perturbation Comparison of Electron Correlation Theories. *Chemical Physics Letters* **1989**, *157*, 479-483.
87. Voorhis, T. V.; Head-Gordon, M. Two-Body Coupled Cluster Expansions. *The Journal of Chemical Physics* **2001**, *115*, 5033-5040.
88. Møller, C.; Plesset, M. S. Note on an Approximation Treatment for Many-Electron Systems. *Physical Review* **1934**, *46*, 618-622.
89. Pople, J. A.; Head-Gordon, M.; Raghavachari, K. Quadratic Configuration Interaction. A General Technique for Determining Electron Correlation Energies. *The Journal of Chemical Physics* **1987**, *87*, 5968-5975.
90. Slater, J. C. Atomic Shielding Constants. *Physical Review* **1930**, *36*, 57-64.
91. Boys, S. F. Electronic Wave Functions - I. A General Method of Calculation for the Stationary States of Any Molecular System. *Proceedings of the Royal Society of London. Series A. Mathematical and Physical Sciences* **1950**, *200*, 542-554.

92. Gill, P. M. W. Molecular Integrals over Gaussian Basis Functions. In *Advances in Quantum Chemistry*, Sabin, J. R.; Zerner, M. C., Eds. Academic Press: 1994; Vol. 25, pp 141-205.
93. Regier, P. E.; Fisher, J.; Sharma, B. S.; Thakkar, A. J. Gaussian Vs. Slater Representations of D Orbitals: An Information Theoretic Appraisal Based on Both Position and Momentum Space Properties. *Int. J. Quantum Chem.* **1985**, *28*, 429-449.
94. Roothaan, C. C. J. New Developments in Molecular Orbital Theory. *Reviews of Modern Physics* **1951**, *23*, 69-89.
95. Hall, G. G. The Molecular Orbital Theory of Chemical Valency Viii. A Method of Calculating Ionization Potentials. *Proceedings of the Royal Society of London. Series A. Mathematical and Physical Sciences* **1951**, *205*, 541-552.
96. Kohn, W.; Sham, L. J. Self-Consistent Equations Including Exchange and Correlation Effects. *Physical Review* **1965**, *140*, A1133-A1138.
97. Parr, R. G.; Yang, W. *Density-Functional Theory of Atoms and Molecules*, 1 ed.; Oxford University Press: Oxford, 1994.
98. Dreizler, R. M.; Gross, E. K. U. *Density Functional Theory: An Approach to the Quantum Many-Body Problem*, 1 ed.; Springer-Verlag: Berlin, 1990.
99. Hohenberg, P.; Kohn, W. Inhomogeneous Electron Gas. *Physical Review* **1964**, *136*, B864-B871.
100. Levy, M. Universal Variational Functionals of Electron Densities, First-Order Density Matrices, and Natural Spin-Orbitals and Solution of the <Em>V</Em>-Representability Problem. *Proceedings of the National Academy of Sciences* **1979**, *76*, 6062-6065.
101. Vignale, G.; Rasolt, M. Density-Functional Theory in Strong Magnetic Fields. *Phys. Rev. Lett.* **1987**, *59*, 2360-2363.
102. Amusia, M. Y.; Msezane, A. Z.; Shaginyan, V. R. Density Functional Theory Versus the Hartree–Fock Method: Comparative Assessment. *Physica Scripta* **2003**, *68*, C133.
103. Perdew, J. P.; Zunger, A. Self-Interaction Correction to Density-Functional Approximations for Many-Electron Systems. *Physical Review B* **1981**, *23*, 5048-5079.
104. Perdew, J. P.; Chevary, J. A.; Vosko, S. H.; Jackson, K. A.; Pederson, M. R.; Singh, D. J.; Fiolhais, C. Atoms, Molecules, Solids, and Surfaces: Applications of the Generalized Gradient Approximation for Exchange and Correlation. *Physical Review B* **1992**, *46*, 6671-6687.
105. Perdew, J. P.; Burke, K.; Ernzerhof, M. Generalized Gradient Approximation Made Simple. *Phys. Rev. Lett.* **1996**, *77*, 3865-3868.
106. Becke, A. D. Density-Functional Exchange-Energy Approximation with Correct Asymptotic Behavior. *Physical Review A* **1988**, *38*, 3098-3100.
107. Langreth, D. C.; Mehl, M. J. Beyond the Local-Density Approximation in Calculations of Ground-State Electronic Properties. *Physical Review B* **1983**, *28*, 1809-1834.
108. Ghosh, S. K.; Parr, R. G. Phase-Space Approach to the Exchange-Energy Functional of Density-Functional Theory. *Physical Review A* **1986**, *34*, 785-791.
109. Becke, A. D.; Roussel, M. R. Exchange Holes in Inhomogeneous Systems: A Coordinate-Space Model. *Physical Review A* **1989**, *39*, 3761-3767.
110. Tao, J.; Perdew, J. P.; Staroverov, V. N.; Scuseria, G. E. Climbing the Density Functional Ladder: Nonempirical Meta--Generalized Gradient Approximation Designed for Molecules and Solids. *Phys. Rev. Lett.* **2003**, *91*, 146401.
111. Perdew, J. P.; Ernzerhof, M.; Burke, K. Rationale for Mixing Exact Exchange with Density Functional Approximations. *The Journal of Chemical Physics* **1996**, *105*, 9982-9985.

112. Kim, K.; Jordan, K. D. Comparison of Density Functional and Mp2 Calculations on the Water Monomer and Dimer. *J. Phys. Chem.* **1994**, *98*, 10089-10094.
113. Becke, A. D. Density-Functional Thermochemistry. Iii. The Role of Exact Exchange. *The Journal of Chemical Physics* **1993**, *98*, 5648-5652.
114. Becke, A. D. A New Mixing of Hartree–Fock and Local Density-Functional Theories. *The Journal of Chemical Physics* **1993**, *98*, 1372-1377.
115. Stephens, P. J.; Devlin, F. J.; Chabalowski, C. F.; Frisch, M. J. Ab Initio Calculation of Vibrational Absorption and Circular Dichroism Spectra Using Density Functional Force Fields. *J. Phys. Chem.* **1994**, *98*, 11623-11627.
116. Lee, C.; Yang, W.; Parr, R. G. Development of the Colle-Salvetti Correlation-Energy Formula into a Functional of the Electron Density. *Physical Review B* **1988**, *37*, 785-789.
117. Vosko, S. H.; Wilk, L.; Nusair, M. Accurate Spin-Dependent Electron Liquid Correlation Energies for Local Spin Density Calculations: A Critical Analysis. *Canadian Journal of Physics* **1980**, *58*, 1200-1211.
118. C., B. E. A.; W., G. J. An Assessment of Pure, Hybrid, Meta, and Hybrid-Meta Gga Density Functional Theory Methods for Open-Shell Systems: The Case of the Nonheme Iron Enzyme 8r–Lox. *Journal of Computational Chemistry* **2013**, *34*, 141-148.
119. Zhao, Y.; Truhlar, D. G. The M06 Suite of Density Functionals for Main Group Thermochemistry, Thermochemical Kinetics, Noncovalent Interactions, Excited States, and Transition Elements: Two New Functionals and Systematic Testing of Four M06-Class Functionals and 12 Other Functionals. *Theoretical Chemistry Accounts* **2008**, *120*, 215-241.
120. Zhao, Y.; Truhlar, D. G. Density Functional for Spectroscopy: No Long-Range Self-Interaction Error, Good Performance for Rydberg and Charge-Transfer States, and Better Performance on Average Than B3lyp for Ground States. *The Journal of Physical Chemistry A* **2006**, *110*, 13126-13130.
121. Mulliken, R. S. Electronic Population Analysis on Lcao–Mo Molecular Wave Functions. I. *The Journal of Chemical Physics* **1955**, *23*, 1833-1840.
122. Csizmadia, I. G. *Theory and Practice of Mo Calculations on Organic Molecules*, 1 ed.; Elsevier Scientific Pub. Co.: Amsterdam, 1976.
123. Chipot, C.; Maigret, B.; Rivail, J. L.; Scheraga, H. A. Modeling Amino Acid Side Chains. 1. Determination of Net Atomic Charges from Ab Initio Self-Consistent-Field Molecular Electrostatic Properties. *J. Phys. Chem.* **1992**, *96*, 10276-10284.
124. Chirlian, L. E.; Francl, M. M. Atomic Charges Derived from Electrostatic Potentials: A Detailed Study. *Journal of Computational Chemistry* **1987**, *8*, 894-905.
125. Chandra, S. U.; Kollman, P. A. An Approach to Computing Electrostatic Charges for Molecules. *Journal of Computational Chemistry* **1984**, *5*, 129-145.
126. Besler, B. H.; Merz, K. M.; Kollman, P. A. Atomic Charges Derived from Semiempirical Methods. *Journal of Computational Chemistry* **1990**, *11*, 431-439.
127. Breneman, C. M.; Wiberg, K. B. Determining Atom-Centered Monopoles from Molecular Electrostatic Potentials. The Need for High Sampling Density in Formamide Conformational Analysis. *Journal of Computational Chemistry* **1990**, *11*, 361-373.
128. Bader, R. F. W. A Quantum Theory of Molecular Structure and Its Applications. *Chemical Reviews* **1991**, *91*, 893-928.
129. Bader, R. F. W. *Atoms in Molecule:S: A Quantum Theory*, 1 ed.; Oxford University Press: Oxford, 1994.

130. Tang, W.; Sanville, E.; Henkelman, G. A Grid-Based Bader Analysis Algorithm without Lattice Bias. *Journal of Physics: Condensed Matter* **2009**, *21*, 084204.
131. Sanville, E.; Kenny, S. D.; Smith, R.; Henkelman, G. Improved Grid-Based Algorithm for Bader Charge Allocation. *Journal of Computational Chemistry* **2007**, *28*, 899-908.
132. Henkelman, G.; Arnaldsson, A.; Jónsson, H. A Fast and Robust Algorithm for Bader Decomposition of Charge Density. *Computational Materials Science* **2006**, *36*, 354-360.
133. Leach, A. R. *Molecular Modelling: Principles and Applications*, 2 ed.; Prentice Hall: Upper Saddle River, 2001.
134. Alder, B. J.; Wainwright, T. E. Studies in Molecular Dynamics. I. General Method. *The Journal of Chemical Physics* **1959**, *31*, 459-466.
135. Rahman, A. Correlations in the Motion of Atoms in Liquid Argon. *Physical Review* **1964**, *136*, A405-A411.
136. Shin, S. A New Method of Drawing the Potential Energy Surface. *Bulletin of the Chemical Society of Japan* **1955**, *28*, 450-453.
137. Albaugh, A., et al. Advanced Potential Energy Surfaces for Molecular Simulation. *The Journal of Physical Chemistry B* **2016**, *120*, 9811-9832.
138. Nutt, D. R.; Karplus, M.; Meuwly, M. Potential Energy Surface and Molecular Dynamics of Mbno: Existence of an Unsuspected Feon Minimum. *The Journal of Physical Chemistry B* **2005**, *109*, 21118-21125.
139. Injan, N.; Megyes, T.; Radnai, T.; Bako, I.; Balint, S.; Limtrakul, J.; Spangberg, D.; Probst, M. Potential Energy Surface and Molecular Dynamics Simulation of Gold(I) in Liquid Nitromethane. *Journal of Molecular Liquids* **2009**, *147*, 64-70.
140. Bussai, C.; Hannongbua, S.; Fritzsche, S.; Haberlandt, R. Ab Initio Potential Energy Surface and Molecular Dynamics Simulations for the Determination of the Diffusion Coefficient of Water in Silicalite-1. *Chemical Physics Letters* **2002**, *354*, 310-315.
141. Ermoshin, V. A.; Engel, V. Construction of a Potential Energy Surface for Molecular Dynamics Studies of Methane Adsorbed in Zeolites. *The Journal of Physical Chemistry A* **1999**, *103*, 5116-5122.
142. Morse, P. M. Diatomic Molecules According to the Wave Mechanics. Ii. Vibrational Levels. *Physical Review* **1929**, *34*, 57-64.
143. Girifalco, L. A.; Weizer, V. G. Application of the Morse Potential Function to Cubic Metals. *Physical Review* **1959**, *114*, 687-690.
144. Shore, B. W. Comparison of Matrix Methods Applied to the Radial Schrödinger Eigenvalue Equation: The Morse Potential. *The Journal of Chemical Physics* **1973**, *59*, 6450-6463.
145. Rappe, A. K.; Goddard, W. A. Charge Equilibration for Molecular-Dynamics Simulations. *J. Phys. Chem.* **1991**, *95*, 3358-3363.
146. Gasteiger, J.; Marsili, M. A New Model for Calculating Atomic Charges in Molecules. *Tetrahedron Letters* **1978**, *19*, 3181-3184.
147. Gasteiger, J.; Marsili, M. Iterative Partial Equalization of Orbital Electronegativity—a Rapid Access to Atomic Charges. *Tetrahedron* **1980**, *36*, 3219-3228.
148. Buckingham, R. A. The Classical Equation of State of Gaseous Helium, Neon and Argon. *Proceedings of the Royal Society of London. Series A. Mathematical and Physical Sciences* **1938**, *168*, 264-283.
149. Lennard-Jones, J. E. On the Determination of Molecular Fields. —Ii. From the Equation of State of a Gas. *Proceedings of the Royal Society of London. Series A* **1924**, *106*, 463-477.

150. Atkinson, K. E. *An Introduction to Numerical Analysis*, 2 ed.; John WIley & Sons: New York, 1989.
151. Bonnans, J. F.; Gilbert, J. C.; Lemaréchal, C.; Sagastizábal, C. A. *Numerical Optimization: Theoretical and Practical Aspects*, 2 ed.; Springer-Verlag: Berlin, 2006.
152. Ortega, J. M.; Rheinboldt, W. C. *Iterative Solution of Nonlinear Equations in Several Variables*, 1 ed.; Society for Industrial and Applied Mathematics: Philadelphia, 2000.
153. Lewars, E. G. The Concept of the Potential Energy Surface. In *Computational Chemistry: Introduction to the Theory and Applications of Molecular and Quantum Mechanics*, Springer Netherlands: Dordrecht, 2011; pp 9-43.
154. Verlet, L. Computer "Experiments" on Classical Fluids. I. Thermodynamical Properties of Lennard-Jones Molecules. *Physical Review* **1967**, *159*, 98-103.
155. Swope, W. C.; Andersen, H. C.; Berens, P. H.; Wilson, K. R. A Computer Simulation Method for the Calculation of Equilibrium Constants for the Formation of Physical Clusters of Molecules: Application to Small Water Clusters. *The Journal of Chemical Physics* **1982**, *76*, 637-649.
156. Eric, B.; Krzysztof, K.; Benedict, L.; D., S. R. Algorithms for Constrained Molecular Dynamics. *Journal of Computational Chemistry* **1995**, *16*, 1192-1209.
157. Beeman, D. Some Multistep Methods for Use in Molecular Dynamics Calculations. *Journal of Computational Physics* **1976**, *20*, 130-139.
158. Berendsen, H. J. C.; Postma, J. P. M.; Gunsteren, W. F. v.; DiNola, A.; Haak, J. R. Molecular Dynamics with Coupling to an External Bath. *The Journal of Chemical Physics* **1984**, *81*, 3684-3690.
159. Morishita, T. Fluctuation Formulas in Molecular-Dynamics Simulations with the Weak Coupling Heat Bath. *The Journal of Chemical Physics* **2000**, *113*, 2976-2982.
160. Lin, Y.; Pan, D.; Li, J.; Zhang, L.; Shao, X. Application of Berendsen Barostat in Dissipative Particle Dynamics for Nonequilibrium Dynamic Simulation. *The Journal of Chemical Physics* **2017**, *146*, 124108.
161. Andersen, H. C. Molecular Dynamics Simulations at Constant Pressure and/or Temperature. *The Journal of Chemical Physics* **1980**, *72*, 2384-2393.
162. Tanaka, H.; Nakanishi, K.; Watanabe, N. Constant Temperature Molecular Dynamics Calculation on Lennard-Jones Fluid and Its Application to Watera). *The Journal of Chemical Physics* **1983**, *78*, 2626-2634.
163. Hünenberger, P. H. Thermostat Algorithms for Molecular Dynamics Simulations. In *Advanced Computer Simulation: Approaches for Soft Matter Sciences I*, Dr. Holm, C.; Prof. Dr. Kremer, K., Eds. Springer Berlin Heidelberg: Berlin, Heidelberg, 2005; pp 105-149.
164. Braga, C.; Travis, K. P. A Configurational Temperature Nosé-Hoover Thermostat. *The Journal of Chemical Physics* **2005**, *123*, 134101.
165. Patra, P. K.; Bhattacharya, B. A Deterministic Thermostat for Controlling Temperature Using All Degrees of Freedom. *The Journal of Chemical Physics* **2014**, *140*, 064106.
166. Hoogerbrugge, P. J.; Koelman, J. M. V. A. Simulating Microscopic Hydrodynamic Phenomena with Dissipative Particle Dynamics. *EPL (Europhysics Letters)* **1992**, *19*, 155.
167. Koelman, J. M. V. A.; Hoogerbrugge, P. J. Dynamic Simulations of Hard-Sphere Suspensions under Steady Shear. *EPL (Europhysics Letters)* **1993**, *21*, 363.
168. Español, P.; Warren, P. Statistical Mechanics of Dissipative Particle Dynamics. *EPL (Europhysics Letters)* **1995**, *30*, 191.

169. Groot, R. D.; Warren, P. B. Dissipative Particle Dynamics: Bridging the Gap between Atomistic and Mesoscopic Simulation. *The Journal of Chemical Physics* **1997**, *107*, 4423-4435.
170. Fokker, A. D. Die Mittlere Energie Rotierender Elektrischer Dipole Im Strahlungsfeld. *Annalen der Physik* **1914**, *348*, 810-820.
171. Planck, M. Über Einen {S}Atz Der Statistischen {D}Ynamik Und Seine {E}Rweiterung in Der {Q}Uantentheorie. *Sitzungsber. Preuss. Akad. Wiss.* **1917**, *24*, 324-341.
172. Kolmogorov, A. Über Die Analytischen Methoden in Der Wahrscheinlichkeitsrechnung. *Mathematische Annalen* **1931**, *104*, 415-458.
173. Chun, B. J.; Fisher, C. C.; Jang, S. S. Dissipative Particle Dynamics Simulation Study of Poly(2-Oxazoline)-Based Multicompartment Micelle Nanoreactor. *Phys. Chem. Chem. Phys.* **2016**, *18*, 6284-6290.
174. Chongli, Z.; Dahuan, L. Understanding Multicompartment Micelles Using Dissipative Particle Dynamics Simulation. *Macromolecular Theory and Simulations* **2007**, *16*, 141-157.
175. Jun, X.; Chongli, Z. Dissipative Particle Dynamics Study of the Formation of Multicompartment Micelles from Abc Star Triblock Copolymers in Water. *Macromolecular Rapid Communications* **2006**, *27*, 1110-1114.
176. Zhao, Y.; Liu, Y.-T.; Lu, Z.-Y.; Sun, C.-C. Effect of Molecular Architecture on the Morphology Diversity of the Multicompartment Micelles: A Dissipative Particle Dynamics Simulation Study. *Polymer* **2008**, *49*, 4899-4909.
177. Ramezani, M.; Shamsara, J. Application of Dpd in the Design of Polymeric Nano-Micelles as Drug Carriers. *Journal of Molecular Graphics and Modelling* **2016**, *66*, 1-8.
178. Lee, M.-T.; Vishnyakov, A.; Neimark, A. V. Calculations of Critical Micelle Concentration by Dissipative Particle Dynamics Simulations: The Role of Chain Rigidity. *The Journal of Physical Chemistry B* **2013**, *117*, 10304-10310.
179. Li, Y.; Zhang, H.; Bao, M.; Chen, Q. Aggregation Behavior of Surfactants with Different Molecular Structures in Aqueous Solution: Dpd Simulation Study. *Journal of Dispersion Science and Technology* **2012**, *33*, 1437-1443.
180. Cheng, F.; Guan, X.; Cao, H.; Su, T.; Cao, J.; Chen, Y.; Cai, M.; He, B.; Gu, Z.; Luo, X. Characteristic of Core Materials in Polymeric Micelles Effect on Their Micellar Properties Studied by Experimental and Dpd Simulation Methods. *International Journal of Pharmaceutics* **2015**, *492*, 152-160.
181. Al-Saigh, Z. Y.; Munk, P. Study of Polymer-Polymer Interaction Coefficients in Polymer Blends Using Inverse Gas Chromatography. *Macromolecules* **1984**, *17*, 803-809.
182. Panayiotou, C. Polymer-Polymer Miscibility and Partial Solvation Parameters. *Polymer* **2013**, *54*, 1621-1638.
183. DiPaola-Baranyi, G.; Guillet, J. E. Estimation of Polymer Solubility Parameters by Gas Chromatography. *Macromolecules* **1978**, *11*, 228–235.
184. Chiu, M. H.; Prenner, E. J. Differential Scanning Calorimetry: An Invaluable Tool for a Detailed Thermodynamic Characterization of Macromolecules and Their Interactions. *J. Pharm. Bioallied Sci.* **2011**, *3*, 39-59.
185. Knopp, M. M.; Olesen, N. E.; Holm, P.; Langguth, P.; Holm, R.; Rades, T. Influence of Polymer Molecular Weight on Drug–Polymer Solubility: A Comparison between Experimentally Determined Solubility in Pvp and Prediction Derived from Solubility in Monomer. *J. Pharm. Sci.* **2015**, *104*, 2905-2912.

186. Silva, M. E. S. R.; Mano, V.; Pacheco, R. R. J.; Freitas, R. F. S. Miscibility Behavior of Polyacrylamides Poly(Ethylene Glycol) Blends: Flory Huggins Interaction Parameter Determined by Thermal Analysis. *J. Mod. Phys.* **2013**, *4*, 45-51.
187. Yang, H.; Ricci, S.; Collins, M. Study of Interaction Parameters of Phase-Separated Polymer Blends by Differential Scanning Calorimetry. *Macromolecules* **1991**, *24*, 5218-5220.
188. Bates, F. S.; Wignall, G. D. Isotope-Induced Quantum-Phase Transitions in the Liquid-State. *Phys. Rev. Lett.* **1986**, *57*, 1429-1432.
189. Ito, H.; Russell, T. P.; Wignall, G. D. Interactions in Mixtures of Poly(Ethylene Oxide) and Poly(Methyl Methacrylate). *Macromolecules* **1987**, *20*, 2213-2220.
190. Russell, T. P. Changes in Polystyrene and Poly(Methyl Methacrylate) Interactions with Isotopic-Substitution. *Macromolecules* **1993**, *26*, 5819-5819.
191. Yurekli, K.; Krishnamoorti, R. Thermodynamic Interactions in Blends of Poly(4-Tert-Butyl Styrene) and Polyisoprene by Small-Angle Neutron Scattering. *J. Polym. Sci. Part B: Polym. Phys.* **2004**, *42*, 3204–3217.
192. Eitouni, H. B.; Balsara, N. P. Thermodynamics of Polymer Blends. In *Physical Properties of Polymers Handbook*, Springer: New York, 2007.
193. Burkert, U.; Allinger, N. L. *Molecular Mechanics*; American Chemical Society: Washington, DC, 1982.
194. Bochevarov, A. D.; Harder, E.; Hughes, T. F.; Greenwood, J. R.; Braden, D. A.; Philipp, D. M.; Rinaldo, D.; Halls, M. D.; Zhang, J.; Friesner, R. A. Jaguar: A High-Performance Quantum Chemistry Software Program with Strengths in Life and Materials Sciences. *Int. J. Quantum Chem.* **2013**, *113*, 2110-2142.
195. Gohy, J.-F.; Ott, C.; Hoeppener, S.; Schubert, U. S. Multicompartment Micelles from a Metallo-Supramolecular Tetrablock Quatercopolymer. *Chemical Communications* **2009**, 6038-6040.
196. Mayo, S. L.; Olafson, B. D.; Goddard, W. A. Dreiding - a Generic Force-Field for Molecular Simulations. *J. Phys. Chem.* **1990**, *94*, 8897-8909.
197. Brunello, G. F.; Lee, S. G.; Jang, S. S.; Qi, Y. A Molecular Dynamics Simulation Study of Hydrated Sulfonated Poly(Ether Ether Ketone) for Application to Polymer Electrolyte Membrane Fuel Cells: Effect of Water Content. *Journal of Renewable and Sustainable Energy* **2009**, *1*.
198. Lee, S. G.; Jang, S. S.; Kim, J.; Kim, G. Distribution and Diffusion of Water in Epoxy Molding Compound: Molecular Dynamics Simulation Approach *IEEE Transactions on Advanced Packaging* **2010**, *33*, 333-339.
199. Brunello, G. F.; Mateker, W. R.; Lee, S. G.; Choi, J. I.; Jang, S. S. Effect of Temperature on Structure and Water Transport of Hydrated Sulfonated Poly(Ether Ether Ketone): A Molecular Dynamics Simulation Approach. *Journal of Renewable and Sustainable Energy* **2011**, *3*.
200. Lee, S. G.; Choi, J. I.; Koh, W.; Jang, S. S.; Kim, J.; Kim, G. Effect of Temperature on Water Molecules in Model Epoxy Molding Compound: Molecular Dynamics Simulation Approach. *IEEE Transactions on Components, Packaging and Manufacturing Technology* **2011**, *1*, 1533.
201. Lee, S. G.; Koh, W.; Brunello, G. F.; Choi, J. I.; Bucknall, D. G.; Jang, S. S. Effect of Monomeric Sequence on Transport Properties of D-Glucose and Ascorbic Acid in Poly(Vp-Co-Hema) Hydrogels with Various Water Contents: Molecular Dynamics Simulation Approach. *Theoretical Chemistry Accounts* **2012**, *131*, 1206.

202. Lee, S. G.; Pascal, T. A.; Koh, W.; Brunello, G. F.; Goddard, W. A.; Jang, S. S. Deswelling Mechanisms of Surface-Grafted Poly(Nipaam) Brush: Molecular Dynamics Simulation Approach. *J. Phys. Chem. C* **2012**, *116*, 15974–15985.
203. Ahmadi, A.; Freire, J. J. Prediction of Polymer Mixture Compatibility by Monte Carlo Simulation of Intermolecular Binary Interactions. *Polymer* **2009**, *50*, 3871–3876.
204. Pajula, K.; Taskinen, M.; Lehto, V.-P.; Ketolainen, J.; Korhonen, O. Predicting the Formation and Stability of Amorphous Small Molecule Binary Mixtures from Computationally Determined Flory−Huggins Interaction Parameter and Phase Diagram. *Mol. Pharmaceutics* **2010**, *7*, 795-804.
205. Rezaei, H.; Amjad-Iranagh, S.; Modarress, H. Self-Accumulation of Uncharged Polyaromatic Surfactants at Crude Oil–Water Interface: A Mesoscopic Dpd Study. *Energy & Fuels* **2016**, *30*, 6626–6639.
206. Connolly, M. L. Analytical Molecular Surface Calculation. *Journal of Applied Crystallography* **1983**, *16*, 548-558.
207. Connolly, M. L. The Molecular Surface Package. *Journal of Molecular Graphics* **1993**, *11*, 139-141.
208. Richmond, T. J. Solvent Accessible Surface Area and Excluded Volume in Proteins: Analytical Equations for Overlapping Spheres and Implications for the Hydrophobic Effect. *Journal of Molecular Biology* **1984**, *178*, 63-89.
209. Connolly, M. L. Computation of Molecular Volume. *J. Am. Chem. Soc.* **1985**, *107*, 1118-1124.
210. Connolly, M. L. Molecular Interstitial Skeleton. *Computers & Chemistry* **1991**, *15*, 37-45.
211. L., C. M. Shape Distributions of Protein Topography. *Biopolymers* **1992**, *32*, 1215-1236.
212. Akkermans, R. L. C.; Spenley, N. A.; Robertson, S. H. Monte Carlo Methods in Materials Studio. *Molecular Simulation* **2013**, *39*, 1153-1164.
213. Chremos, A.; Nikoubashman, A.; Panagiotopoulos, A. Z. Flory-Huggins Parameter X, from Binary Mixtures of Lennard-Jones Particles to Block Copolymer Melts. *The Journal of Chemical Physics* **2014**, *140*.
214. Levitt, M.; Lifson, S. Refinement of Protein Conformations Using a Macromolecular Energy Minimization Procedure. *Journal of Molecular Biology* **1969**, *46*, 269-279.
215. Brooks, B. R.; Bruccoleri, R. E.; Olafson, B. D.; States, D. J.; Swaminathan, S.; Karplus, M. Charmm: A Program for Macromolecular Energy, Minimization, and Dynamics Calculations. *Journal of Computational Chemistry* **1983**, *4*, 187-217.
216. Broyden, C. G. The Convergence of a Class of Double-Rank Minimization Algorithms 1. General Considerations. *IMA Journal of Applied Mathematics* **1970**, *6*, 76-90.
217. Fletcher, R. A New Approach to Variable Metric Algorithms. *The Computer Journal* **1970**, *13*, 317-322.
218. Goldfarb, D. A Family of Variable-Metric Methods Derived by Variational Means. *Mathematics of Computation* **1970**, *24*, 23-26.
219. Shanno, D. F. Conditioning of Quasi-Newton Methods for Function Minimization. *Mathematics of Computation* **1970**, *24*, 647-656.
220. Gröschel, A. H.; Schacher, F. H.; Schmalz, H.; Borisov, O. V.; Zhulina, E. B.; Walther, A.; Müller, A. H. E. Precise Hierarchical Self-Assembly of Multicompartment Micelles. *Nature Communications* **2012**, *3*.
221. Wang, L.; Lin, J. Discovering Multicore Micelles: Insights into the Self-Assembly of Linear Abc Terpolymers in Midblock-Selective Solvents. *Soft Matter* **2011**, *7*, 3383-3391.

222. Procházka, K.; Martin, T. J.; Webber, S. E.; Munk, P. Onion-Type Micelles in Aqueous Media. *Macromolecules* **1996**, *29*, 6526-6530.
223. Talingting, M. R.; Munk, P.; Webber, S. E.; Tuzar, Z. Onion-Type Micelles from Polystyrene-Block-Poly(2-Vinylpyridine) and Poly(2-Vinylpyridine)-Block-Poly(Ethylene Oxide). *Macromolecules* **1999**, *32*, 1593-1601.
224. Pleštil, J.; Kříž, J.; Tuzar, Z.; Procházka, K.; Melnichenko, Y. B.; Wignall, G. D.; Talingting, M. R.; Munk, P.; Webber, S. E. Small-Angle Neutron Scattering Study of Onion-Type Micelles. *Macromolecular Chemistry and Physics* **2001**, *202*, 553-563.
225. Read, E. S.; Armes, S. P. Recent Advances in Shell Cross-Linked Micelles. *Chemical Communications* **2007**, 3021-3035.
226. Synatschke, C. V., et al. Multicompartment Micelles with Adjustable Poly(Ethylene Glycol) Shell for Efficient in Vivo Photodynamic Therapy. *ACS Nano* **2014**, *8*, 1161-1172.
227. Wang, X.; Gao, J.; Wang, Z.; Xu, J.; Li, C.; Sun, S.; Hu, S. Dissipative Particle Dynamics Simulation on the Self-Assembly and Disassembly of Ph-Sensitive Polymeric Micelle with Coating Repair Agent. *Chemical Physics Letters* **2017**, *685*, 328-337.
228. Zhong, C.; Liu, D. Understanding Multicompartment Micelles Using Dissipative Particle Dynamics Simulation. *Macromolecular Theory and Simulations* **2007**, *16*, 141-157.
229. Xia, J.; Zhong, C. Dissipative Particle Dynamics Study of the Formation of Multicompartment Micelles from Abc Star Triblock Copolymers in Water. *Macromolecular Rapid Communications* **2006**, *27*, 1110-1114.
230. Hoogenboom, R.; Wiesbrock, F.; Leenen, M. A. M.; Thijs, H. M. L.; Huang, H.; Fustin, C.-A.; Guillet, P.; Gohy, J.-F.; Schubert, U. S. Synthesis and Aqueous Micellization of Amphiphilic Tetrablock Ter- and Quarterpoly(2-Oxazoline)S. *Macromolecules* **2007**, *40*, 2837-2843.
231. Fustin, C.-A.; Thijs-Lambermont, H. M. L.; Hoeppener, S.; Hoogenboom, R.; Schubert, U. S.; Gohy, J.-F. Multiple Micellar Morphologies from Tri- and Tetrablock Copoly(2-Oxazoline)S in Binary Water–Ethanol Mixtures. *Journal of Polymer Science Part A: Polymer Chemistry* **2010**, *48*, 3095-3102.
232. Li, Z.; Liu, G. Water-Dispersible Tetrablock Copolymer Synthesis, Aggregation, Nanotube Preparation, and Impregnation. *Langmuir* **2003**, *19*, 10480-10486.
233. Puig-Rigall, J.; Obregon-Gomez, I.; Monreal-Pérez, P.; Radulescu, A.; Blanco-Prieto, M. J.; Dreiss, C. A.; González-Gaitano, G. Phase Behaviour, Micellar Structure and Linear Rheology of Tetrablock Copolymer Tetronic 908. *Journal of Colloid and Interface Science* **2018**, *524*, 42-51.
234. Kostarelos, K.; Miller, A. D. Synthetic, Self-Assembly Abcd Nanoparticles; a Structural Paradigm for Viable Synthetic Non-Viral Vectors. *Chemical Society Reviews* **2005**, *34*, 970-994.